

**ASSESSING THE DETERMINANTS THAT PARSE THE LYASE AND MUTASE
ACTIVITIES OF A PLANT AMINOMUTASE, AND DEVELOPING A
REGIOSELECTIVE COUPLING REACTION FOR A TRIALKYL PYRAZINE.**

By

Gayanthi Kumari Attanayake

A DISSERTATION

**Submitted to
Michigan State University
in partial fulfillment of the requirements
for the degree of**

Chemistry – Doctor of Philosophy

2021

ABSTRACT

ASSESSING THE DETERMINANTS THAT PARSE THE LYASE AND MUTASE ACTIVITIES OF A PLANT AMINOMUTASE, AND DEVELOPING A REGIOSELECTIVE COUPLING REACTION FOR A TRIALKYL PYRAZINE.

By

Gayanthi Kumari Attanayake

This dissertation is mainly contributed with two main projects. The first project is based on aminomutase enzyme. Recent discovery of MIO-dependent aminomutases on the biosynthetic pathways of biologically active, medicinal compounds in plants and microorganisms raises interest in further understanding how they catalyze β -amino acid building blocks. A tyrosine aminomutase isolated from Japanese rice, *Oryza sativa* (*OsTAM*), converts α -tyrosine to β -tyrosine (75%) and makes an acrylate, *p*-coumarate (25%), as a by-product. *OsTAM* is the first TAM to have slight phenylalanine aminomutase (PAM) activity (3%). This may not be surprising since the active sites of *OsTAM* and *TcPAM* from *Taxus* plants differ by only two residues (Y125 and N446 of *OsTAM* compared to C107 and K427 of *TcPAM*, respectively) positioned similarly near the aryl ring of their substrates. We anticipated by changing key active site residues of *OsTAM* to nonpolar side chains found in *TcPAM* would improve the binding of substituted phenylalanine substrates. Another feature of MIO-aminomutases, highlighted in a previous study,¹ is a hinge-gate inner loop that opens and closes the entry to the active site. We changed hydrophilic for more hydrophobic residues within the *OsTAM* loop like in *TcPAM* to make it function as a more efficient PAM and expected the mutants to produce a greater proportion of the β -amino acid over acrylate compared to that made by wild-type *OsTAM*. Our data suggested that a combination of active site mutants and loop mutants generally increased the turnover of *OsTAM* for *para*-substituted substrates over the other *meta*- and *ortho*- regioisomers

to their corresponding cinnamates, and not to the β -amino acids, as the major products. These findings suggest that while active site residues may be involved primarily in creating broad substrate selectivity, their role along with that of the inner loop to parse the reaction toward β -amino acids remains elusive.

The second project mainly focused on regioselective synthesis of ethyl dimethyl pyrazine. Alkylpyrazines are important heterocyclic compounds used as flavorants in the food and beverage industries. This study developed a regioselective synthesis of 2-ethyl-3,5-dimethylpyrazine (235-EDMP) over its 3-ethyl-2,5-dimethyl isomer (325-EDMP). Our first attempts explored how steric direct the coupling orientations between diamines to diketones to access 235-EDMP. Also, various physical parameters of the reaction conditions were changed, such as reduced temperature, the order-of-addition of reactants, and supplementation with chiral zeolites (Montmorillonite phyllosilicates) to template the orientation of the coupling partners to direct the regiochemistry of the reaction. Each reaction trial resulted in 50:50 mixtures of the ethyl dimethylpyrazine regioisomers. An alternative approach was explored to direct the regioselectivity of the reactions; acyloins (α -hydroxy ketone) replaced the diketone as the electrophilic coupling reactant used in the previous trial experiments. The hydroxy ketone reactants were made biocatalytically with pyruvate decarboxylase (E.C. 4.1.1.1). The coupling reaction between 2-hydroxypentan-3-one and propane-1,2-diamine resulted in the desired 235-EDMP at >70% (~77 mg total) relative to 30% 325-EDMP in the product mixture. The 3-hydroxypentan-2-one acyloin congener bio catalyzed and reacted with propane-1,2-diamine as proof of principle to make 325-EDMP (~60% relative abundance, ~57 mg) over the 235-EDMP. These results hinted toward a mechanism directed by the hydroxy ketone electrophilicity and the sterics at each nucleophilic center of the diamine.

ACKNOWLEDGMENTS

I would like to extend my deepest gratitude to my research advisor, Prof. Kevin Walker for his encouragement and spontaneous willingness to answer my numerous questions and helping me to develop my carrier. Prof. Walker's encouragement and motivation always helped me to build up my personal attitude as an independent researcher. I realize that it would not be possible to accomplish this thesis and my publications without the efforts of my research advisor.

I am similarly thankful to the members of the graduate advisory committee: Prof. James. Geiger, Prof. Xuefei Huang and Prof. A. Dan Jones for their continuous involvement in the project. I appreciate their invaluable support during my dissertation time. Furthermore, I would like to extend my sincere appreciation to our collaborator Dr. Guohong Mao in Conagen, LLC for his guidance and funding for this project

Mass Spectrometry and Metabolomics Core of MSU had provided me knowledge of analytical techniques during my project. I appreciate, Dr. Tony Schillmiller, and Dr. Casey Johnny for all the extensive training and advice during this project. For NMR troubleshooting, Dr. Daniel Holmes at the MTR-NMR Facility helped me to solve all issues.

I would like to thank the Department of Chemistry at Michigan State University for providing me the opportunity to complete my PhD degree thesis work; and, respectfully thank all the faculty members and staff in the Department of Chemistry at MSU. Special thanks go to Prof. Gary Blanchard and Prof. Robert Maleczka (chair) for providing me recommendations for fellowships given from MSU.

Thanks to my group members Dr. Tyler Walter, Dr. Prakash Shee and Aimen Al-Hilfi for their kind cooperation throughout my study at MSU. I am grateful for all the advice and support given me through entire my life in MSU which has helped me to balance my personal life and carrier life as a graduate student.

Special thanks go to my family members for their unconditional help throughout my life. My parents and My Husband have been exceptionally supportive; without their help I would have never made it through graduate school.

TABLE OF CONTENTS

LIST OF TABLES.....	x
LIST OF FIGURES.....	xi
LIST OF SCHEMES.....	xxi
KEY TO ABBREVIATIONS.....	xxii
Chapter 1 . Overview of Aminomutase Enzyme	1
1.1 Applications of Aminomutase Enzymes in Pharmaceutical Industry.....	1
1.2 Aminomutases Classification based on Mechanism.....	2
1.2.1 Adenosylcobalamin (AdoCbl) dependent aminomutase.	2
1.2.2 S-Adenosylmethionine (SAM)-dependent aminomutases.....	3
1.2.3 Methylideneimidazole-5-one-dependent aminomutases.	3
1.3 Subclasses of MIO AMs	5
REFERENCES.	7
Chapter 2 . Tyrosine Aminomutase Derived from <i>Oryza sativa</i>	11
2.1 Introduction.....	11
2.2 Objective.....	11
2.3 Experimental.....	12
2.3.1 Chemicals and Reagents	12
2.3.2 OsTAM Mutations.....	12
2.3.3 Subcloning, Expression, and Purification of Mutant <i>OsTAM</i>	13
2.3.4 Activity of <i>OsTAM</i> Mutants.....	14
2.3.5 Kinetic Parameters of <i>OsTAM</i> Mutants with α -Phenylalanine Analogues.....	15
2.3.6 Homology Modeling of <i>OsTAM</i> and Its Mutant Cognates.....	16
2.4 Results and Discussion	16
2.4.1 Determining Effects of Active Site Mutants on Substrate Selectivity and Activity.	16
2.4.1.1 N446K- <i>OsTAM</i> mutant <i>p</i> -Substituted Substrates.	20
2.4.1.2 <i>meta</i> - and <i>ortho</i> -Substituted Substrates.	21
2.4.1.3 Y125C- <i>OsTAM</i> Mutant. Substituted Substrates.	23
2.4.1.4 Y125C/N446K- <i>OsTAM</i> Mutant.....	24
2.5 Conclusions.....	26
REFERENCES	27
Chapter 3 . Dissecting the Role of the Inner Loop Caping the Active Site	30
3.1 Introduction.....	30
3.2 Experimental.....	31
3.2.1 Chemicals and Reagents	31
3.2.2 Instrumentation	31

3.2.3 <i>Os</i> TAM Mutations	32
3.2.4 Subcloning, Expression, and Purification of Mutant <i>Os</i> TAM.....	33
3.2.5 Activity of <i>Os</i> TAM Mutants.....	34
3.2.6 Kinetic Parameters of <i>Os</i> TAM Mutants with α -Phenylalanine Analogs.....	35
3.3 Results and Discussion	35
3.3.1 Inner Loop Alterations of <i>Os</i> TAM.	35
3.3.2 Mutation of Inner-Loop Residues T95 and T97.	37
3.3.3 Combined Inner-Loop (T95 and T97) and Active Site Mutations.	40
3.3.4 Mutation of <i>Os</i> TAM Variants with H109S Loop Residue Exchange.	42
3.3.5 Mutation of <i>Os</i> TAM Variants with H109S/F115L Loop Residue Exchanges.	44
3.3.6 Other Mutants Containing the F115L Mutation.	47
3.3.7 Multiple Mutations to "Evolve" the <i>Os</i> TAM Loop to that of <i>Tc</i> PAM.	48
3.4 Conclusions.....	49
APPENDIX.....	50
REFERENCES	85

Chapter 4 . Developing a Coupling Reaction Toward Regioselectively Enriched Ethyl Dimethyl Pyrazine Isomers via Semibiocatalysis	87
4.1 Introduction.....	87
4.1.1 Pyrazines in Food Chemistry	87
4.1.2 Developed Synthetic Routes for Alk Pyrazines.....	88
4.2 Experimental	92
4.2.1 Chemicals, Reagents, and Instrumental Analysis.....	92
4.2.2 Instrumentations.....	93
4.2.3 Synthetic approach to produce 2-ethyl-3,5-dimethylpyrazine through diketone and diamine coupling.....	94
4.2.4 Assessing conditions for the diketone and diamine coupling reaction to increase the regioselectivity.	94
4.2.5 Synthesis of hydroxypentanones 17 and 18.....	95
4.2.6 Synthesis of EDMP isomers.	96
4.2.7 HPLC separation to isolate 235-EDMP from a commercially available EDMP mixture	97
4.3 Results and Discussion	97
4.3.1 Separation of the EDMP Isomers.	97
4.3.2 Regioselective Assembly of EDMP Isomer.	100
4.3.2.1 Synthetic Assembly of 235 EDMP.....	100
4.3.3 Semibiocatalytic Assembly of Isomerically Enriched EDMP Isomers.	102
4.3.3.1 Biocatalysis of Alkyl Acyloins.	102
4.3.4 Assembly of Isomerically Enriched 235-EDMP.	109
4.3.5 Assembly of Isomerically Enriched 325-EDMP.	109
4.3.6 Putative side-products in EDMP Preparations.....	111
4.4 Conclusion	114
APPENDIX.....	116
REFERENCES	133

LIST OF TABLES

Table 2.1. Kinetic Parameters of <i>OsTAM</i> Wild-type and Mutant Enzymes for α -Phenylalanine and Its Analogs.	23
Table S1. Primers ^a Used to Make <i>ostam</i> cDNA Mutants.....	52
Table S2. Primers Used to Make <i>OsTAM</i> Loop Mutations Analogous to Loop of <i>TcPAM</i>	52
Table S3. Plasmids Containing <i>ostam</i> cDNA Mutants.....	53
Table S4. Space Filling Arrangement of <i>para</i> -CH ₃ , -OCH ₃ , and -NO ₂ Substituted Substrates with Different <i>OsTAM</i> Active Site Mutants ^a	54
Table S5. Space Filling Arrangement of <i>para</i> -F, -Cl, and -Br Substituted and α -Phenylalanine with Different <i>OsTAM</i> Active Site Mutants. ^a	55
Table S6. Kinetic Parameters of <i>OsTAM</i> T95A/T97I-Mutants for α -Phenylalanine and Its Analogs.	56
Table 4.1. Estimated Yield of Hydroxyketone (HK) Synthesis.....	107
Table 4.2. Estimated Purity of the Isomerically Enriched EDMPs	111
Table S7. ¹ J _{C,H} (¹³ C- ¹ H HSQC) correlation data for 235-EDMP	118
Table S8. ² J _{C,H} , ³ J _{C,H} (¹³ C- ¹ H HMBC) correlation data for 235-EDMP.....	120
Table S9. ¹ J _{C,H} (¹³ C- ¹ H HSQC) correlations in HSQC of 325-EDMP	122
Table S10. ² J _{C,H} , ³ J _{C,H} (¹³ C- ¹ H HMBC) Coupling Data for 325-EDMP.....	124

LIST OF FIGURES

- Figure 1.1. Natural products containing β -amino acids2
- Figure 1.2. Partial lysine 2,3-aminomutase (LAM) mechanism. Ado-CH₂• is an adenosyl radical. Imine of lysine and pyridoxal (1) proceeding to the β -amino acid precursor radical (4) via the β -amino acid pyridoxal imine radical (2) and the pyridoxal aziridine radical (3).3
- Figure 1.3 Autocatalysis of the 3,5-dihydro-5-methylidene-4H-imidazol-4-one cofactor through cyclization of (A/T/S)-Ser-Gly residues within the active site.4
- Figure 1.4. Mechanism of MIO-dependent aminomutase and ammonia lyase enzymes. Inset 1: Carbanionic transition state intermediate at β -carbon of the substrate. Inset 2: Cationic transition state intermediate at α -carbon of the substrate.5
- Figure 2.1. Comparison of the residues forming the aryl binding pocket for the substrate, catalytic tyrosine, the arginine for carboxylate binding in the active sites and MIO (cyan) of A) *Os*TAM with a cinnamate intermediate (orange) modeled on B) *Tc*PAM (PDB: 3NZ4) and *Pc*PAL (PDB: 1W27) (not shown), and C) *Sg*TAM (PDB: 2RJR). Common residues for all three enzymes were shown in green color.17
- Figure 2.2. *Os*TAM active site mutants A) N446K-*Os*TAM, B) Y125C-*Os*TAM, and C) Y125C/N446K-*Os*TAM modeled on the *Tc*PAM (PDB: 3NZ4) and *Pc*PAL (PDB: 1W27) with cinnamate docked as per PDB: 3NZ4 and PDB: 1W27. Heteroatoms are colored red for oxygen, blue for nitrogen. Numbers are distances in Angstroms. On aryl ring, *o* designates *ortho*-positions, *m* designates *meta*-positions, and *p* designates *para*-position.18
- Figure 2.3. The percent yield of *trans*-cinnamate analogs made biocatalytically from A) N446K-*Os*TAM, B) Y125C-*Os*TAM, C) Y125C/N446K-*Os*TAM active site mutants, and D) wild-type *Os*TAM incubated with *p*-(□), *m*-(▲), and *o*-(○)-substituted α -phenylalanines. The dashed line shows the percent yield of cinnamic acid from phenylalanine, and the solid line shows the percent yield of coumaric acid from tyrosine. Standard error = \pm 5%.19
- Figure 3.1. A) Alignment of inner loop sequences of 1) ammonia lyase *Pc*PAL used to guide mutations in the loop of 2) aminomutase *Tc*PAM to convert its function to that of 3) a *Tc*PAL lyase. B) Alignment of inner loop sequences of 4) *Tc*PAM used to guide mutations in the loop of 5) *Os*TAM to convert its function to that of 6) an aminomutase "*Os*PAM." C) Inner loop structure of *Os*TAM modeled on the *Tc*PAM backbone (PDB: 3NZ4) with the cinnamate intermediate (orange) docked in an orientation based on the cocrystallized cinnamate in the *Tc*PAM structure. Residues in the aryl ring-binding pocket (green), and inner loop region (blue). Heteroatoms are colored red for oxygen, blue for nitrogen.36
- Figure 3.2. The percent yield of *trans*-cinnamate analogs made biocatalytically from A) T95A-*Os*TAM, B) T97I-*Os*TAM, C) T95A/T97I-*Os*TAM, and D) wild-type *Os*TAM incubated with *p*-

(□), *m*-(▲), and *o*-(○)-substituted α -phenylalanines. The dashed line shows the percent yield of cinnamic acid from phenylalanine, and the solid line shows the percent yield of coumaric acid from tyrosine. Standard error = \pm 5%.....38

Figure 3.3. The percent yield of *trans*-cinnamate analogs made biocatalytically from A) Y125C/N446K/T95A-*Os*TAM, B) Y125C/N446K/T97I-*Os*TAM, C) Y125C/N446K/T95A/T97I-*Os*TAM, and D) Y125C/N446K-*Os*TAM (included here from Figure 2.3C for convenience) incubated with *p*-(□), *m*-(▲), and *o*-(○)-substituted α -phenylalanines. The dashed line shows the percent yield of cinnamic acid from phenylalanine, and the solid line shows the percent yield of coumaric acid from tyrosine. Standard error = \pm 5%.....42

Figure 3.4. The percent yield of *trans*-cinnamate analogs made biocatalytically from A) H109S-*Os*TAM, B) N446K/H109S-*Os*TAM, C) T95A/T97I/H109S-*Os*TAM, and D) Y125C/N446K/T95A/T97I/H109S-*Os*TAM incubated with *p*-(□), *m*-(▲), and *o*-(○)-substituted α -phenylalanines. The dashed line shows the percent yield of cinnamic acid from phenylalanine, and the solid line shows the percent yield of coumaric acid from tyrosine. Standard error = \pm 5%.45

Figure 3.5. The percent yield of *trans*-cinnamate analogs for A) F115L-*Os*TAM and B) N446K/F115L-*Os*TAM were incubated with *p*-(□), *m*-(▲), and *o*-(○)-substituted α -phenylalanines. The dashed line shows the percent yield of cinnamic acid from phenylalanine, and the solid line shows the percent yield of coumaric acid from tyrosine. Standard error = \pm 5%.46

Figure 3.6. The percent yield of *trans*-cinnamate analogs for A) M92E/N93D/T95A/T97I-*Os*TAM and B) M92E/N93D/T95A/T97I/G106A /A107C/A108S/H109S-*Os*TAM incubated with *p*-(□), *m*-(▲), and *o*-(○)-substituted α -phenylalanines. The dashed line shows the percent yield of cinnamic acid from phenylalanine, and the solid line shows the percent yield of coumaric acid from tyrosine. Standard error = \pm 5%.....47

Figure S1 SDS-PAGE gel of A) wild-type *Os*TAM after Coomassie blue staining. Purity (55%) estimated by a Kodak Gel Logic 100 Imaging System; *lane* MW: PageRuler® Prestained Ladder, *lane* 1: Enzyme (10 μ L of a ~4.2 mg/mL solution) and of B) N446K-*Os*TAM after Coomassie blue staining. Purity (60%) estimated by a Kodak Gel Logic 100 Imaging System; *lane* MW: PageRuler® Prestained Ladder, *lane* 1: Enzyme (10 μ L of a ~5.6 mg/mL solution). PageRuler® Prestained Ladder: MW (kDa) – 1: 100 kDa, 2: 70 kDa, 3: 55 kDa, 4: 40 kDa, 5: 35 kDa, 6: 25 kDa, and 7: 15 kDa.....56

Figure S2.SDS-PAGE gel of A) Y125C-*Os*TAM after Coomassie blue staining. Purity (55%) estimated by a Kodak Gel Logic 100 Imaging System; *lane* 1: PageRuler® Prestained Ladder (see Figure S1), *lane* MW: Enzyme (5 μ L of a ~3.0 mg/mL solution) and of B) Y125C/N446K-*Os*TAM after Coomassie blue staining. Purity (50%) estimated by a Kodak Gel Logic 100 Imaging System; *lane* MW: PageRuler® Prestained Ladder (see Figure S1), *lane* 1: Enzyme (10 μ L of a ~2.7 mg/mL solution).57

Figure S3. SDS-PAGE gel of A) T95A/T97I-*Os*TAM after Coomassie blue staining. Purity (65%) estimated by a Kodak Gel Logic 100 Imaging System; *lane* MW: PageRuler® Prestained Ladder (see Figure S1), *lane* 1: Enzyme (10 μ L of a ~2.3 mg/mL solution) and of B)

Y125C/N446K/T95A/T97I- <i>Os</i> TAM after Coomassie blue staining. Purity (52%) estimated by a Kodak Gel Logic 100 Imaging System; <i>lane</i> MW: PageRuler © Prestained Ladder (see Figure S1), <i>lane</i> 1: Enzyme (10 μ L of a ~5.4 mg/mL solution).	57
Figure S4. SDS-PAGE gel of A) T95A/T97I/H109S- <i>Os</i> TAM after Coomassie blue staining. Purity (62%) estimated by a Kodak Gel Logic 100 Imaging System; <i>lane</i> MW: PageRuler © Prestained Ladder (see Figure S1), <i>lane</i> 1: Enzyme (10 μ L of a ~4.6 mg/mL solution) and of B) Y125C/N446K/T95A/T97I/H109S- <i>Os</i> TAM after Coomassie blue staining. Purity (48%) estimated by a Kodak Gel Logic 100 Imaging System; <i>lane</i> MW: PageRuler © Prestained Ladder (see Figure S1), <i>lane</i> 1: Enzyme (5 μ L of a ~3.4 mg/mL solution).	58
Figure S5. SDS-PAGE gel of A) T95A/T97I/H109S/F115L- <i>Os</i> TAM after Coomassie blue staining. Purity (65%) estimated by a Kodak Gel Logic 100 Imaging System <i>lane</i> 1: Enzyme (10 μ L of a ~5.3 mg/mL solution), <i>lane</i> MW: PageRuler© Prestained Ladder (see Figure S1), and of B) Y125C/N446K/T95A/T97I/H109S/F115L- <i>Os</i> TAM after Coomassie blue staining. Purity (55%) estimated by a Kodak Gel Logic 100 Imaging System, <i>lane</i> MW: PageRuler© Prestained Ladder (see Figure S1), <i>lane</i> 1: Enzyme (5 μ L of a ~6.2 mg/mL solution).	59
Figure S6. Conversion of <i>p</i> -Br-phenyl- α -alanine (\circ) (3 mM) to <i>p</i> -Br-phenyl- β -alanine (Δ) and <i>p</i> -Br-cinnamate (\blacksquare) over 12 h by A) Y125C/N446K- <i>Os</i> TAM and B) N446K- <i>Os</i> TAM.	60
Figure S7. Conversion of α -phenylalanine (\circ) (3 mM) to β -phenylalanine (Δ) and cinnamate (\blacksquare) over 12 h by wild type- <i>Os</i> TAM.	60
Figure S8. EI-MS of ethyl ester of authentic (<i>E</i>)-cinnamate.	61
Figure S9. EI-MS of ethyl ester of (<i>E</i>)-cinnamate biocatalyzed by N446K- <i>Os</i> TAM from (2 <i>S</i>)- α -phenylalanine.	61
Figure S10. EI-MS of ethyl ester of authentic (<i>E</i>)- <i>p</i> -Br-cinnamate.	62
Figure S11. EI-MS of ethyl ester of (<i>E</i>)- <i>p</i> -Br-cinnamate biocatalyzed by N446K- <i>Os</i> TAM from (2 <i>S</i>)- α - <i>p</i> -Br-phenylalanine.	62
Figure S12. EI-MS of ethyl ester of authentic (<i>E</i>)- <i>p</i> -Cl-cinnamate.	63
Figure S13. EI-MS of ethyl ester of (<i>E</i>)- <i>p</i> -Cl-cinnamate biocatalyzed by N446K- <i>Os</i> TAM from (2 <i>S</i>)- α - <i>p</i> -Cl-phenylalanine.	63
Figure S14. EI-MS of ethyl ester of authentic (<i>E</i>)- <i>p</i> -F-cinnamate.	64
Figure S15. EI-MS of ethyl ester of (<i>E</i>)- <i>p</i> -F-cinnamate biocatalyzed by N446K- <i>Os</i> TAM from (2 <i>S</i>)- α - <i>p</i> -F-phenylalanine.	64
Figure S16. EI-MS of ethyl ester of authentic (<i>E</i>)- <i>p</i> -CH ₃ -cinnamate.	65

Figure S17. EI-MS of ethyl ester of (<i>E</i>)- <i>p</i> -CH ₃ -cinnamate biocatalyzed by N446K- <i>Os</i> TAM from (2 <i>S</i>)- α - <i>p</i> -CH ₃ -phenylalanine.	65
Figure S18. EI-MS of ethyl ester of authentic (<i>E</i>)- <i>p</i> -OCH ₃ -cinnamate.	66
Figure S19. EI-MS of ethyl ester of (<i>E</i>)- <i>p</i> -OCH ₃ -cinnamate biocatalyzed by N446K- <i>Os</i> TAM from (2 <i>S</i>)- α - <i>p</i> -OCH ₃ phenylalanine.	66
Figure S20. Michaelis-Menten kinetics plot for <i>p</i> -Br-cinnamic acid biocatalyzed by wild-type <i>Os</i> TAM. Standard error < 5%. $v = ([E] \times k_{cat} \times [S]) / (K_M + [S])$, where $K_M = 710 \mu\text{M}$, $k_{cat} = 0.014 \text{ s}^{-1}$	67
Figure S21. Michaelis-Menten kinetics plot for <i>p</i> -Cl-cinnamic acid biocatalyzed by wild-type <i>Os</i> TAM. Standard error < 5%. $v = ([E] \times k_{cat} \times [S]) / (K_M + [S])$, where $K_M = 708 \mu\text{M}$, $k_{cat} = 0.012 \text{ s}^{-1}$	67
Figure S22.. Michaelis-Menten kinetics plot for <i>p</i> -F-cinnamic acid biocatalyzed by wild-type <i>Os</i> TAM. Standard error < 5%. $v = ([E] \times k_{cat} \times [S]) / (K_M + [S])$, where $K_M = 713 \mu\text{M}$, $k_{cat} = 0.010 \text{ s}^{-1}$	68
Figure S23. Michaelis-Menten kinetics plot for cinnamic acid biocatalyzed by wild-type <i>Os</i> TAM. Standard error < 5%. $v = ([E] \times k_{cat} \times [S]) / (K_M + [S])$, where $K_M = 660 \mu\text{M}$, $k_{cat} = 0.013 \text{ s}^{-1}$	68
Figure S24. Michaelis-Menten kinetics plot for <i>p</i> -Br-cinnamic acid biocatalyzed by Y125C- <i>Os</i> TAM mutant. Standard error < 5%. $v = ([E] \times k_{cat} \times [S]) / (K_M + [S])$, where $K_M = 349 \mu\text{M}$, $k_{cat} = 0.021 \text{ s}^{-1}$	69
Figure S25. Michaelis-Menten kinetics plot for <i>p</i> -Cl-cinnamic acid biocatalyzed by Y125C- <i>Os</i> TAM mutant. Standard error < 5%. $v = ([E] \times k_{cat} \times [S]) / (K_M + [S])$, where $K_M = 377 \mu\text{M}$, $k_{cat} = 0.017 \text{ s}^{-1}$	69
Figure S26. Michaelis-Menten kinetics plot for <i>p</i> -F-cinnamic acid biocatalyzed by Y125C- <i>Os</i> TAM mutant. Standard error < 5%. $v = ([E] \times k_{cat} \times [S]) / (K_M + [S])$, where $K_M = 785 \mu\text{M}$, $k_{cat} = 0.012 \text{ s}^{-1}$	70
Figure S27. Michaelis-Menten kinetics plot for cinnamic acid biocatalyzed by Y125C- <i>Os</i> TAM. Standard error < 5%. $v = ([E] \times k_{cat} \times [S]) / (K_M + [S])$, where $K_M = 787 \mu\text{M}$, $k_{cat} = 0.006 \text{ s}^{-1}$	70
Figure S28. Michaelis-Menten kinetics plot for <i>p</i> -Br-cinnamic acid biocatalyzed by N446K- <i>Os</i> TAM mutant. Standard error < 5%. $v = ([E] \times k_{cat} \times [S]) / (K_M + [S])$, $K_M = 414 \mu\text{M}$, $k_{cat} = 0.048 \text{ s}^{-1}$	71
Figure S29. Michaelis-Menten kinetics plot for <i>p</i> -Cl-cinnamic acid biocatalyzed by N446K- <i>Os</i> TAM mutant. Standard error < 5%. $v = ([E] \times k_{cat} \times [S]) / (K_M + [S])$, where $K_M = 376 \mu\text{M}$, $k_{cat} = 0.040 \text{ s}^{-1}$	71

Figure S30. Michaelis-Menten kinetics plot for *p*-F-cinnamic acid biocatalyzed by N446K-*Os*TAM mutant. Standard error < 10%. $v = ([E] \times k_{cat} \times [S]) / (K_M + [S])$, where $K_M = 376 \mu\text{M}$, $k_{cat} = 0.040 \text{ s}^{-1}$72

Figure S31. Michaelis-Menten kinetics plot for cinnamic acid biocatalyzed by N446K-*Os*TAM. Standard error < 5%. $v = ([E] \times k_{cat}) / (K_M + [S])$, where $K_M = 503 \mu\text{M}$, $k_{cat} = 0.033 \text{ s}^{-1}$72

Figure S32. Michaelis-Menten kinetics plot for *p*-Br-cinnamic acid biocatalyzed by Y125C/N446K-*Os*TAM mutant. Standard error < 5%. $v = ([E] \times k_{cat} \times [S]) / (K_M + [S])$, where $K_M = 327 \mu\text{M}$, $k_{cat} = 0.018 \text{ s}^{-1}$73

Figure S33. Michaelis-Menten kinetics plot for *p*-Cl-cinnamic acid biocatalyzed by Y125C/N446K-*Os*TAM mutant. Standard error < 10%. $v = ([E] \times k_{cat} \times [S]) / (K_M + [S])$, where $K_M = 463 \mu\text{M}$, $k_{cat} = 0.016 \text{ s}^{-1}$73

Figure S34. Michaelis-Menten kinetics plot for *p*-F-cinnamic acid biocatalyzed by Y125C/N446K-*Os*TAM mutant. Standard error < 5%. $v = ([E] \times k_{cat} \times [S]) / (K_M + [S])$, where $K_M = 439 \mu\text{M}$, $k_{cat} = 0.016 \text{ s}^{-1}$74

Figure S35. Michaelis-Menten kinetics plot for cinnamic acid biocatalyzed by Y125C/N446K-*Os*TAM. Standard error < 5%. $v = ([E] \times k_{cat} \times [S]) / (K_M + [S])$, where $K_M = 494 \mu\text{M}$, $k_{cat} = 0.011 \text{ s}^{-1}$74

Figure S36. Michaelis-Menten kinetics plot for *p*-Br-cinnamic acid biocatalyzed by Y125C/N446K/T95A/T97I-*Os*TAM mutant. Standard error < 5%. $v = ([E] \times k_{cat} \times [S]) / (K_M + [S])$, where $K_M = 445 \mu\text{M}$, $k_{cat} = 0.047 \text{ s}^{-1}$75

Figure S37. Michaelis-Menten kinetics plot for *p*-Cl-cinnamic acid biocatalyzed by Y125C/N446K/T95A/T97I-*Os*TAM mutant. Standard error < 5%. $v = ([E] \times k_{cat} \times [S]) / (K_M + [S])$, where $K_M = 290 \mu\text{M}$, $k_{cat} = 0.046 \text{ s}^{-1}$75

Figure S38. Michaelis-Menten kinetics plot for *p*-F-cinnamic acid biocatalyzed by Y125C/N446K/T95A/T97I-*Os*TAM mutant. Standard error < 5%. $v = ([E] \times k_{cat} \times [S]) / (K_M + [S])$, where $K_M = 238 \mu\text{M}$, $k_{cat} = 0.021 \text{ s}^{-1}$76

Figure S39. Michaelis-Menten kinetics plot for cinnamic acid biocatalyzed by Y125C/N446K/T95A/T97I-*Os*TAM mutant. Standard error < 10%. $v = ([E] \times k_{cat} \times [S]) / (K_M + [S])$, where $K_M = 379 \mu\text{M}$, $k_{cat} = 0.023 \text{ s}^{-1}$76

Figure S40. Michaelis-Menten kinetics plot for *p*-Br-cinnamic acid biocatalyzed by T95A/T97I-*Os*TAM mutant. Standard error < 5%. $v = ([E] \times k_{cat} \times [S]) / (K_M + [S])$, where $K_M = 439 \mu\text{M}$, $k_{cat} = 0.025 \text{ s}^{-1}$77

Figure S41. Michaelis-Menten kinetics plot for *p*-Cl-cinnamic acid biocatalyzed by T95A/T97I-*Os*TAM mutant. Standard error < 5%. $v = ([E] \times k_{cat} \times [S]) / (K_M + [S])$, where $K_M = 458 \mu\text{M}$, $k_{cat} = 0.023 \text{ s}^{-1}$77

Figure S42. Michaelis-Menten kinetics plot for *p*-F-cinnamic acid biocatalyzed by T95A/T97I-*Os*TAM mutant. Standard error < 5%. $v = ([E] \times k_{cat} \times [S]) / (K_M + [S])$, where $K_M = 562 \mu\text{M}$, $k_{cat} = 0.015 \text{ s}^{-1}$78

Figure S43. Michaelis-Menten kinetics plot for cinnamic acid biocatalyzed by T95A/T97I-*Os*TAM mutant. Standard error < 5%. $v = ([E] \times k_{cat} \times [S]) / (K_M + [S])$, where $K_M = 311 \mu\text{M}$, $k_{cat} = 0.022 \text{ s}^{-1}$78

Figure S44. Percent conversion of β -phenylalanine analogs for A) N446K-*Os*TAM, B) Y125C-*Os*TAM, C) Y125C/N446K-*Os*TAM D) wild type-*Os*TAM E) T95A-*Os*TAM, and F) T97I-*Os*TAM were incubated with *para*-(\square), *meta*-(\blacktriangle), and *ortho*-(\circ)-substituted α -phenylalanines. The dotted line represents the percent yield β -phenylalanine analogs, and the solid line shows the percent yield of β -tyrosine. Standard error = $\pm 5\%$; n = 3.79

Figure S45. Percent conversion of β -phenylalanine analogs for A) T95A/T97I-*Os*TAM, B) Y125C/N446K/T95A-*Os*TAM, C) Y125C/N446K/T95I-*Os*TAM, and D) Y125C/N446K/T95A/T97I-*Os*TAM were incubated with *para*-(\square), *meta*-(\blacktriangle), and *ortho*-(\circ)-substituted α -phenylalanines. The dotted line represents the percent yield β -phenylalanine analogs, and the solid line shows the percent yield of β -tyrosine. Standard error = $\pm 5\%$; n = 3. 80

Figure S46. Percent conversion of β -phenylalanine analogs for A) H109S-*Os*TAM, B) N446K/H109S-*Os*TAM, C) T95A/T95I/H109S-*Os*TAM, and D) Y125C/N446K/T95A/T97I/H109S-*Os*TAM were incubated with *para*-(\square), *meta*-(\blacktriangle), and *ortho*-(\circ)-substituted α -phenylalanines. The dotted line represents the percent yield β -phenylalanine analogs, and the solid line shows the percent yield of β -tyrosine. Standard error = $\pm 5\%$; n = 3. 81

Figure S47. The percent yield of *trans*-cinnamate analogs made biocatalytically from A) H109S-*Os*TAM, B) N446K/H109S-*Os*TAM, C) T95A/T97I/H109S-*Os*TAM, D) Y125C/N446K/T95A/T97I/H109S-*Os*TAM, E) F115L-*Os*TAM, and F) N446K/F115L-*Os*TAM incubated with *p*-(\square), *m*-(\blacktriangle), and *o*-(\circ)-substituted α -phenylalanines. The dashed line shows the percent yield of cinnamic acid from phenylalanine, and the solid line shows the percent yield of coumaric acid from tyrosine. Standard error = $\pm 5\%$; n = 3.82

Figure S48. Percent conversion of β -phenylalanine analogs made biocatalytically from A) F115L-*Os*TAM, B) N446K/F115L-*Os*TAM, C) T95A/T97I/F115L-*Os*TAM D) Y125C/N446K/T95A/T97I/F115L-*Os*TAM E) T95A/T97I/H109S/F115L-*Os*TAM, and F) Y125C/N446K/T95A/T97I/H109S/F115L-*Os*TAM were incubated with *para*-(\square), *meta*-(\blacktriangle), and *ortho*-(\circ)-substituted α -phenylalanines. The dotted line represents the percent yield β -phenylalanine analogs, and the solid line shows the percent yield of β -tyrosine. Standard error = $\pm 5\%$; n = 3.83

Figure S49. The percent yield of *trans*-cinnamate analogs made biocatalytically from A) T95A-*Os*TAM, B) T97I-*Os*TAM, C) T95A/T97I/F115L-*Os*TAM, D) Y125C/N446K/T95A/T97I/F115L-*Os*TAM, E) T95A/T97I/H109S/F115L-*Os*TAM, and F) Y125C/N446K/T95A/T97I/H109S/F115L-*Os*TAM were incubated with *para*-(\square), *meta*-(\blacktriangle), and *ortho*-(\circ)-substituted α -phenylalanines. The dashed line shows the percent yield of cinnamic

acid from phenylalanine, and the solid line shows the percent yield of coumaric acid from tyrosine. Standard error = $\pm 5\%$; $n = 3$84

Figure 4.1. Important alkylpyrazines (AlkPyr), Acylpyrazines (AcylPyr), and alkyl/alkoxy-pyrazines (Alk/AlkO-Pyr) in food chemistry.87

Figure 4.2. A) HPLC chromatogram of 1:1 mixture of commercial 10 and 11 (mobile phase: 20:80 CH₃CN/H₂O on an Alltech Econosil C-18 column, 10 μ (250 mm \times 22 mm) with a 5 mL/min flow rate with A₂₇₈ monitoring of the effluent. B) GC/EI-MS profiles (selected-ion mode, m/z 136) of 1:1 mixture of commercial 10 and 11, C) purified 325-EDMP (11) and D) 235-EDMP (10).98

Figure 4.3. Key structural ²J_{CH} and ³J_{CH} HMBC correlations within A) 235-EDMP (10) and B) 325-EDMP (11) between carbon (●) and hydrogen (shown explicitly as bold and underlined). The pyrazine ring numbering is shown.100

Figure 4.4. A representative partial GC/EI-MS chromatogram with selected-ion monitoring (m/z 136) of 235- and 325-EDMP at 50:50 relative abundance in the product mixture after incubating 1,2-diaminopropane and pentan-2,3-dione (dropwise addition) at 0 °C for 1 h and then air oxidation.101

Figure 4.5. A) The GC/EI-MS selected-ion (m/z 102) profile of the crude product extracted from the reaction mixture after incubating PDC, propanal, and pyruvate to make 3-hydroxypentan-2-one. B) The compound eluting at $R_t = 5.29$ min in *Panel A* had EI-MS fragment ions consistent with the α -cleavage sites of 3-hydroxypentan-2-one. The compound eluting at $R_t = 5.43$ min in *Panel A* had EI-MS fragment ions consistent with α -cleavage sites of 2-hydroxypentan-3-one (see Figure 4.6B). C) The GC/EI-MS total ion chromatogram of the crude product described for *Panel A*. Putative compounds within the biocatalysis-derived sample whose peak thresholds were greater than or equal to those for the hydroxypentanones at $R_t = 5.29$ min and 5.43 min and had relative fragment ions abundances like those listed in a spectral database (see Figure S61 - Figure S63 for fragment ion profiles.^{47,48} The coupled carbon-chain moieties originating from propanal are highlighted with bold C-C bonds.106

Figure 4.6. A) The GC/EI-MS selected-ion (m/z 102) profile of the crude product extracted from the reaction mixture after incubating PDC, acetaldehyde, and 2-oxobutanoate to make 2-hydroxypentan-3-one. B) The compound eluting at $R_t = 5.43$ min in *Panel A* had EI-MS fragment ions consistent with the α -cleavage sites of 2-hydroxypentan-3-one. The compound eluting at $R_t = 5.29$ min in *Panel A* had EI-MS fragment ions consistent with α -cleavage sites of 3-hydroxypentan-2-one (see Figure 4.5). C) The GC/EI-MS total ion chromatogram of the crude product described for *Panel A*. A compound ($R_t = 4.85$ min) within the biocatalysis-derived sample whose peak threshold was approximately equal to those for the hydroxypentanones at $R_t = 5.29$ min and 5.43 min and had relative fragment ions abundances like those listed in a spectral database⁵⁰ (see Figure S64 for fragment ion profile). The coupled carbon-chain moieties originating from acetaldehyde are highlighted with bold C-C bonds.108

Figure 4.7. Partial GC/EI-MS chromatograms with selected-ion monitoring of the dihydropyrazines (m/z 138) in the product mixture after incubating propane-1,2-diamine (8) with A) 2-hydroxypentan-3-one (17) and B) 3-hydroxypentan-2-one (18). Partial GC/EI-MS profile with selected-ion monitoring of the EDMPs (m/z 136) after air-oxidation of the dihydropyrazines in the sample analyzed C) in <i>Panel A</i> and D) in <i>Panel B</i>	110
Figure 4.8. GC/EI-MS total ion chromatogram (TIC) of products isolated from the crude reaction mixture after incubating 1,2-diaminopropane with A) 2-hydroxy-3-pentanone and B) 3-hydroxy-2-pentanone. The EDMPs 10 (~5.40 min) and 11 (5.49 min) are highlighted. C) EI-MS fragmentation profile of compound eluting from the GC at 4.60 min in the TIC profile (<i>Panel A</i>); D) a similar fragmentation ion profile was identified for 2,6-dimethylpiperazine in a mass spectral database. ⁵³ E) EI-MS fragmentation profile of peak eluting from the GC at 4.79 min in the TIC profile (<i>Panel A</i>); F) a similar fragmentation ion profile was identified in a mass spectral database for 2,5-dimethylpiperazine. ⁵⁴	113
Figure S50. ¹ H NMR (500 MHz, D ₂ O) of 235-EDMP.	117
Figure S51 ¹³ C NMR (126 MHz, D ₂ O) of 235-EDMP.....	117
Figure S52. ¹ J _{C,H} (¹³ C- ¹ H HSQC, D ₂ O) spectrum of 235-EDMP. Correlation data is summarized in Table S3.	118
Figure S53. ² J _{C,H} , ³ J _{C,H} (¹³ C- ¹ H HMBC) spectrum of 235-EDMP. Correlation data are summarized in Table S11.....	119
Figure S54. ¹ H NMR (500 MHz, D ₂ O) of 325-EDMP.....	121
Figure S55. ¹³ C NMR (126 MHz, D ₂ O) of 325-EDMP.....	121
Figure S56. ¹ J _{C,H} (¹³ C- ¹ H HSQC, D ₂ O) correlation spectrum of 325-EDMP. Correlation data are summarized in Table S9.....	122
Figure S57. ² J _{C,H} , ³ J _{C,H} (¹³ C- ¹ H HMBC) correlation spectrum of 325-EDMP. Correlation data are summarized in Table S10.....	123
Figure S58. ¹ H NMR analysis (¹ H NMR, 500 MHz, CDCl ₃) of 2-hydroxy-3-pentanone in a crude sample extracted (Et ₂ O) from a reaction mixture incubated with PDC, acetaldehyde, and 2-oxobutanoate sodium salt for 48 h. δ : 4.86 (1H, quartet, $J = 6.9$ Hz), 3.01 (2H, quartet, $J = 7.1$ Hz), 1.43 (3H, doublet, $J = 7.0$ Hz), 1.18 (3H, triplet, $J = 6.5$ Hz).	125
Figure S59. Reference homonuclear ⁴⁶ ¹ H- ¹ H COSY data for 3-hydroxy-2-hexanone1 used to predict the chemical shift correlations of 3-hydroxy-2-pentanone made via a carboligation reaction catalyzed by a pyruvate decarboxylase in the current study. Homonuclear correlations between H3 and H1, H4, H5, and H7 (bold circles) and annotated highlighted because these were the most diagnostic for identifying ¹ H- ¹ H correlations in 3-hydroxy-2-pentanone (Figure S60). Other correlations are circled and annotated.	126

Figure S60. ^1H - ^1H COSY analysis (500 MHz, CDCl_3) of the putative biocatalyzed 3-hydroxy-2-pentanone in a crude sample extracted (Et_2O) from a reaction mixture in which PDC, propanal, and 2-oxopropanoate sodium salt were incubated for 48 h. Putative correlations between H5 and H4 are circled and annotated off-diagonal.127

Figure S61. *Left panel*: GC/EI MS of the compound eluting at 5.74 min in the TIC of the crude 3-hydroxy-2-pentanone sample (Figure 4.5 of the main text) whose fragment ions correspond approximately with those for *Right panel*: 2-methyl-2-pentenal in the mass spectral database.⁴⁸128

Figure S62. *Left panel*: GC/EI MS of the compound eluting at 7.93 min in the TIC of the crude 3-hydroxy-2-pentanone sample (Figure 4.5 of the main text) whose fragment ions correspond approximately with those for *Right panel*: 3-hydroxy-2-methylpentanal in the mass spectral database.⁴⁸128

Figure S63. *Left panel*: GC/EI MS of the compound eluting at 12.15 min in the TIC of the crude 3-hydroxy-2-pentanone sample (Figure 4.5 of the main text) whose fragment ions correspond approximately with those for *Right panel*: 2,6-diethyl-5-methyl-1,3-dioxane in the mass spectral database.⁴⁹129

Figure S64. *Left panel*: GC/EI MS of the compound eluting at 4.85 min in the TIC of the 2-hydroxy-3-pentanone sample (Figure 4.6 of the main text) whose fragment ions correspond approximately with those for *Right panel*: paraldehyde in the mass spectral database.⁵⁰129

Figure S65. GC/EI-MS analysis in A) total-ion count (TIC) mode, (B) selected-ion monitoring (SIM) mode for the EDMPs (m/z 136), and C) SIM mode (m/z 80) for the pyrazine core minus the alkyl substituents of the product mixture after incubating 1,2-diaminopropane and 2-hydroxy-3-pentanone. The products (boxed) are characterized in Figure 4.8 of the main text.130

Figure S66. GC/EI-MS analysis in A) TIC mode, (B) SIM mode for the EDMPs (m/z 136), and (C) SIM mode (m/z 80) for the pyrazine core minus the alkyl substituents of the product mixture after incubating 1,2-diaminopropane and 3-hydroxy-2-pentanone. The products (boxed) are characterized in Figure 4.8 of the main text.131

Figure S67. EI-MS fragmentation profile of peaks eluting from the GC (TIC profile in Figure 4.8A of the main text) at A) 3.87 min, B) 4.12 min, C) 4.52 min, deduced from related azo-compounds,⁵² and D) 7.52 min, which corresponded to a putative alkyl ester with a molecular formula of $\text{C}_9\text{H}_{16}\text{O}_2$. EI-MS fragmentation profile of peaks eluting from the GC (TIC profile in Figure 4.8B of the main text) at E) 3.73 min and F) 4.43 min. The fragment ions in *Panels A – C, E, F* are inferred from those in Figure 4.8 of the main text and a previous document.⁵²132

LIST OF SCHEMES

- Scheme 4.1. A) a) H₂, b) dehydration/oxidation.²⁰ B) a) deaminocyclisation and Cu₂Cr₂O₅ dehydrogenation.²¹ C) a) thioalk/phenoxide or alk/phenoxide nucleophiles, methylpyrrolidone, microwave radiation.²² D) Example of coupling a diamine and diketone to make a 50:50 mixture of 235-EDMP/325-EDMP isomers. a) rt, 1 h, Et₂O, KOH. E) Proposed 325-EDMP biosynthesis in *Serratia marcescens* from L-threonine (12), showing a self-condensation step of 13. a) oxidation/decarboxylation; b) spontaneous iminization condensation; c) tautomerization; d) acetyltransferase/Acetyl CoA, reductase (H⁻/H⁺); e) dehydratase, O₂. F) Proposed 235-EDMP biosynthesis from mixed aminocarbonyl compounds, showing intermediates and products from self- and cross condensation. Steps b – e) are the same as in *Panel E*.89
- Scheme 4.2. a) isoamyl nitrite, conc HCl, Et₂O, 10-20 °C, 2 h; b) allylamine, hexane, reflux; c) potassium tert-butoxide, DMSO, 50 °C, 1-2 h; d) ClCOOCH₃, Et₃N, CH₂Cl₂, 10-20 °C; e) short contact-time pyrolysis in toluene solution at ~300 °C.....92
- Scheme 4.3. A proposed mechanism for the formation of 5,6-dihydropyrazine intermediates toward pyrazines from condensation between acylloins and 1,2-propanediamine: *a*) condensation between the less hindered amine with the keto group of the hydroxyketone substrate, *b*) proton transfer and dehydration, *c*) enolization and tautomerization, and *d*) condensation between the internal amine and the keto group.....103
- Scheme 4.4. Synthesis of hydroxypentanones (17 and 18) from the appropriate aldehyde and oxoalkanoate incubated with a) pyruvate decarboxylase (PDC), MgSO₄, and thiamine diphosphate in sodium citrate buffer.....103

KEY TO ABBREVIATIONS

AMs : Aminomutases

SAM : S-adenosyl methionine

PLP: Pyridoxal-5'-phosphate

AdoCbl : Adenosylcobalamin

2,3-GAM : glutamate 2,3-aminomutase

A/T/S : Alanine/ Threonine/ Serine

MIO : 4-methylidene-1H-imidazol-5(4H)-one

AL : Ammonia Lyase

PAM : phenylalanine aminomutases

TAM : tyrosine aminomutases

UCSF: University of California-San Francisco

PCR: Polymerase chain reaction

PDB: Protein data bank

SDS-PAGE: Sodium dodecyl sulfate-polyacrylamide gel electrophoresis

NMR: Nuclear Magnetic Resonance

IPTG: Isopropyl- β -D-thiogalactopyranoside

PDC : pyruvate decarboxylase

EDMP : Ethyl Dimethyl Pyrazine

DMSO: Dimethyl sulfoxide

CH₃CN : Acetonitrile

ESI: Electrospray ionization

EtOAc: Ethyl acetate

EtOH: Ethanol

GC/EI-MS: Gas chromatography electron ionization mass spectrometry

E. coli: Escherichia coli

ESI: Electrospray ionization

KOH: Potassium hydroxide

MgSO₄: Magnesium Sulfate

Chapter 1 . Overview of Aminomutase Enzyme.

1.1 Applications of Aminomutase Enzymes in Pharmaceutical Industry

Aminomutases (AMs) catalyze the chemically challenging isomerization of α - to β -amino acids by exchanging a vicinal hydrogen atom and amine group^{3,4} The existence of aminomutases in nature was initially recognized in 1970 when the metabolism of lysine was found to proceed through β -lysine in *Clostridium subterminale* SB4 and *Clostridium sticklandii*.⁵ The high enantio- and regioselectivity of these enzymes make them attractive to biosynthesizing chiral β -amino acid products. β -Amino acids are scarcely found in nature, but are essential components of biologically active natural products (Figure 1.1) such as the anticancer drug Taxol,⁶ amino peptidase inhibitor bestatin,⁵ antibiotic andrimid,⁷ anticancer agent bleomycin made by *Streptomyces*,⁸ and cytotoxic microcystin made by cyanobacteria.⁹ The antibiotic kirromycin from *Streptomyces collins*¹⁰ and nakinadines from the Okinawan marine sponge *Amphimedon sp.*,¹⁰ which showed cytotoxicity against leukemia, are recent discoveries¹¹ of natural products containing a β -amino acid moiety.

Several methods are described for the stereoselective chemical synthesis of β -amino acids, such as Arndt–Eistert homologation,¹² which involves the use of carcinogenic diazomethane reagents and Ag byproduct. This produces significant chemical waste during the multistep synthesis on an industrial scale. For this reason, biocatalysts can be integrated into large-scale chemical synthesis of β -amino acids and potentially play a significant role toward reducing harmful waste products.

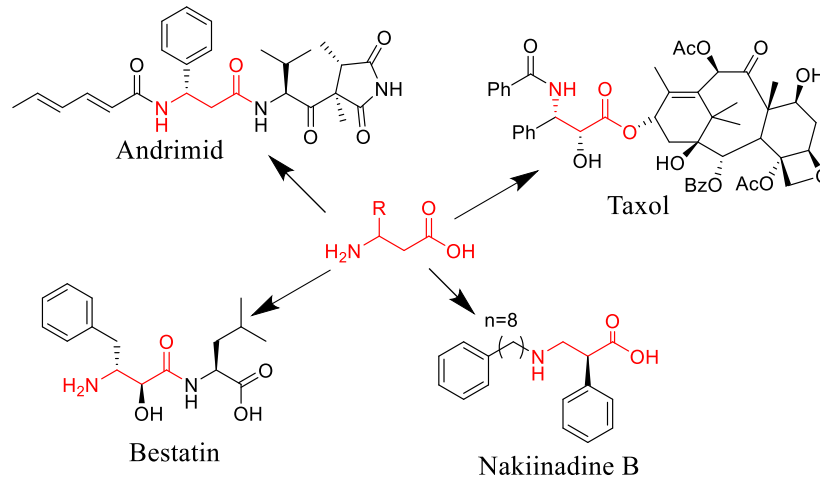


Figure 1.1. Natural products containing β -amino acids.

1.2 Aminomutases Classification based on Mechanism

Aminomutase are classified into three main categories based on their catalytic mechanisms: 1) adenosylcobalamin-dependent,¹³ 2) S-adenosyl methionine (SAM)-dependent,¹⁴ and 3) methylidene-imidazole-5-one-dependent.¹⁵

1.2.1 Adenosylcobalamin (AdoCbl) dependent aminomutase.

Anaerobic bacteria, such as *C. sticklandii* contain adenosylcobalamin-dependent aminomutases that are involved in the catabolism of amino acids. In the oxidative pathway that operates in these organisms, the primary substrate L-lysine undergoes amino group migration reaction that is catalyzed by an AdoCbl-dependent 5,6-aminomutase. The mechanism of adenosylcobalamin-based aminomutase depends on a radical mechanism. The initiator radical 5'-deoxyadenosyl is produced by homolytic cleavage of the Co-C (30 kcal/mol) bond of adenosylcobalamin (coenzyme B12).¹³ Pyridoxal phosphate is needed as a co-factor to catalyze the migration of the ω -amino group from C5 and C4 of D-ornithine (Figure 1.2). X-ray crystallographic studies showed that adenosylcobalamin-dependent aminomutases have a

heterotetrameric structure. Each α/β subunit harbors a Rossmann-like domain that binds AdoCbl and a PLP-binding triosephosphate isomerase-like (TIM) barrel.

1.2.2 S-Adenosylmethionine (SAM)-dependent aminomutases.

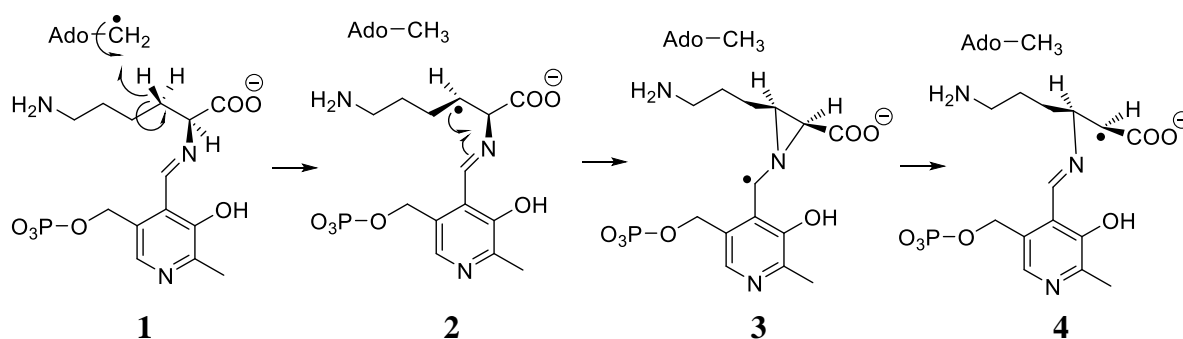


Figure 1.2. Partial lysine 2,3-aminomutase (LAM) mechanism. Ado-CH₂• is an adenosyl radical. Imine of lysine and pyridoxal (**1**) proceeding to the β -amino acid precursor radical (**4**) via the β -amino acid pyridoxal imine radical (**2**) and the pyridoxal aziridine radical (**3**).

The mechanism of SAM-dependent aminomutases is similar to that of AdoCbl dependent aminomutase mechanism (Figure 1.2). SAM-dependent aminomutases contain, 5'-deoxyadenosyl moieties from SAM as the radical initiator, pyridoxal phosphate and an iron-sulfur cluster ([4Fe-4S]). This aminomutase catalyzes the migration of amine group in between α and β carbon atoms in lysine. In anaerobic bacteria, this enzyme plays a role in the utilization of lysine for growth. Another member of this group is glutamate 2,3-aminomutase (2,3-GAM), which is widespread in bacterial and archaeal species. It is proposed to be involved in generating β -glutamate, which serves as an osmoregulator, and in the metabolism of α -glutamate.

1.2.3 Methylideneimidazole-5-one-dependent aminomutases.

A subclass of AMs belongs to a class I lyase-like family that utilize a 3,5-dihydro-5-methylidene-4*H*-imidazol-4-one prosthetic group in the active site to catalyze the isomerization. The electrophilic MIO forms post-translationally through self-cyclization and dehydration of a backbone tripeptide A/T/S-Ser-Gly (Figure 1.3).¹⁶

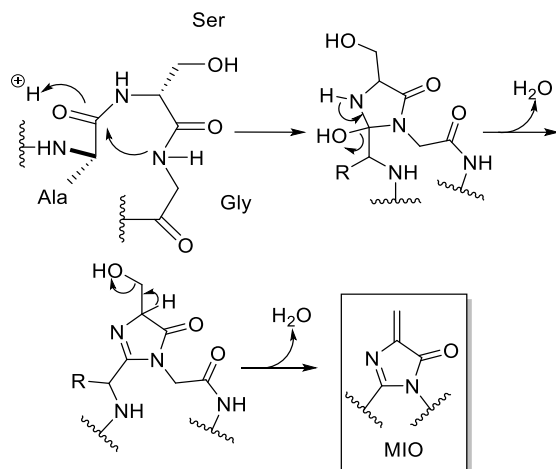


Figure 1.3 Autocatalysis of the 3,5-dihydro-5-methylidene-4H-imidazol-4-one cofactor through cyclization of (A/T/S)-Ser-Gly residues within the active site.

The MIO assists in the elimination of the NH_2 from the α -amino acid substrates by forming an NH_2 -MIO adduct. Removal of the vicinal proton from the substrate (NH_2 -MIO adduct) catalyzed by a tyrosine residue yields an acrylate intermediate, which is reaminated at the β -position to produce β -amino acids (Figure 1.4). The aminomutases likely evolved from the ancestral ammonia lyases (AL), which also belong to the MIO class I like catalysts. The lyases terminate their reactions at the acrylate intermediate.¹⁵

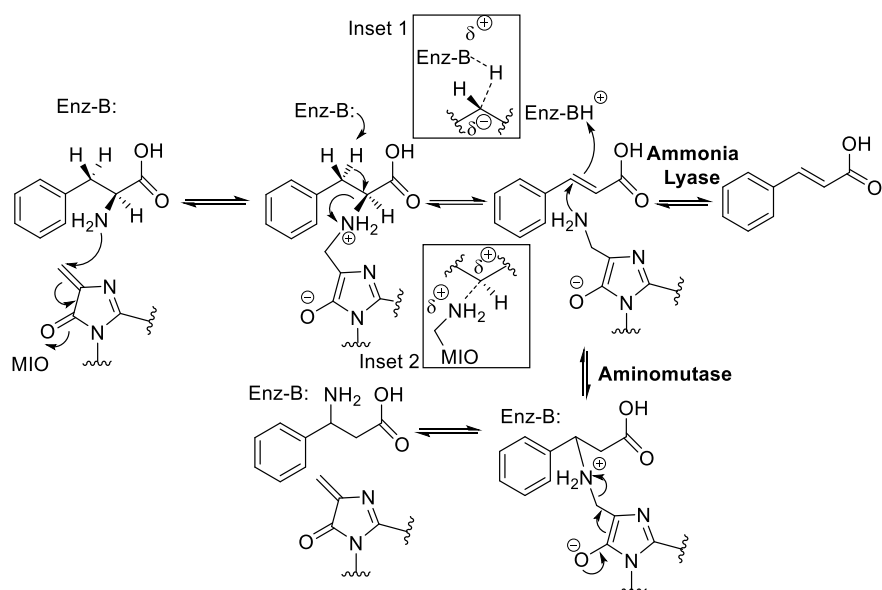


Figure 1.4. Mechanism of MIO-dependent aminomutase and ammonia lyase enzymes. Inset 1: Carbanionic transition state intermediate at β -carbon of the substrate. Inset 2: Cationic transition state intermediate at α -carbon of the substrate.

1.3 Subclasses of MIO AMs

Currently, MIO-dependent AMs split into two classes based on their substrate preference: phenylalanine aminomutases (PAM) and tyrosine aminomutases (TAM). Earlier substrate specificity studies showed that PAMs convert substituted aromatic and heteroaromatic α -phenylalanines to the corresponding β -phenylalanines and generally do not accept tyrosine as a substrate. There are three known PAMs: *PaPAM* (*Pantoea agglomerans*), *TcPAM*¹⁷ (*Taxus canadensis*) and *EncP*¹⁸ (*Streptomyces maritimus*).

Based on the stereochemical mechanism studies of MIO enzymes¹⁵⁻¹⁶ the PAM family is divided into two classes (EC 5.4.3.10 and EC 5.4.3.11) based on the *R* and *S* enantioselectivity of the amino acid product, respectively. *TcPAM* from *Taxus canadensis*¹⁷ makes (*R*)- β -phenylalanine. *TcPAM* initiates its reaction by heterolytically removing C_{β} -H and C_{α} -NH₂ from

the substrate. Rotation of the cinnamate intermediate, exchange, and reattachment of H and NH₂ at C_α and C_β, respectively, result in the anti-migration product.¹⁷ By contrast, the mechanisms of *Pa*PAM from *Pantoea agglomerans*,¹⁹ *EncP* from *Streptomyces maritimus*,¹⁸ and *Pf*PAM from *Pseudomonas fluorescens*²⁰ make (*S*)-β-phenylalanine. For example, *Pa*PAM removes and interchanges C_β-H and C_αNH₂ of the substrate and then reattaches them to a nonrotatable cinnamate intermediate. This mechanism reattaches the H and NH₂ to C_α and C_β, respectively, resulting in the syn-migration product.¹⁹ It is also important to note these PAM family members catalyze their reaction at ~100% enantioselectivity.^{17, 19}

The PAM family members catalyze their reaction with higher enantioselectivity (~100% selectivity). By contrast, TAMs require the 4'-hydroxyl group on the aromatic ring of the substrate for catalysis and generally do not accept phenylalanine as a substrate. Thus, the substrate selectivity of TAMs is limited compared to that of PAMs, and the enantiomeric excess is often variable (85-95% ee under the steady state reaction conditions) for the three different MIO TAMs identified so far. The mode of migration, reaction stereochemistry, and kinetic parameters have been characterized for *Sg*TAM from *Streptomyces globisporus*,²¹ *Cc*TAM from *Chondromyces crocatus*,²² *Os*TAM from

Oryza sativa,²³ and *KedY*₄ from *Streptoalloteichus sp.*,²⁴ while those for *Mx*TAM (*Myxococcus sp.* Mx-BO), *Mf*TAM (*Myxococcus fulvus*) and *Am*TAM (*Antinomadura madurae*)²² have not yet been fully determined. The *S*-enantioselectivity of the latter three aminomutases is preliminary while the enantioselectivities of *Cc*TAM, *Os*TAM, and *KedY*₄ preferentially make the (*R*)-β-antipode.

REFERENCES

REFERENCES

1. Walter, T.; Wijewardena, D.; Walker, K. D., Mutation of Aryl Binding Pocket Residues Results in an Unexpected Activity Switch in an *Oryza sativa* Tyrosine Aminomutase. *Biochemistry* **2016**, *55* (25), 3497-3503.
2. Ma, Y.-J.; Wu, J.-H.; Li, X.; Xu, X.-B.; Wang, Z.-Y.; Wu, C.; Du, M.; Song, L., Effect of Alkyl Distribution in Pyrazine on Pyrazine Flavor Release in Bovine Serum Albumin Solution. *RSC Advances* **2019**, *9* (63), 36951-36959.
3. Morley, C.; Stadtman, T., Studies on the Fermentation of D-alpha-Lysine. Purification and Properties of an Adenosine Triphosphate Regulated B 12-coenzyme-dependent D-alpha-Lysine Mutase Complex from *Clostridium sticklandii*. *Biochemistry* **1970**, *9* (25), 4890.
4. Liu, W.; Shen, B., Genes for Production of the Enediyne Antitumor Antibiotic C-1027 in *Streptomyces globisporus* are Clustered with the *cagA* Gene that Encodes the C-1027 Apoprotein. *Antimicrobial Agents and Chemotherapy* **2000**, *44* (2), 382-392.
5. Velmourougane, G.; Harbut, M. B.; Dalal, S.; McGowan, S.; Oellig, C. A.; Meinhardt, N.; Whisstock, J. C.; Klemba, M.; Greenbaum, D. C., Synthesis of New (-)-bestatin-based Inhibitor Libraries Reveals a Novel Binding Mode in the S1 Pocket of the Essential Malaria M1 Metalloaminopeptidase. *Journal of medicinal chemistry* **2011**, *54* (6), 1655-1666.
6. Walker, K. D.; Klettke, K.; Akiyama, T.; Croteau, R., Cloning, Heterologous Expression, and Characterization of a Phenylalanine Aminomutase Involved in Taxol Biosynthesis. *Journal of Biological Chemistry* **2004**, *279* (52), 53947-53954.
7. Jin, M.; Fischbach, M. A.; Clardy, J., A Biosynthetic Gene Cluster for the Acetyl-CoA Carboxylase Inhibitor Andrimid. *Journal of the American Chemical Society* **2006**, *128* (33), 10660-10661.
8. Umezawa, H.; Maeda, K.; Takeuchi, T.; Okami, Y., New Antibiotics, bleomycin A and B. *The Journal of antibiotics* **1966**, *19* (5), 200-209.
9. Botes, D. P.; Tuinman, A. A.; Wessels, P. L.; Viljoen, C. C.; Kruger, H.; Williams, D. H.; Santikarn, S.; Smith, R. J.; Hammond, S. J., The Structure of Cyanoginosin-LA, a Cyclic Heptapeptide Toxin from the Cyanobacterium *Microcystis aeruginosa*. *Journal of the Chemical Society, Perkin Transactions 1* **1984**, 2311-2318.
10. Nishi, T.; Kubota, T.; Fromont, J.; Sasaki, T.; Kobayashi, J. i., Nakinadines B-F: New Pyridine Alkaloids with a β -amino Acid Moiety from Sponge *Amphimedon* sp. *Tetrahedron* **2008**, *64* (14), 3127-3132.
11. Kudo, F.; Miyanaaga, A.; Eguchi, T., Biosynthesis of Natural Products Containing β -amino Acids. *Natural product reports* **2014**, *31* (8), 1056-1073.

12. Pinho, V. D.; Gutmann, B.; Kappe, C. O., Continuous Flow Synthesis of β -amino Acids from α -amino Acids via Arndt–Eistert Homologation. *RSC advances* **2014**, *4* (70), 37419-37422.
13. Chirpich, T.; Zappia, V.; Costilow, R.; Barker, H., Lysine 2, 3-Aminomutase Purification and Properties of a Pyridoxal Phosphate and S-adenosylmethionine-activated Enzyme. *Journal of Biological Chemistry* **1970**, *245* (7), 1778-1789.
14. Frey, P. A.; Reed, G. H., Radical Mechanisms in Adenosylmethionine-and Adenosylcobalamin-dependent Enzymatic Reactions. *Archives of Biochemistry and Biophysics* **2000**, *382* (1), 6-14.
15. Givot, I.; Smith, T.; Abeles, R. H., Studies on the Mechanism of Action and the Structure of the Electrophilic Center of Histidine Ammonia Lyase. *Journal of Biological Chemistry* **1969**, *244* (23), 6341-6353.
16. Schwede, T. F.; Rétey, J.; Schulz, G. E., Crystal Structure of Histidine Ammonia-lyase Revealing a Novel Polypeptide Modification as the Catalytic Electrophile. *Biochemistry* **1999**, *38* (17), 5355-5361.
17. Mutatu, W.; Klettke, K. L.; Foster, C.; Walker, K. D., Unusual Mechanism for an Aminomutase Rearrangement: Retention of Configuration at the Migration Termini. *Biochemistry* **2007**, *46* (34), 9785-9794.
18. Weise, N. J.; Parmeggiani, F.; Ahmed, S. T.; Turner, N. J., The Bacterial Ammonia Lyase EncP: a Tunable Biocatalyst for the Synthesis of Unnatural Amino Acids. *Journal of the American Chemical Society* **2015**, *137* (40), 12977-12983.
19. Ratnayake, N. D.; Wanninayake, U.; Geiger, J. H.; Walker, K. D., Stereochemistry and Mechanism of a Microbial Phenylalanine Aminomutase. *Journal of the American Chemical Society* **2011**, *133* (22), 8531-8533.
20. Csuka, P.; Juhász, V.; Kohári, S.; Filip, A.; Varga, A.; Sátorhelyi, P.; Bencze, L. C.; Barton, H.; Paizs, C.; Poppe, L., Pseudomonas Fluorescens Strain R124 Encodes Three Different MIO Enzymes. *ChemBioChem* **2018**, *19* (4), 411-418.
21. Christenson, S. D.; Liu, W.; Toney, M. D.; Shen, B., A Novel 4-methylideneimidazole-5-one-Containing Tyrosine Aminomutase in Eneidyne Antitumor Antibiotic C-1027 Biosynthesis. *Journal of the American Chemical Society* **2003**, *125* (20), 6062-6063.
22. Krug, D.; Müller, R., Discovery of Additional Members of the Tyrosine Aminomutase Enzyme Family and the Mutational Analysis of CmdF. *ChemBioChem* **2009**, *10* (4), 741-750.
23. Walter, T.; King, Z.; Walker, K. D., A Tyrosine Aminomutase from Rice (*Oryza sativa*) Isomerizes (S)- α -to (R)- β -tyrosine with Unique High Enantioselectivity and Retention of Configuration. *Biochemistry* **2015**, *55* (1), 1-4.

24. Huang, S.-X.; Lohman, J. R.; Huang, T.; Shen, B., A New Member of the 4-methylideneimidazole-5-one-Containing Aminomutase Family from the Eneidyne kedarcidin Biosynthetic Pathway. *Proceedings of the National Academy of Sciences* **2013**, *110* (20), 8069-8074.

Chapter 2 . Tyrosine Aminomutase Derived from *Oryza sativa*.

Reprinted (adapted) with permission from (Attanayake, G. K.; Walter, T.; Walker, K. D., Understanding which residues of the active site and loop structure of a tyrosine aminomutase define its mutase and lyase activities. *Biochemistry*. 2018, 57 (25), 3503-3514.) Copyright (2018) American Chemical Society.

2.1 Introduction

Recent studies on *Os*TAM, the first TAM isolated from a plant (other TAMs have bacterial origins), showed that it isomerizes (2*S*)- α - to (3*R*)- β -tyrosine with higher enantioselectivity (94% ee)¹ than that of other fully characterized TAMs. This high enantioselectivity is similar to that catalyzed by *Tc*PAM (another plant-derived MIO-aminomutase), which makes (3*R*)- β -phenylalanine with exceptionally high enantioselectivity (~100% ee)² and shares high sequence identity with the active site of *Os*TAM. This high sequence identity may in part help explain the unusual, although slight, 3% native PAM activity of *Os*TAM.³

2.2 Objective

Based on the high sequence similarity and the virtually identical enantioselectivities between the plant-derived *Os*TAM and *Tc*PAM, We hypothesized that *Os*TAM could be converted to a functional PAM through straightforward active site mutations.⁴ This conversion to a PAM was foreseen as a strategy to expand the substrate scope of *Os*TAM to include different substituted phenylalanines as substrates and reduce the limitation of needing a hydroxyaryl substrate. While pursuing this objective, we also looked to 1) discern the structural and chemical features within the *Os*TAM active site and active site loop (functioning as a "lid") that governs its high enantioselectivity, and 2) dissect the principles that parse MIO ammonia lyase and aminomutase activities.

Understanding these factors are critical for manipulating the properties of MIO-dependent enzymes for potential use in various biotechnological applications.⁵

2.3 Experimental

2.3.1 Chemicals and Reagents.

(3*R*)- β -Tyrosine and (3*R*)- β -phenylalanine were obtained from Peptech (Burlington, MA). All other chemicals and reagents were obtained from Sigma-Aldrich (St. Louis, MO) and used without further purification unless noted otherwise.

2.3.2 OsTAM Mutations.

Point mutations of the *OsTAM* gene were generated by the QuickChange Multi Site-Directed Mutagenesis Kit (Stratagene) using the buffers, enzymes, and dNTP mix provided. To make each single *OsTAM* mutant, specific forward and reverse primer pairs were used (Table S1).

Whole-plasmid mutagenesis of the pET28a plasmid containing wild-type *OsTAM* cDNA (*OsTAM*-pET) was performed by polymerase chain reaction (PCR) using the Phusion HF DNA polymerase (New England Biolabs, Ipswich, MA). The thermocycling conditions had an initial denaturation step at 95 °C for 5 min, followed by 18 cycles at 95 °C for 30 s, an optimal primer annealing temperature for each primer set for 1 min, and 68 °C for 8.5 min. The PCR was completed with a final elongation step of 68 °C for 5 min. The *OsTAM*-pET template plasmid remaining after each thermocycling reaction was digested with DpnI (New England Biolabs) at 37 °C for 2 h.

The resultant pN446K-*OsTAM* plasmid was used as the template in another round of whole-plasmid PCR with the Y125C oligonucleotide primer set to make the pY125C/N446K-*OsTAM* double mutant. Likewise, other multiple mutants were made using the proper precursor mutant

plasmid (Table S1 and Table S2). Each resulting plasmid was used to transform a separate *DH5 α Escherichia coli* strain (Invitrogen, Thermo Life Sciences, Grand Island, NY). The resulting colonies were inoculated into 5-mL starter cultures and grown for plasmid replication, isolation, and purification (Wizard Plus SV Minipreps DNA Purification System, Promega, Fitchburg, WI). The resultant plasmid DNA was sequenced at the Michigan State University Research Technology Support Facility to verify the *OsTAM* point mutations.

2.3.3 Subcloning, Expression, and Purification of Mutant *OsTAM*.

Plasmids containing *OsTAM* mutant cDNA (Table S3) were used to transform *E. coli* BL21(DE3) cells. Cells were grown in 3 L of Luria-Bertani (LB) medium supplemented with kanamycin (50 μ g/ mL). Overexpression of the *OsTAM* mutant DNA was induced by addition of isopropyl β -D-thiogalactopyranoside (IPTG) (250 μ M), and the cells were grown at 18 °C for 18 h. The cells were harvested by centrifugation, and the resulting pellet was resuspended in lysis buffer [50 mM sodium phosphate containing 300 mM NaCl, 10 mM imidazole, and 5% (v/v) glycerol (pH 8.0)]. The cells were lysed by sonication (Misonix Sonicator, Farmingdale, NY), and the cellular debris was removed by centrifugation. The crude lysate was added to a nickel-nitrilotriacetic acid affinity chromatography column (Qiagen, Valencia, CA) that was pre-equilibrated with wash buffer [50 mM sodium phosphate containing 300 mM NaCl, 10 mM imidazole, and 5% (v/v) glycerol (pH 8.0)]. Each *OsTAM* mutant was expressed with a His₆ tag and purified according to the protocol described by the manufacturer. *OsTAM* mutant enzymes (~76 kDa) eluted in the 250 mM imidazole fraction, which was concentrated, and buffer exchanged against assay buffer [50 mM sodium phosphate containing 5% (v/v) glycerol (pH 8.0)], using a Centriprep centrifugal filter (30K molecular weight cutoff, Millipore). The protein mixtures containing *OsTAM* mutants were subjected to

sodium dodecyl sulfate–polyacrylamide gel electrophoresis and stained with Coomassie Blue *in situ*. The purity (~60%) of each mutant was calculated on a Kodak Gel Logic 100 Imaging System (Figure S2 and Figure S5.). The mutant enzyme concentrations were estimated (corrected for purity) on a NanoDrop spectrophotometer (Thermo Scientific, Wilmington, DE).

2.3.4 Activity of *OsTAM* Mutants.

The activity of each *OsTAM* mutant was tested with α -tyrosine, α -phenylalanine, and analogues of α -phenylalanine variously substituted on the aryl ring at the *ortho*, *meta*, and *para* positions. Wild-type and mutant enzymes (0.2 mg each) were incubated separately with each substituted phenylalanine substrate (2 mM) in 0.25 mL of assay buffer, run in triplicate at 29 °C for 5 h. On the basis of the steady-state range from 3 to ~8 h for AL activity (see Figure S6. and Figure S7. for examples), the enzyme reactions were terminated at 5 h within the steady state. At the end of the reaction, the product mixture containing amino acids and acrylates was then treated with pyridine (2×0.6 mmol) and ethyl chloroformate (2×0.5 mmol) and ethanol in one pot and stirred for 5 min. For assays incubated with α -tyrosine, the resulting 4'-*O*,2-*N*- and 4'-*O*,3-*N*-di(ethoxycarbonyl) ethyl ester derivatives of α - and β -tyrosine, respectively, and the 4'-*O*-ethoxycarbonyl ethyl ester derivative of *p*-coumarate were extracted into diethyl ether (3×1 mL). Likewise, when substituted α -phenylalanines were the substrates, the resulting 2-*N*- and 3-*N*-di(ethoxycarbonyl) ethyl ester derivatives of the α - and β -amino acid isomers and the ethyl ester derivatives of the corresponding ring-substituted cinnamates were extracted into diethyl ether. The organic layer was separated, the solvent was removed under a stream of nitrogen, and the resultant residue was resuspended in 100 μ L of a 3:1 ethyl acetate/ethanol mixture (v/v). The derivatives were analyzed by gas chromatography–mass spectrometry (GC/EI–MS) with a limit of detection at ~55 pM (see Figure S8. - Figure S19 for representative spectra). The derivatized

biosynthetic products had retention times and fragment ion abundances identical to those of authentic standards derivatized in the same way (see the Supporting Information).

2.3.5 Kinetic Parameters of *Os*TAM Mutants with α -Phenylalanine Analogues.

Wild-type *Os*TAM and mutants (0.20 mg) were incubated in assay buffer (3 mL) containing a (2*S*)- α -phenylalanine analogue (3 M) to establish linearity over time at a fixed protein concentration at 29 °C (see Figure S6. and Figure S7. for representative examples). Aliquots (250 μ L) were withdrawn from each at 1-h intervals over 12 h. The products were derivatized and quantified, and steady-state conditions were determined. To calculate the kinetic constants, the (2*S*)- α -phenylalanine analogue concentration was varied (0.1, 0.2, 0.5, 1, 2, and 3 mM) in separate assays under steady-state conditions run for ~3 h in triplicate. Kinetic samples at 0.05 and 0.4 mM were added for *p*-Cl- and *p*-F-phenylalanine to help shape the Michaelis–Menten nonlinear regression fit for wild-type *Os*TAM. The resultant cinnamate analogue products were derivatized and quantified as described in the previous section. Kinetic parameters (k_{cat} and K_M , used to approximate K_d) were determined from Michaelis–Menten plots (Figure S20.- Figure S35), using OriginPro 9.0 for the curve fitting.

2.3.6 Homology Modeling of *Os*TAM and Its Mutant Cognates.

Homology models of *Os*TAM and its mutants were created using the Swiss-Model Server (ExPASy) and UCSF Chimera 1.12.¹⁴ For example, the amino acid sequence of *Os*TAM was mapped onto the backbone of the *Tc*PAM homodimer (PDB entry 3NZ4). The output text file was then appended to include the contents of CRYST1 from 3NZ4 (unit cell parameters, space group, and Z value), allowing the homotetramer of the *Os*TAM model to be created within UCSF Chimera 1.12. This homotetrameric model of *Os*TAM was then aligned with the homotetramers of *Tc*PAM and *Pc*PAL (PDB entry 1W27) to adopt the most probable and useful rotamers for each active site residue.

2.4 Results and Discussion

2.4.1 Determining Effects of Active Site Mutants on Substrate Selectivity and Activity.

To guide the change in substrate preference of *Os*TAM, a systematic strategy from earlier studies in which the MIO-dependent enzyme specificity was interchanged from tyrosine to phenylalanine and vice versa was followed. As an example, the substrate specificity of an MIO-tyrosine ammonia lyase *Rs*TAL from *Rhodobacter sphaeroides* was altered by a H89F mutation in active site. This removed the H-bonding interaction between the active site H89 and substrate,⁶ and the substrate specificity changed from tyrosine to phenylalanine without changing the intrinsic AL activity. A systematic strategy emerged to interchange MIO-dependent enzyme specificity from tyrosine to phenylalanine and vice versa. An analogous mutation, based on the *Rs*TAL study, was also done recently with the plant aminomutase *Tc*PAM.⁷ The *Rs*TAL preference for tyrosine depended on a histidine hydrogen-binding contact with *p*-OH of the

substrate. A reciprocal mutation was done with *TcPAM*, where the active site C107H mutation stimulated TAM activity with a preference for tyrosine without altering the mutase function.

In a recent study, we used a strategy like those described earlier to change the substrate specificity of *OsTAM* from tyrosine to phenylalanine.³ A model of *OsTAM* was built from the crystal structure (PDB 3NZ4) of the plant-derived *TcPAM*. *OsTAM* and *TcPAM* differ by only two residues (Y125 and N446 of *OsTAM* compared with C107 and K427 of *TcPAM*) in their active sites, and the enantioselectivities of their reaction products are almost identical.³ The active site of *OsTAM* residues resembles that of *TcPAM* more than that of other TAMs. Even more interesting, unlike bacterial TAMs, *OsTAM* does not contain signature histidine and serine residues in the aryl ring-binding region of the active site.

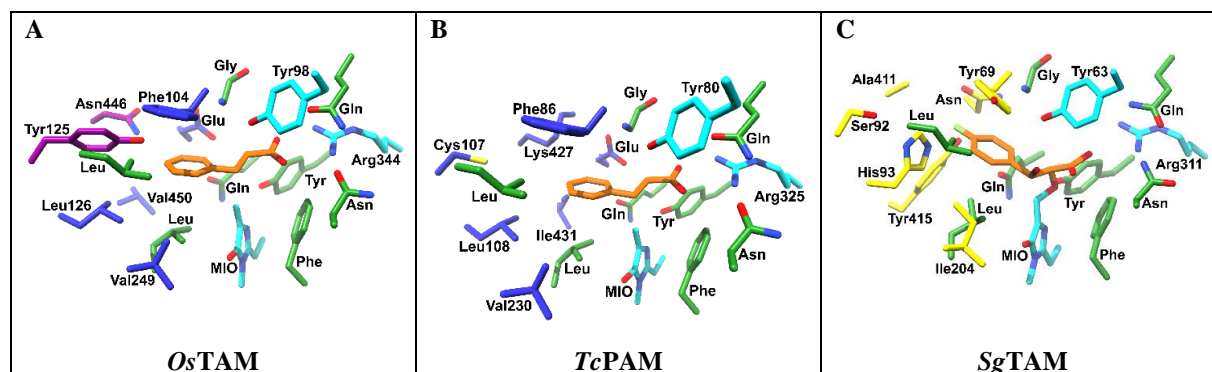


Figure 2.1. Comparison of the residues forming the aryl binding pocket for the substrate, catalytic tyrosine, the arginine for carboxylate binding in the active sites and MIO (cyan) of A) *OsTAM* with a cinnamate intermediate (orange) modeled on B) *TcPAM* (PDB: 3NZ4) and *PcPAL* (PDB: 1W27) (not shown), and C) *SgTAM* (PDB: 2RJR). Common residues for all three enzymes were shown in green color.

Therefore, we hypothesized that *OsTAM* could be converted into a functional PAM through straightforward active site mutations. These *OsTAM* mutants (Y125C, N446K and Y125C/N446K) were reacted with different substituted α -phenylalanines, the products were derivatized and analyzed by GC-MS. Two active site mutations (Y125C/N446K) of the *OsTAM*

made it match the first-tier active site residues of *Tc*PAM. The *Os*TAM double mutant was more selective for phenylalanine.

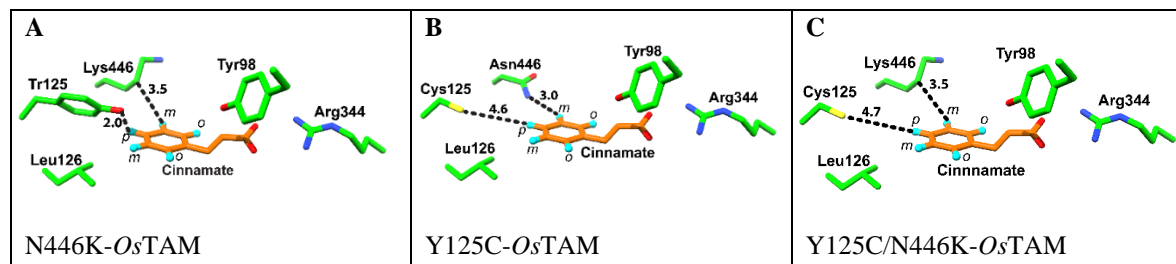


Figure 2.2. *Os*TAM active site mutants A) N446K-*Os*TAM, B) Y125C-*Os*TAM, and C) Y125C/N446K-*Os*TAM modeled on the *Tc*PAM (PDB: 3NZ4) and *Pc*PAL (PDB: 1W27) with cinnamate docked as per PDB: 3NZ4 and PDB: 1W27. Heteroatoms are colored red for oxygen, blue for nitrogen. Numbers are distances in Angstroms. On aryl ring, *o* designates *ortho*-positions, *m* designates *meta*-positions, and *p* designates *para*-position.

The *Os*TAM active site residues resemble (Figure 2.1A) those of the MIO phenylalanine aminomutase *Tc*PAM (Figure 2.1B) more than those of other TAMs.³ Even more interesting, unlike bacterial TAMs, *Os*TAM does not contain signature histidine and serine residues in the aryl binding region of the active site, such as in *Sg*TAM (Figure 2.1C). Instead, *Os*TAM uses polar Y125 and N446 residues to bind the phenol moiety of its tyrosine substrate. First-tier residues in the active sites of Y125C/N446K-*Os*TAM and *Tc*PAM were identical. Y125C/N446K-*Os*TAM catalyzed the cinnamate intermediate as the major product. This was unexpected because a precedent study described how modest changes (C107H) to the active site of the *Tc*PAM (see Figure 2.2), excluding catalytic residues, changed the substrate specificity from phenylalanine to tyrosine but did not alter the aminomutase function.⁷

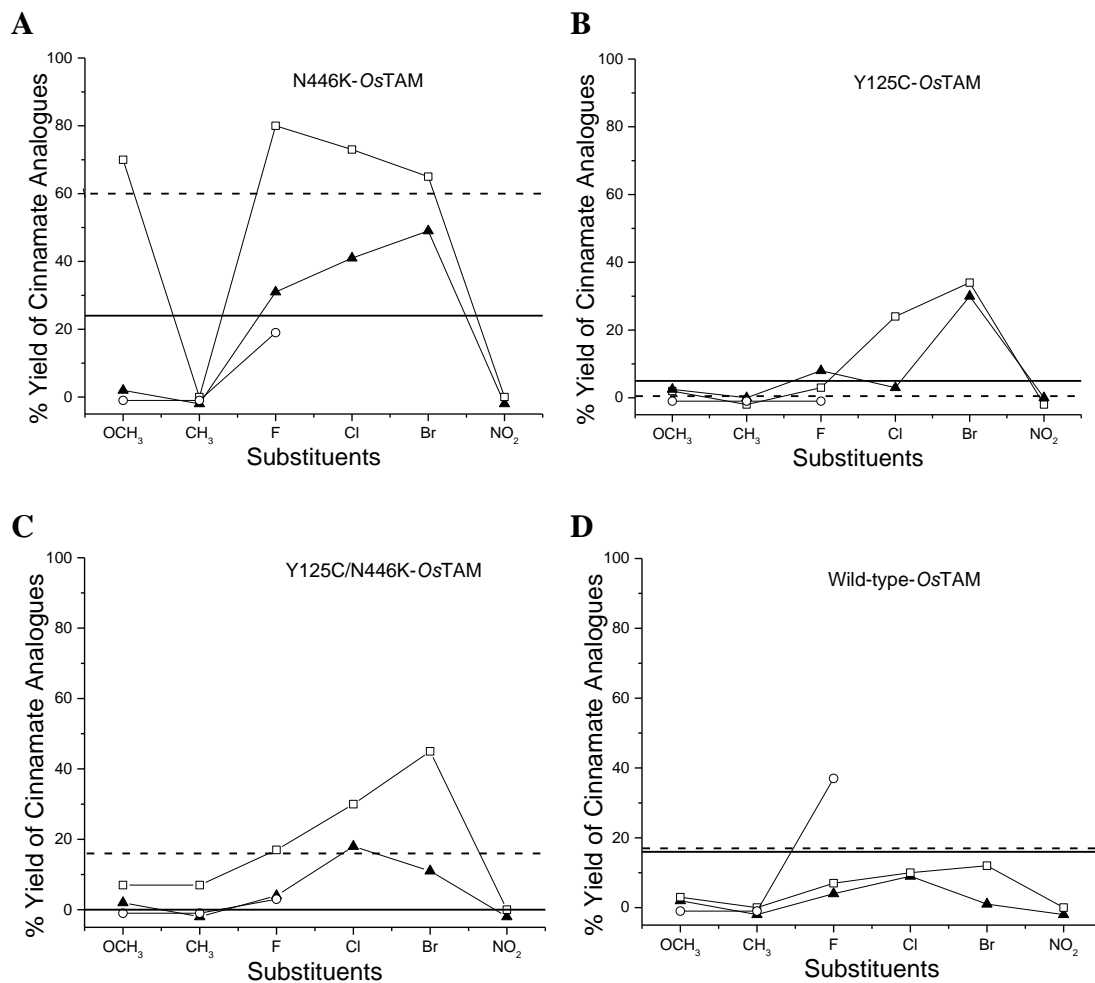


Figure 2.3. The percent yield of *trans*-cinnamate analogs made biocatalytically from A) N446K-*OsTAM*, B) Y125C-*OsTAM*, C) Y125C/N446K-*OsTAM* active site mutants, and D) wild-type *OsTAM* incubated with *p*-(□), *m*-(▲), and *o*-(○)-substituted α -phenylalanines. The dashed line shows the percent yield of cinnamic acid from phenylalanine, and the solid line shows the percent yield of coumaric acid from tyrosine. Standard error = $\pm 5\%$.

In this study, Y125C/N446K-*OsTAM* and single mutant Y125C-*OsTAM* or N446K-*OsTAM* functioned as ALs, turning over several substituted phenylalanines with higher conversion than wild-type *OsTAM* did (Figure 2.3). It is worth noting that the aryl ring binding pocket in the active site of N446K-*OsTAM* and that of *PcPAL*⁸ are isosteric,

differing by one residue [Y125 in N446K-*O*sTAM and F137 in *Pc*PAL (PDB entry 1W27)]. It is unclear how the sterically similar active sites of N446K-*O*sTAM and *Pc*PAL promote their AL activities. N446K-*O*sTAM retained slightly higher AM activity with tyrosine (~9% conversion to β -tyrosine), while Y125C-*O*sTAM and Y125C/N446K-*O*sTAM catalyzed phenylalanine and its substituted analogues to their β -amino acids at 3% maximum converted yield (Figure S44). However, each of these mutants unexpectedly catalyzed cinnamate as the major product.³ The low AM activity of Y125C/N446K-*O*sTAM was surprising, because the first-tier residues in the active sites of Y125C/ N446K-*O*sTAM and *Tc*PAM are identical.

2.4.1.1 N446K-*O*sTAM mutant *p*-Substituted Substrates.

Single mutant N446K-*O*sTAM turned over phenylalanine, halogen-, *p*-OCH₃-, and *p*-OH-phenylalanines (the latter is the natural substrate tyrosine) at >50% conversion to their acrylates, converting the *p*-F substrate the most (80%) (Figure 2.3A) Phenylalanines with the smaller *p*-H-substituted (60%) and the larger *p*-F- and *p*-Cl-substituted substrates were turned over similarly (Figure 2.3A). These conversion yields are much higher than those for wild-type *O*sTAM, which converted each para-substituted substrate at <20% (Figure 2.3D). N446K-*O*sTAM turned over the *p*-halogen series (F, Cl, and Br) in a manner inversely proportional to size, with the larger Br substrate turned over slower. This observation was paradoxical because a structural model of N446K-*O*sTAM, based on a crystal structure of *Tc*PAM, has a steric Y125 residue near the *para* carbon of the substrate. Based on the catalytic efficiency (k_{cat}/K_M) of N446K-*O*sTAM, *p*-Br was having higher efficiency than *p*-Cl and *p*-F substrates which is reciprocal with observed conversion yields.

However, the K_M values of the enzyme for the halogenated and phenylalanine substrates were the same order of magnitude (Table 2.1); thus, the difference in the turnover of N446K-

*Os*TAM for phenylalanine and the halogenated substrates was largely influenced by electronics, according to Hammett σ_{para} constants,⁹ and less by steric.

The electron donating property of *p*-OCH₃ did not slow the elimination reaction more than when phenylalanine was the substrate, as postulated in another study.¹⁰ Therefore, we propose that the rate determining step of the elimination reaction changed for the *p*-OCH₃ substrate from β -hydrogen abstraction (through a carbanion transition state) to NH₂-MIO elimination (through a carbocation transition state) (Figure 1.4). The electron releasing, inductive property of the OCH₃ can theoretically stabilize the latter carbocationic transition, which is supported by electronic substituent effects on the mechanism of an MIO-dependent AM described in an earlier study.¹¹

We also anticipated that the large steric occupancy of the *p*-OCH₃ substrate would discourage turnover, but the OCH₃ group can rotate its CH₃ away from Y125 (Table S4) and reduce the extent of steric clashing. This rotational freedom of the OCH₃ may account for its robust conversion (~70%) that was similar to that of phenylalanine and halogenated substrates. In addition, the van der Waals surface of Y125 in N446K-*Os*TAM overlaps with the steric volumes of the *p*-NO₂ and *p*-CH₃ substituents (Table S4). These observations can purportedly explain why substrates with a *p*-NO₂ or *p*-CH₃ were turned over below the detection limit of the analysis.

2.4.1.2 *meta*- and *ortho*-Substituted Substrates.

A model of N446K-*Os*TAM from a crystal structure of *Tc*PAM¹² places N446 (Figure 2.2A) in a position identical to that of K427 in *Tc*PAM (Figure 2.1B). The ϵ -NH₂ of K427 is oriented outside the active site, while the hydrophobic β -, δ -, and γ -methylene carbons of its side chain border the active site cavity (Figure 2.2A). N446K-*Os*TAM provided steric relief for the *meta* substituted substrates (Figure 2.3A), but the sensitivity to electronic effects was unmasked.

N446K-*O*sTAM turned over *m*-F (31%; $\sigma_{meta} = 0.34$), *m*-Cl (41%; $\sigma_{meta} = 0.37$), and *m*-Br (49%; $\sigma_{meta} = 0.39$) substrates proportionally with the Hammett σ_{meta} constants.¹³

The *m*-OCH₃ substrate was turned over at 2% ($\sigma_{meta} = 0.12$), supporting the finding that electron-withdrawing meta substituents hasten and electron-donating meta substituents discourage the MIO-AL activity of N446K-*O*sTAM.¹⁰ N446K-*O*sTAM turned over the meta-substituted substrates slower than the para isomers. We hypothesize that a stronger steric interaction between Y125 and the para substituents might help align the substrate into a favorable catalytic orientation.

Only the *o*-F-, *o*-OCH₃-, and *o*-CH₃-phenylalanine isomers were on hand for testing. Just like with meta-substituted substrates, N446K-*O*sTAM turned over *o*-F-phenylalanine (19%) to its cinnamate significantly better than it turned over the *o*-OCH₃- and -CH₃-substituted phenylalanines (Figure 2.3A). Substrates with a sizable *ortho* substituent have a torsional barrier between the substituent and the propyl side chain of phenylalanine that could disrupt productive catalytic conformations within the enzyme, the substrate, or both.¹¹

Table 2.1. Kinetic Parameters of *OsTAM* Wild-type and Mutant Enzymes for α -Phenylalanine and Its Analogs.

<i>OsTAM</i> type	<i>p</i> -Br			<i>p</i> -Cl			<i>p</i> -F			<i>p</i> -H (no substituent)		
	k_{cat} ($10^{-3} s^{-1}$)	K_M (mM)	k_{cat}/K_M	k_{cat} ($10^{-3} s^{-1}$)	K_M (mM)	k_{cat}/K_M	k_{cat} ($10^{-3} s^{-1}$)	K_M (mM)	k_{cat}/K_M	k_{cat} ($10^{-3} s^{-1}$)	K_M (mM)	k_{cat}/K_M
N446K	48 ± 8	0.4 ± 0.1	120	40 ± 2	0.4 ± 0.03	100	40 ± 8	0.4 ± 0.1	100	33 ± 3	0.5 ± 0.1	66
Y125C	21 ± 8	0.4 ± 0.1	52	17 ± 2	0.4 ± 0.1	42	12 ± 3	0.8 ± 0.2	15	6 ± 1	0.8 ± 0.2	8
Y125C/ N446K	18 ± 1	0.3 ± 0.03	60	16 ± 2	0.5 ± 0.1	32	16 ± 2	0.4 ± 0.1	40	11 ± 3	0.5 ± 0.1	22
Wild type	14 ± 2	0.7 ± 0.2	20	12 ± 2	0.7 ± 0.2	17	10 ± 1	0.7 ± 0.1	14	13 ± 2	(0.7 ± 0.1)	19

2.4.1.3 Y125C-*OsTAM* Mutant. Substituted Substrates.

The single mutant Y125C-*OsTAM* generally turned over the *p*-halogen substrates to their cinnamate analogues faster than the other substrates tested in this study. Y125C-*OsTAM* conversion of *p*-F (3%; $\sigma_{para} = 0.06$), *p*-Cl (25%; $\sigma_{para} = 0.23$), and *p*-Br (34%; $\sigma_{para} = 0.23$) correlated with increasing Hammett σ_{para} constants (Figure 2.3B). This supported the finding that electron-withdrawing substituents accelerate the MIO-AL reactions. In addition, the Y125C mutation likely reduced the degree of steric strain between the para substituents and the active site (Figure 2.2C)

Docking the *p*-Br-substituted and phenylalanine substrates into the Y125C-*OsTAM* active site shows that the steric relief can better accommodate the bromo group, while phenylalanine likely binds less tight (Table S5). The effects of this steric relief were supported by the slightly lower K_M (0.4 mM) of Y125C-*OsTAM* for the larger *p*-Br phenylalanine calculated in this study compared with the K_M (0.8 mM) for the less steric phenylalanine (Table 2.1). Also, Y125C-

-OsTAM turned over *para*-substituted substrates (Figure 2.3B) slower than N446K-OsTAM did (Figure 2.3A). These data suggest that the steric compression between Y125 of N446K-OsTAM and the *para*-substituents might lock the substrate into an orientation favorable for catalysis.

Y125C-OsTAM turned over the *meta*-substituted substrates with an electronegativity trend similar to that of the *para*-substituted substrates (Figure 2.3B). It is not clear, however, why the *m*-Cl substrate was turned over slower than the *m*-F and *m*-Br substrates (Figure 2.3B). In addition, Y125C-OsTAM did not turn over the three *ortho*-substituted phenylalanines. This contrasts with the 20% conversion of *o*-F-phenylalanine to *o*-F cinnamate catalyzed by N446K-OsTAM. The steric bulk of Y125 in N446K-OsTAM may help position the aryl ring of the substrate with the smaller *o*-F substituent in a proper catalytic conformation, which is lost in the Y125C-OsTAM mutant (Figure 2.2B).

2.4.1.4 Y125C/N446K-OsTAM Mutant.

The trends in converted yield of the *para*-, *meta*-, and *ortho*-substituted substrates by Y125C/N446K-OsTAM mutant shares features of those for the single mutants N446K-OsTAM and Y125C-OsTAM (Figure 2.3C). For example, the conversion of the *para*-substituted substrates catalyzed by the double mutant (Figure 2.3C) and Y125C-OsTAM is similar (Figure 2.3B) at <10% for the *p*-OCH₃ and *p*-CH₃ substrates, and ramping from 17% for the *p*-fluoro to 45% for the *p*-bromo substrates.

We did notice slightly higher activity of Y125C/N446K-OsTAM versus that of Y125C-OsTAM for the *para*-substituted substrates, suggesting that the N446K mutation somehow helps enhance its catalysis (Figure 2.3).

We noted earlier that the Y125C-*Os*TAM created steric relief near the *para*-carbon, but remained inactive with the *p*-CH₃ substrate. However, the favorable N446K mutation enabled Y125C/N446K-*Os*TAM to turnover the *p*-CH₃ substrate at ~10% conversion (Figure 2.3C). The benefit attributed to the N446K mutation, by an unknown process, is also evident in the significantly better turnover of phenylalanine by Y125C/N446K-*Os*TAM (16% conversion) (Figure 2.3C) than by Y125C-*Os*TAM (~3% conversion) (Figure 2.3B and Table 2.1).

Y125C/N446K-*Os*TAM turned over the *m*-OCH₃ (2%) and *m*-CH₃ (0%) substrates to their acrylates with almost the same yield (Figure 2.3C) as both single mutants (Figure 2.3A,B) and wild-type *Os*TAM (Figure 2.3D). The double mutant turned over the *m*-halogen substrate series [*m*-Cl product (18%) > *m*-F (4%) and *m*-Br products (11%)] with a trend parallel to that for wild-type *Os*TAM (Figure 2.1C). In contrast, the amount of *m*-Cl product quantified (~3% converted yield) after catalysis by the Y125C-*Os*TAM cognate catalysis was lower than those of the *m*-F (8% converted yield) and *m*-Br (30% converted yield) acrylate products. Y125C-*Os*TAM and Y125C/N446K-*Os*TAM seem to effect the turnover of the *m*-Cl and *m*-Br substrates without regard to steric, and there was no linear correlation between the Hammett σ_{meta} constants⁹ and electronic effects of the substituents (Figure 2.3). It is therefore unclear how the common Y125C mutation for Y125C-*Os*TAM and Y125C/ N446K-*Os*TAM, and the N446K exchange in the latter, affect the substrate preference for the *m*-Cl-and *m*-Br substituents.

2.5 Conclusions

This mutation study improved our understanding of the factors that control the substrate specificity of an MIO-dependent AM. Changing the substrate specificity of *Os*TAM to that of a PAM in principle releases the dependence on needing a *p*-OH group on the substrate and changes the substrate scope to make an extended array of β -amino acids of potential pharmaceutical interest. We approached this goal by introducing two mutations into the active site of *Os*TAM so that it matched those in the active site of *Tc*PAM. The substrate preference of *Os*TAM changed from tyrosine to phenylalanine, but to our surprise, the AM activity was lost nearly completely, and the AL activity became predominant. Phenylalanine lacks a substituent on the aryl ring that can act as a binding contact that aligns it for catalysis in mutants. We proposed that the missing electronics or steric on the aryl ring of the phenylalanine substrate, compared to the steric, H-bonding hydroxyl of the natural tyrosine substrate, caused the unexpected AL reactivity. We tested different regioisomers of substituted phenylalanine substrates that had a steric “bump” on the substrates to substitute for the hydroxyl group of tyrosine. The steric and varying electronic effects of the substituents did not help *Os*TAM recover its AM activity with any phenylalanine analogue used here. Minor active site mutations of *Os*TAM tipped the delicate balance of the AM to that of an ancestral cognate MIO-AL. With this study, we also focused our concerns towards finding the differences that control PAL and PAM activity which is explained in next chapter.

REFERENCES

REFERENCES

1. Walter, T.; King, Z.; Walker, K. D., A Tyrosine Aminomutase from Rice (*Oryza sativa*) Isomerizes (*S*)- α -to (*R*)- β -tyrosine with Unique High Enantioselectivity and Retention of Configuration. *Biochemistry* **2015**, *55* (1), 1-4.
2. Mutatu, W.; Klettke, K. L.; Foster, C.; Walker, K. D., Unusual Mechanism for an Aminomutase Rearrangement: Retention of Configuration at the Migration Termini. *Biochemistry* **2007**, *46* (34), 9785-9794.
3. Walter, T.; Wijewardena, D.; Walker, K. D., Mutation of Aryl Binding Pocket Residues Results in an Unexpected Activity Switch in an *Oryza sativa* Tyrosine Aminomutase. *Biochemistry* **2016**, *55* (25), 3497-3503.
4. Attanayake, G.; Walter, T.; Walker, K. D., Understanding Which Residues of the Active Site and Loop Structure of a Tyrosine Aminomutase Define its Mutase and Lyase Activities. *Biochemistry* **2018**, *57* (25), 3503-3514.
5. Kudo, F.; Miyanaga, A.; Eguchi, T., Biosynthesis of Natural Products Containing β -Amino Acids. *Natural product reports* **2014**, *31* (8), 1056-1073.
6. Louie, G. V.; Bowman, M. E.; Moffitt, M. C.; Baiga, T. J.; Moore, B. S.; Noel, J. P., Structural Determinants and Modulation of Substrate Specificity in Phenylalanine-tyrosine Ammonia-lyases. *Chemistry & biology* **2006**, *13* (12), 1327-1338.
7. Wu, B.; Szymański, W.; Wijma, H. J.; Crismaru, C. G.; de Wildeman, S.; Poelarends, G. J.; Feringa, B. L.; Janssen, D. B., Engineering of an Enantioselective Tyrosine Aminomutase by Mutation of a single active site residue in phenylalanine aminomutase. *Chemical Communications* **2010**, *46* (43), 8157-8159.
8. Dreben, A.; Hilberath, T.; Mackfeld, U.; Billmeier, A.; Rudat, J.; Pohl, M., Phenylalanine Ammonia Lyase from *Arabidopsis thaliana* (AtPAL2): A Potent MIO-Enzyme for the Synthesis of Non-canonical Aromatic α -amino Acids: Part I: Comparative Characterization to the Enzymes from *Petroselinum crispum* (PcPAL1) and *Rhodospiridium toruloides* (RtPAL). *Journal of biotechnology* **2017**, *258*, 148-157.
9. Hansch, C.; Leo, A., *Substituent Constants for Correlation Analysis in Chemistry and Biology*. Wiley: 1979.
10. Bartsch, S.; Bornscheuer, U. T., Mutational Analysis of Phenylalanine Ammonia Lyase to Improve Reactions Rates for Various Substrates. *Protein Engineering, Design & Selection* **2010**, *23* (12), 929-933.
11. Ratnayake, N. D.; Liu, N.; Kuhn, L. A.; Walker, K. D., Ring-Substituted α -Arylalanines for Probing Substituent Effects on the Isomerization Reaction Catalyzed by an Aminomutase. *ACS Catalysis* **2014**, *4* (9), 3077-3090.

12. Feng, L.; Wanninayake, U.; Strom, S.; Geiger, J.; Walker, K. D., Mechanistic, Mutational, and Structural Evaluation of a *Taxus* Phenylalanine Aminomutase. *Biochemistry* **2011**, *50* (14), 2919-2930.
13. Hansch, C.; Leo, A.; Taft, R., A survey of Hammett Substituent Constants and Resonance and Field Parameters. *Chemical Reviews* **1991**, *91* (2), 165-195.
14. Pettersen, E. F.; Goddard, T. D.; Huang, C. C.; Couch, G. S.; Greenblatt, D. M.; Meng, E. C.; Ferrin, T. E., UCSF Chimera—a Visualization System for Exploratory Research and Analysis. *Journal of computational chemistry* **2004**, *25* (13), 1605-1612.

Chapter 3 . Dissecting the Role of the Inner Loop Caping the Active Site.

Reprinted (adapted) with permission from (Attanayake, G. K.; Walter, T.; Walker, K. D., Understanding which residues of the active site and loop structure of a tyrosine aminomutase define its mutase and lyase activities. *Biochemistry*. 2018, 57 (25), 3503-3514.) Copyright (2018) American Chemical Society.

3.1 Introduction

Another active site feature of MIO-enzymes is a flexible inner-loop region that was targeted for mutation in *TcPAM* in a previous study to exchange the AM activity with that of an AL.¹ The inner loop of *TcPAM* purportedly caps the active site cavity and has a catalytic tyrosine that removes the β -hydrogen from the substrate during the reaction. The earlier report suggested that a flexible inner-loop structure, more interactive with bulk water, would less effectively seal the active site and decrease the residence time of the acrylate intermediate.¹ The rapid release of the acrylate would discourage NH_2 -rebound from the NH_2 -MIO adduct to produce the β -amino acid. An earlier study tested this hypothesis by changing inner-loop residues of *TcPAM* from hydrophobic to the hydrophilic residues positioned analogously in the ammonia lyase *PcPAL*. The results showed that by adding the polar residues *TcPAM* behaved more like *PcPAL*.

Here, we hypothesized that the altered electronics (N446K) and weakened steric interactions (Y125C) between the active site of *OsTAM* and the aryl ring of the substrate changed the mutase reaction chemistry to that of a lyase. We tested different α -phenylalanines with substituents of varying electronic properties and steric demand to complement the N556K and Y125C mutations in the *OsTAM* sequence and determine if the isomerization chemistry of *OsTAM* was restored. Further, the *OsTAM* inner loop has higher sequence identity (65%) with the ammonia lyase *PcPAL* inner-loop structure than that of the aminomutase *TcPAM* (34% identity). Our approach contrasted that described in an earlier report that looked to convert *TcPAM* into a *TcPAL*.¹ Here,

we made the inner-loop structure of *Os*TAM chemically analogous to the presumed "closed" loop of the homologous plant *Tc*PAM that uses more hydrophobic residues. We hypothesized that the residence time of the acrylate intermediate would increase and enable *Os*TAM mutants to rebound NH₂ more efficiently to the acrylate intermediate to produce more β -amino acid.

3.2 Experimental

3.2.1 Chemicals and Reagents.

Chemicals. (3*R*)- β -Tyrosine and (3*R*)- β -phenylalanine were obtained from Peptech (Burlington, MA). All other chemicals and reagents were obtained from Sigma-Aldrich (St. Louis, MO) and used without further purification unless noted otherwise.

3.2.2 Instrumentation.

GC/EI-MS analysis was performed on an Agilent 6890N gas chromatograph equipped with a capillary GC column (30 m \times 0.25 mm \times 0.25 μ M; HP-5MS; J & W Scientific) with He as the carrier gas (flow rate, 1 mL/min). The injector port (at 250 °C) was set to splitless injection mode. A 1- μ L aliquot of each sample was injected using an Agilent 7683 auto-sampler (Agilent, Atlanta, GA). The column temperature was increased from 200 – 220 °C at 8 °C/min with a 13 min hold, then increased by 50 °C/min to 250 °C, and returned to 200 °C over 5 min, with a 5 min hold for tyrosine and *para*-coumarate derivatives detection; the column temperature was increased from 50 – 110 °C at 30 °C/min then increased by 10 °C/min to 250 °C, and returned to 50 °C over 5 min, with a 5 min hold for phenylalanine and cinnamate derivatives detection. The gas chromatograph was coupled to a mass selective detector (Agilent, 5973 inert) operated in electron impact mode (70 eV ionization voltage). All spectra were recorded in the mass range of 50 – 400 *m/z* to analyze amino acid and acrylate derivatives.

3.2.3 *OsTAM* Mutations.

Point mutations of the *OsTAM* gene were generated by the QuickChange Multi Site-Directed Mutagenesis Kit (Stratagene) using the buffers, enzymes, and dNTP mix provided. To make each single *OsTAM* mutant, specific forward and reverse primer pairs were used (Table S1).

Whole-plasmid mutagenesis of the pET28a plasmid containing the wild-type *OsTAM* cDNA (*OsTAM*-pET) was done by PCR using the Phusion HF DNA polymerase (New England Biolabs, Ipswich, MA). The thermocycling conditions were an initial denaturation step at 95 °C for 5 min, followed by 18 cycles at 95 °C for 30 s, an optimal primer annealing temperature for each primer set for 1 min, and 68 °C for 8.5 min. The PCR reaction was completed with a final elongation step of 68 °C for 5 min. The *OsTAM*-pET template plasmid remaining after each thermocycling reaction was digested with DpnI (New England Biolabs) at 37 °C for 2 h.

Each resulting plasmid was used to transform a separate DH5 α *E. coli* strain (Invitrogen, Thermo Life Sciences, Grand Island, NY). The resulting colonies were inoculated in 5-mL starter cultures and grown for plasmid replication, isolation, and purification (Wizard Plus SV Minipreps DNA Purification System, Promega, Fitchburg, WI). The resultant plasmid DNA was sequenced at the Michigan State University Research Technology Support Facility to verify the *OsTAM* point mutations.

3.2.4 Subcloning, Expression, and Purification of Mutant *OsTAM*.

Plasmids containing *OsTAM* mutant cDNA (Table S2) were used to transform *E. coli* BL21(DE3) cells. Cells were grown in 3 L of Luria-Bertani (LB) medium supplemented with kanamycin (50 $\mu\text{g}/\text{mL}$). Overexpression of the *OsTAM* mutant DNA was induced by addition of isopropyl β -D-thiogalactopyranoside (IPTG) (250 μM), and the cells were grown at 18 $^{\circ}\text{C}$ for 18 h. The cells were harvested by centrifugation, and the resulting pellet was resuspended in lysis buffer [50 mM sodium phosphate containing 300 mM NaCl, 10 mM imidazole, and 5% (v/v) glycerol (pH 8.0)]. The cells were lysed by sonication (Misonix Sonicator, Farmingdale, NY), and the cellular debris was removed by centrifugation. The crude lysate was added to a nickel-nitrilotriacetic acid affinity chromatography column (Qiagen, Valencia, CA) that was pre-equilibrated with wash buffer [50 mM sodium phosphate containing 300 mM NaCl, 10 mM imidazole, and 5% (v/v) glycerol (pH 8.0)]. Each *OsTAM* mutant was expressed with a His₆-tag and purified according to the protocol described by the manufacturer. *OsTAM* mutant enzymes (~76 kDa) eluted in the 250 mM imidazole fraction, which was concentrated and buffer exchanged against 50 mM sodium phosphate containing 5% (v/v) glycerol (pH 8.0) using a Centriprep centrifugal filter (30K molecular weight cutoff, Millipore). The protein mixtures containing *OsTAM* mutants were run on sodium dodecyl sulfate–polyacrylamide gel electrophoresis and stained with Coomassie Blue *in situ*. The purity (~60%) of each mutant was calculated on a Kodak Gel Logic 100 Imaging System (Figure S2 and Figure S5.). The concentration of each mutant enzyme was estimated (corrected for purity) on a NanoDrop spectrophotometer (Thermo Scientific, Wilmington, DE).

3.2.5 Activity of *Os*TAM Mutants.

The activity of each *Os*TAM mutant was tested with α -tyrosine, α -phenylalanine, and analogs of α -phenylalanine substituted on the aryl ring at the *meta*- and *para*- (*m*- and *p*-, respectively) positions with Br, Cl, F, CH₃, OCH₃, and NO₂, and at the *ortho*- (*o*-) position with F, CH₃, and OCH₃. Each mutant enzyme (0.2 mg of each) was incubated for 5 h with each substrate (2 mM) in assay buffer [50 mM sodium phosphate and 5% (v/v) glycerol (pH 8.0)]. The product mixture containing amino acids and acrylates was treated with pyridine (2 × 0.6 mmol) and ethyl chloroformate (2 × 0.5 mmol) and ethanol in one pot and stirred for 5 min. For assays incubated with α -tyrosine, the resulting 4'-*O*,2-*N*- and 4'-*O*,3-*N*-di(ethoxycarbonyl) ethyl ester derivatives of the α - and β -tyrosine, respectively, and 4'-*O*-ethoxycarbonyl ethyl ester derivative of *p*-coumarate were extracted into diethyl ether (3 × 1 mL). Likewise, when substituted α -phenylalanines were the substrates, the resulting 2-*N*- and 3-*N*-di(ethoxycarbonyl) ethyl ester derivatives of the α - and β -amino acid isomers and the ethyl ester derivatives of the corresponding ring-substituted cinnamates were extracted into diethyl ether. The organic layer was separated, the solvent was removed under a stream of nitrogen, and the resultant residue was resuspended in a 3:1 ethyl acetate/ethanol mixture (v/v). The derivatives were analyzed by gas chromatography-mass spectrometry (GC/EI-MS) with a limit of detection at ~55 pM (see Figure S6. Figure S7. for representative spectra). The derivatized biosynthetic products had retention times and fragment ion abundances identical to those of authentic standards derivatized in the same way (see Supporting Information)

3.2.6 Kinetic Parameters of *Os*TAM Mutants with α -Phenylalanine Analogs.

Wild-type *Os*TAM and mutants (0.20 mg) were incubated in assay buffer (3 mL) containing a (2S)- α -phenylalanine analog to establish linearity with respect to time at a fixed protein concentration at 29 °C. Aliquots (250 μ L) were withdrawn from each at 1 h intervals over 12 h. The products were derivatized and quantified, and steady-state conditions were determined. To calculate the kinetic constants, the (2S)- α -phenylalanine analog concentration was varied (0.1 – 3 mM) in separate assays under steady-state conditions. The resultant cinnamate analog products were derivatized and quantified as described in the previous section. Kinetic parameters (K_M and k_{cat}) were determined from Michaelis–Menten or Lineweaver–Burk plots (Figure S36 - Figure S43), using OriginPro 9.0 for the nonlinear curve fitting.

3.3 Results and Discussion

3.3.1 Inner Loop Alterations of *Os*TAM.

The inner loop region that caps the active site cavity of *Os*TAM was parsed here to understand further what switched its mechanism from a functional MIO-aminomutase to that of an MIO-lyase. An earlier computational study suggested that if the inner loop contained specifically positioned hydrophilic residues, its preference for bulk water would place it in an open conformation. This open loop conformation was proposed to promote lyase activity and stimulate the release of the acrylate intermediate. The earlier report also stated that an inner loop containing more hydrophobic residues would exclude water molecules and close the active site. This would retain the acrylate intermediate, facilitate the NH_2 -rebound, and produce the β -amino acid.² In another earlier investigation,¹ the hydrophobic inner loop residues (A77, I79, C89, and L97) of *Tc*PAM were replaced with a more hydrophilic series (A77T, I79S, C89T, and L97G,

respectively), analogously positioned in an authentic lyase *PcPAL* (Figure 3.1A). The resultant inner loop mutant of *TcPAM* caused the aminomutase to behave more like a lyase.

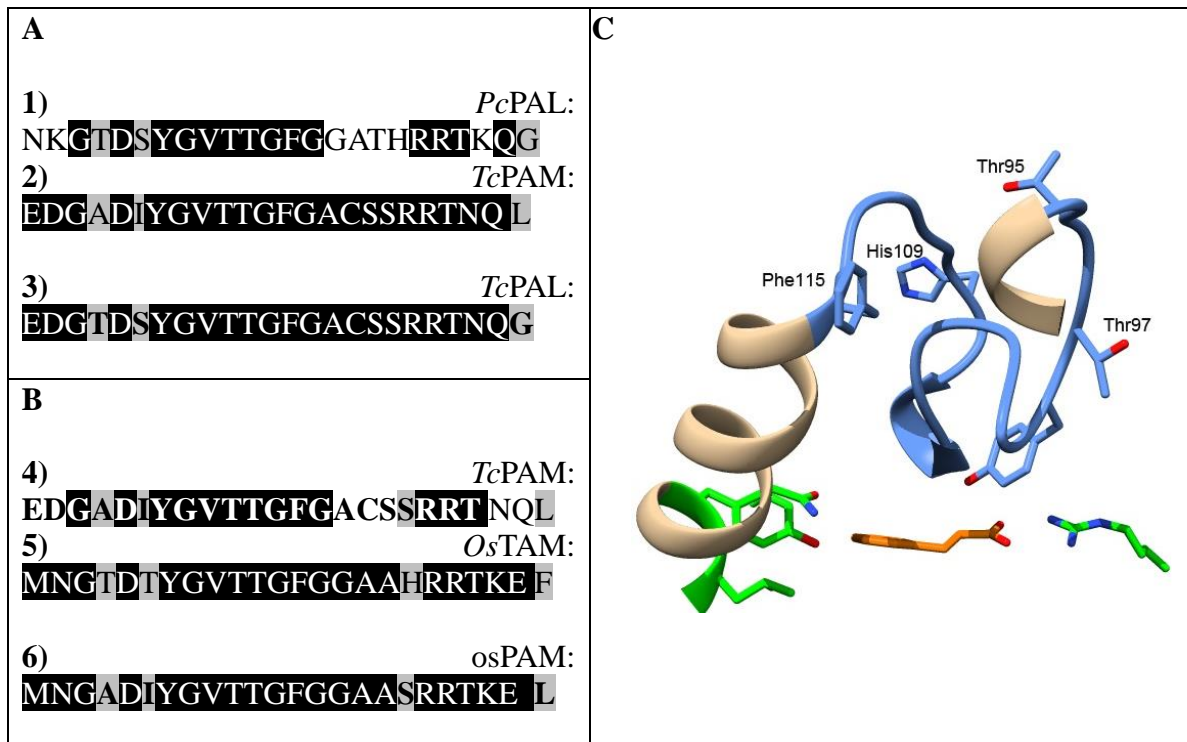


Figure 3.1. A) Alignment of inner loop sequences of 1) ammonia lyase *PcPAL* used to guide mutations in the loop of 2) aminomutase *TcPAM* to convert its function to that of 3) a *TcPAL* lyase. B) Alignment of inner loop sequences of 4) *TcPAM* used to guide mutations in the loop of 5) *OsTAM* to convert its function to that of 6) an aminomutase "*OsPAM*." C) Inner loop structure of *OsTAM* modeled on the *TcPAM* backbone (PDB: 3NZ4) with the cinnamate intermediate (orange) docked in an orientation based on the cocrystallized cinnamate in the *TcPAM* structure. Residues in the aryl ring-binding pocket (green), and inner loop region (blue). Heteroatoms are colored red for oxygen, blue for nitrogen.

A similar strategy of targeting the inner loop structure, used in the earlier studies, was used here with active site mutants of *OsTAM* hopefully to change their predominant lyase activity to aminomutase activity. The hydrophobic inner loop of *TcPAM* was used as the model to mutate *OsTAM* (Figure 3.1B). We first mutated inner loop residues T95, T97, H109, and F115 of *OsTAM* to those of *TcPAM* (T95A, T97I, H109S, and F115L, respectively). We then assessed how these *OsTAM* mutants turned over substrates with different substituents on the aryl ring.

3.3.2 Mutation of Inner-Loop Residues T95 and T97.

Mutations in the loops of wild-type *OsTAM* (T95A-*OsTAM*, T97I-*OsTAM*, and T95A/T97I-*OsTAM*) and Y125C/N446K-*OsTAM* (Y125C/N446K/T95A-*OsTAM*, Y125C/N446K/T95I-*OsTAM*, and Y125C/N446K/T95A/T97I-*OsTAM*) were made, and the enzymes were incubated with substituted α -phenylalanines. Assay products were derivatized and analyzed by GC-MS.

T95A-*OsTAM* and T97I-*OsTAM* (Figure 3.2A and B) still worked principally as lyases, but their turnover was dramatically diminished for each substrate (only slight turnover of the *p*-Cl and *p*-Br substrates was seen at $\lesssim 3\%$). These turnover rates for most halogenated substrates and phenylalanine to their cinnamates were lower than the rates ($\sim 5\% - 10\%$ conversion) of wild-type *OsTAM* (Figure 3.2D). It was interesting to observe that the T95A and T97I mutants converted tyrosine to coumarate at $\sim 20\%$ and $\sim 30\%$ conversion (Figure 3.2A and B) and to β -tyrosine at $\sim 25\%$ and $\sim 38\%$ conversion (Figures S38E and S38F), respectively. The corresponding mutase:lyase product ratios for both mutants was $\sim 1.3:1$ (coumarate: β -tyrosine), which was lower than the 3:1 ratio catalyzed by wild-type *OsTAM*.³ These data show that the T95A and T97I mutations affect the AM activity of *OsTAM*.

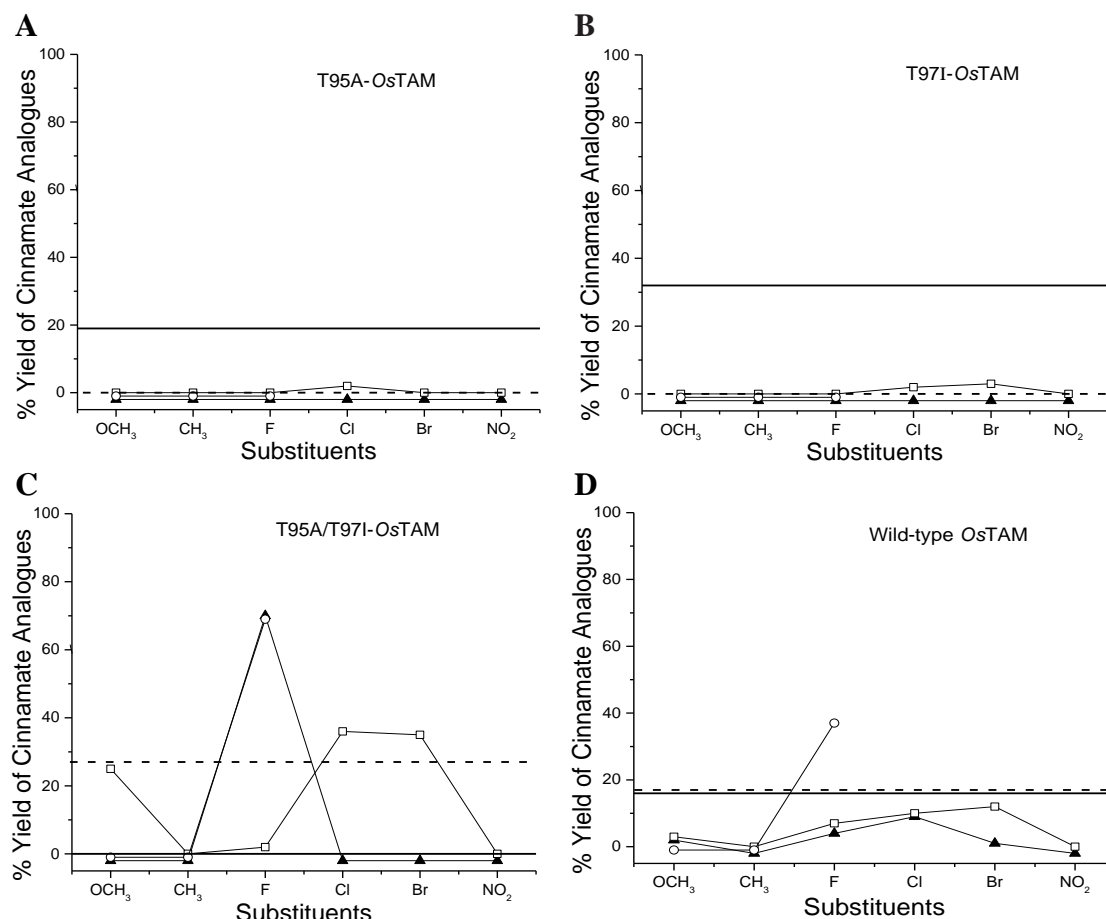


Figure 3.2. The percent yield of trans-cinnamate analogs made biocatalytically from A) T95A-*OsTAM*, B) T97I-*OsTAM*, C) T95A/T97I-*OsTAM*, and D) wild-type *OsTAM* incubated with *p*-(□), *m*-(▲), and *o*-(○)-substituted α -phenylalanines. The dashed line shows the percent yield of cinnamic acid from phenylalanine, and the solid line shows the percent yield of coumaric acid from tyrosine. Standard error = $\pm 5\%$.

Wild-type *OsTAM* turned over phenylalanine to cinnamate (20% conversion) and β -phenylalanine (3% conversion) (Figure 3.2D). Introduction of a T95A or T97I mutation in wild-type *OsTAM* extinguished the lyase (Figure 3.2A and B) and mutase (Figure S44 E and F) activities for phenylalanine. T95A-*OsTAM* and T97I-*OsTAM* also did not turn over the substituted phenylalanine analogs to their β -amino acid products (Figure S44 E and F).

In summary, these data suggest that the natural active site residues (Y125 and N446) in the T95A and T97I mutants retain their substrate specificity for tyrosine, but the relative mutase activity suffers curiously from the loop mutations. Further, these loop mutations apparently hamper the effects of the tyrosyl *p*-OH group needed for catalysis that cannot be rescued by the electronics and sterics of the phenyl ring of phenylalanine or the substituents of its analogs.

The tandem inner loop mutant T95A/T97I-*Os*TAM regained lyase activity over that of the single T95A and T97A mutants for some substrates. T95A/T97I-*Os*TAM was better than wild-type *Os*TAM at turning over larger *p*-halogen (Cl and Br), *p*-OCH₃ substrates, and the smaller *m*-F and *o*-F-substituted substrates (Figure 3.2C and D). The *p*-halogen substrates were turned over at rates that correlated well with their electronic effects as estimated by Hammett σ_{para} constants,⁴ and thus the turnover was less influenced by sterics. To contrast, the larger *m*-halogen (Cl and Br), *m*-OCH₃ and *m*-CH₃ substrates were barely turned over ($\approx 3\%$ turnover), suggesting that the tandem T95A and T97I mutations created a steric bottleneck in catalysis for the *meta*-isomers. Further, the production of β -phenylalanine analogs, including β -tyrosine, made by T95A/T97I-*Os*TAM from each substitute phenylalanine was below the detection limit of the analysis (Figure S45A).

It is worth noting that the coumarate: cinnamate ratio for single mutants T95A-*Os*TAM (100:0) and T97I-*Os*TAM (100:0) showed a preference for tyrosine over phenylalanine in their lyase reactions. While the same ratio for T95A/T97I-*Os*TAM (0:100) had reversed specificity for phenylalanine in its lyase reaction. These latter results suggest that the hydrophilic T95 and T97 may, in part, interact with the OH of the tyrosine substrate.

3.3.3 Combined Inner-Loop (T95 and T97) and Active Site Mutations.

Combined inner-loop and active site mutations were made using the active site double mutant Y125C/N446K-*Os*TAM (with an active site identical to that of *Tc*PAM) as the progenitor of T95A and T97I mutations in the loop sequence. Mutants Y125C/N446K/T95A-*Os*TAM (Figure 3.3A) and Y125C/N446K/T95I-*Os*TAM (Figure 3.3B) showed parallel trends for turning over substrates with *p*-, *m*-, and *o*-substituents, both turning over the *para*-isomers the best. These results were curious because the activities of single loop mutants T95A-*Os*TAM and T97I-*Os*TAM were impaired significantly (Figure 3.2A and B). These data suggest that T95A-*Os*TAM and T97I-*Os*TAM likely have an active site that is sterically more inaccessible, compared to the active site of *Os*TAM, which precludes activity. We showed that the K_M values (Table 2.1) of Y125C/N446K-*Os*TAM are lower for the larger *p*-Cl and *p*-Br substrates (estimating tighter binding) and paradoxically higher for the smaller *p*-F substrate relative to that for the wild-type *Os*TAM. Also, the *p*-OCH₃ substrate was turned over better by Y125C/N446K/T95A-*Os*TAM (Figure 3.3A) and Y125C/N446K/T95I-*Os*TAM (Figure 3.3B) than it was by the Y125C/N446K-*Os*TAM (Figure 3.3D). These results indicated that the T95A and T97I loop mutations helped lock the bulkier substrates into a catalytically competent conformation for the lyase reaction. The data also reveal that the sterics of the active site, the substrate, and the inner loop work jointly towards defining substrate specificity.

A Y125C/N446K/T95A/T97I-*Os*TAM quadruple mutant was made to provide more evidence to support the hypothesis that loop mutations T95A and T97I would increase the turnover of Y125C/N446K-*Os*TAM for bulkier substrates Y125C/N446K/T95A/T97I-*Os*TAM (Figure 3.3C) showed considerably higher lyase activity than Y125C/N446K-, Y125C/N446K/T95A- and Y125C/N446K/T97I-*Os*TAM for all the substituted substrate

isomers, except for the CH₃- and NO₂-substituted isomers. Still, no β -amino acids were made, even as the loop and active site residues more resembled the characterized *Tc*PAM aminomutase. The quadruple mutant also turned over the unsubstituted phenylalanine substrate 2-fold better (40% conversion) than did Y125C/N446K-, Y125C/N446K/T95A- and Y125C/N446K/T97I-*Os*TAM (see Figure 3.3).

The most profound changes in turnover by Y125C/N446K/T95A/T97I-*Os*TAM compared with those by Y125C/N446K/T95A- and Y125C/N446K/T97I-*Os*TAM was for the F-substrate isomers. The products made from *m*- and *o*-F substrates by the latter two mutants were near the detection limit of the GC-MS (Figure 3.3A and B, respectively); the *p*-F product was made at ~20% conversion by Y125C/N446K/T97I-*Os*TAM only. The quadruple mutant boosted the turnover for the *o*-F and *m*-F from ~0% (made by its progenitors) to 10% and 70%, respectively (Figure 3.3C). We noted earlier that the combination of Y125C/N446K/T95A/T97I mutations in *Os*TAM likely creates a tighter binding pocket. Thus, we imagine that substrates with the smaller F-substituent can be held more securely in a catalytic conformation like those substrates with the larger Br- and Cl-substituents. Further, the CH₃- and NO₂-substituted substrates showed slow turnover (<1%) by the quadruple mutant. This observation reinforced that the splayed geometry of these substituents prevented them from binding properly for catalysis with all mutants tested in this study, except for Y125C/N446K-*Os*TAM that turned over the *p*-CH₃ substrate at ~10% (Figure 3.3D).

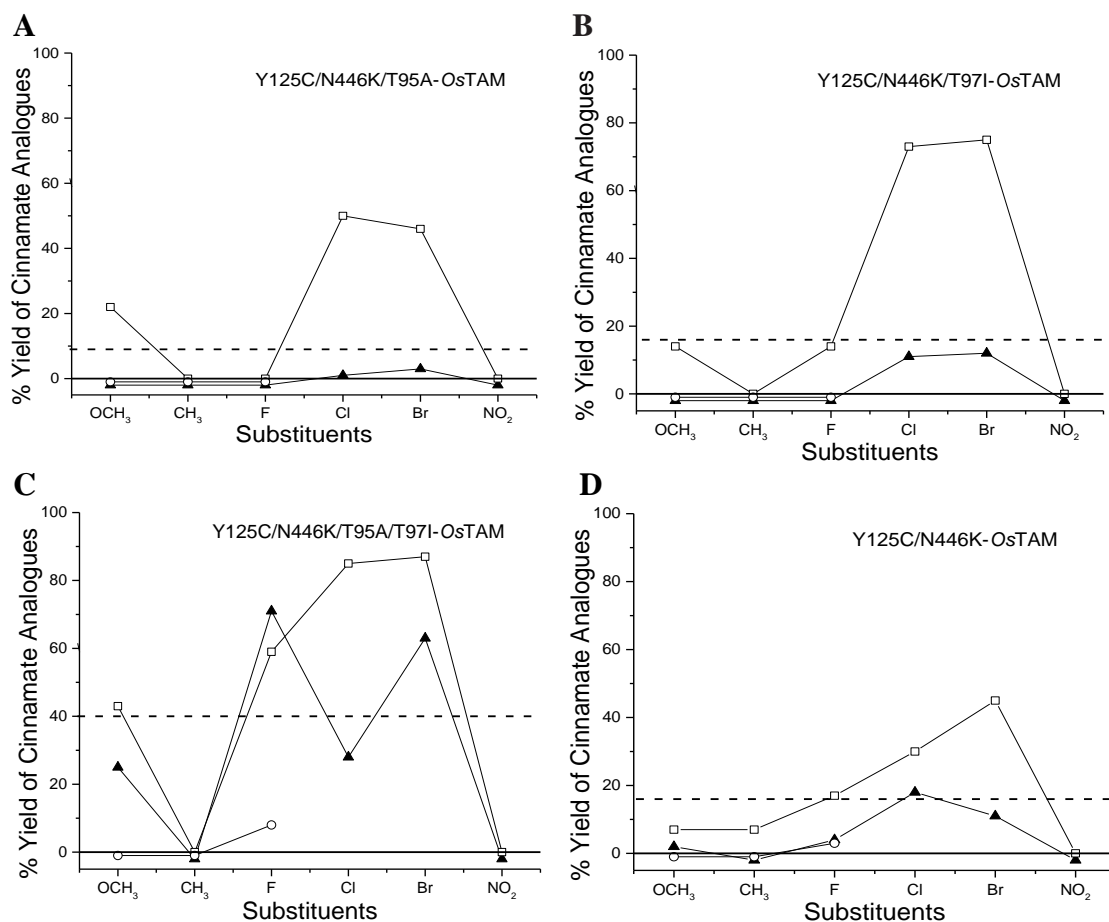


Figure 3.3. The percent yield of trans-cinnamate analogs made biocatalytically from A) Y125C/N446K/T95A-*OsTAM*, B) Y125C/N446K/T97I-*OsTAM*, C) Y125C/N446K/T95A/T97I-*OsTAM*, and D) Y125C/N446K-*OsTAM* (included here from Figure 2.3C for convenience) incubated with *p*-(\square), *m*-(\blacktriangle), and *o*-(\circ)-substituted α -phenylalanines. The dashed line shows the percent yield of cinnamic acid from phenylalanine, and the solid line shows the percent yield of coumaric acid from tyrosine. Standard error = $\pm 5\%$.

3.3.4 Mutation of *OsTAM* Variants with H109S Loop Residue Exchange.

The activity was parsed for various intermediate iterations of an H109S mutation of the inner loop of *OsTAM* on the way to making the Y125C/N446K/T95A/T97I/H109S-*OsTAM* mutant. The H109S exchange replaced the more polar H109 side chain (estimated from the dipole moment of imidazole ~ 3.8 D)⁵ with a relatively less polar S109 residue (estimated from the

dipole moment of ethanol ~ 1.7 D)⁶ to build a more hydrophobic loop and drive the close-loop conformation.

A combined active site/loop mutant N446K/H109S-*Os*TAM and a single loop-mutation H109S-*Os*TAM (Figure 3.4A) catalyzed the turnover of more substrates to their acrylates than did multiple-mutation variants T95A/T97I/H109S- (Figure 3.4C) and Y125C/N446K/T95A/T97I/H109S-*Os*TAM (Figure 3.4D). The latter variants were designed to improve the match with active site and loop sequences of the characterized *Tc*PAM mutase (Figure 3.1B). However, as for many of the *Os*TAM mutants made in this study, low (<3% conversion), if any, aminomutase activity was measured for a mutant containing an H109S exchange. An interesting observation is how the H109S exchange in the loop of cognates T95A/T97I-*Os*TAM and Y125C/N446K/T95A/T97I-*Os*TAM caused them to lose their activity dramatically for all substrates (Figure 3.4C and D).

Further, the selectivity for the *m*- over *p*-substituted substrates with N446K/H109S-*Os*TAM (Figure 3.4B) was reciprocal to the *p*- over *m*-substituted substrate specificity with N446K-*Os*TAM (Figure 3.3A). Also, sterics appear to influence the turnover rate of N446K/H109S-*Os*TAM with the substrates from the *m*-halogen series, while electronic effects appear to dominate the reactivity of N446K-*Os*TAM with the same substrates. By comparison, electronic effects appear to guide the turnover rate of N446K/H109S-*Os*TAM with the *p*-halogen series, while sterics influence the relative turnover rates of N446K-*Os*TAM with the same *p*-halogen substrates. Further, the overall reactivity of N446K/H109S-*Os*TAM was lower than that of N446K-*Os*TAM, indicating the H109S obstructs catalysis. It becomes more apparent that the interplay of residues within the loop structure, between the loop and other parts of the MIO

enzyme, and between the loop and the substrate orientation are unclear. It is therefore difficult to explain the effects caused by the H109S exchange.

3.3.5 Mutation of *Os*TAM Variants with H109S/F115L Loop Residue Exchanges.

Residues within the loop structure of *Os*TAM were changed from hydrophilic to hydrophobic to drive the equilibrium of the loop to its closed conformation. This closed topology, in theory, would stimulate retention of the reaction intermediate to promote the aminomutase activity for phenylalanine. Intrinsically hydrophobic residues of the characterized *Tc*PAM mutase were used to replace positionally similar residues in the *Os*TAM loop to make the loop sequences identical.

In an earlier study,¹ residue L97 was the proposed hinge of the inner loop of *Tc*PAM at an α -helix:loop junction and considered crucial to mobilizing the loop during catalysis. The earlier study projected that an L97G mutation reduced sterics and induced the highest loop mobility, allowing more backbone flexibility at this pivotal position.¹ This flexion mutation was proposed to cause the α -helix to shorten and the inner loop to lengthen; highlighted as the key to switching the *Tc*PAM mutase activity to that of a lyase. Our objective was reciprocal, to change the intrinsic lyase activity of *Os*TAM, and its mutants, to that of the *Tc*PAM mutase. L97 of *Tc*PAM aligns with F115 of *Os*TAM in the hinge position of the inner loop. Hence, an F115L mutation of *Os*TAM was targeted to shorten the loop as purported in *Tc*PAM, reduce loop flexibility, and thereby stimulate mutase activity. The target multiple-mutant Y125C/N446K/T95A/T97I/H109S/F115L-*Os*TAM was made, and its activity was compared against that of other mutant iterations of the inner loop and active site.

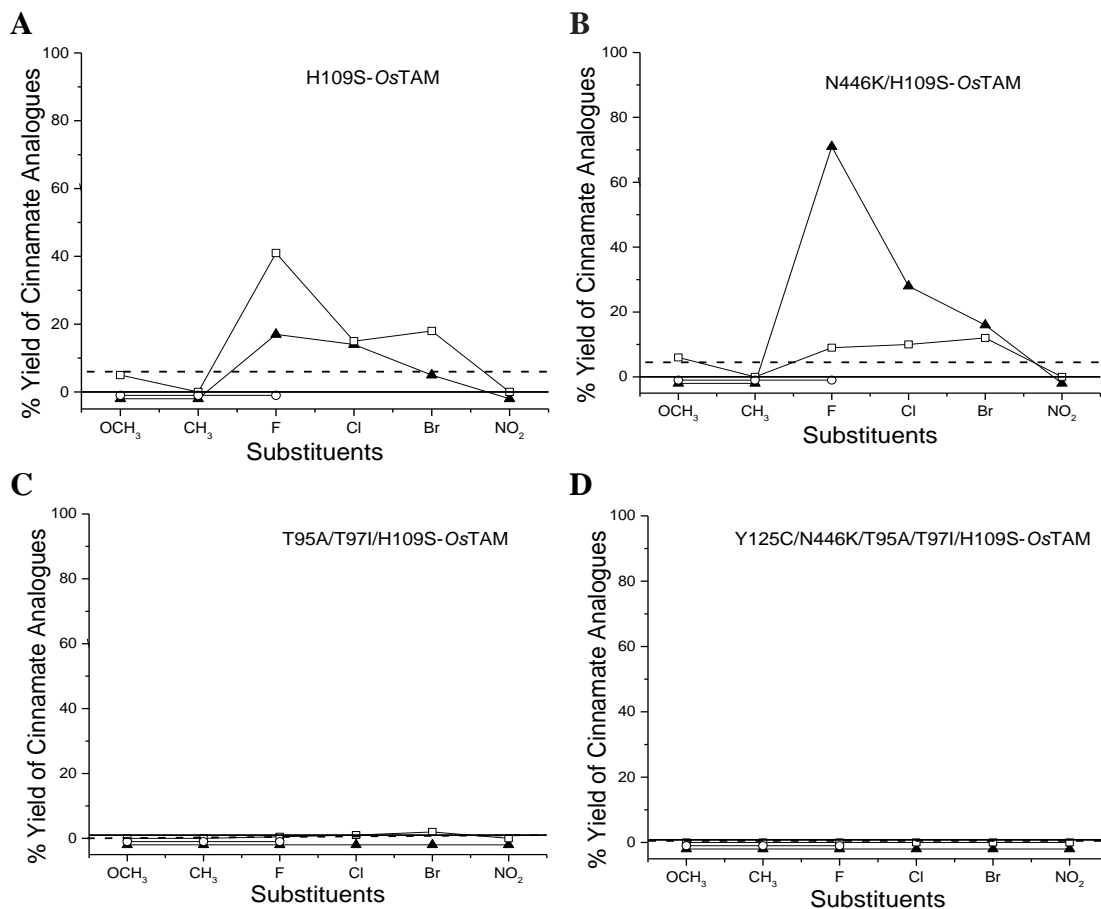


Figure 3.4. The percent yield of *trans*-cinnamate analogs made biocatalytically from A) H109S-OsTAM, B) N446K/H109S-OsTAM, C) T95A/T97I/H109S-OsTAM, and D) Y125C/N446K/T95A/T97I/H109S-OsTAM incubated with *p*-(□), *m*-(▲), and *o*-(○)-substituted α -phenylalanines. The dashed line shows the percent yield of cinnamic acid from phenylalanine, and the solid line shows the percent yield of coumaric acid from tyrosine. Standard error = $\pm 5\%$.

The single F115L-OsTAM mutant showed no mutase activity. It had greater lyase activity than that of the wild-type OsTAM (Figure 3.3D), particularly for the smaller *m*- and *p*-F substrates, while both catalysts turned over the larger OCH₃-, CH₃-, Cl- and Br-isomers about the same ($\leq 20\%$ conversion) (Figure 3.5A). The turnover of the *m*- and *p*-F substrates increased relative to that of the *o*-F isomer. We propose that some fortuitous fluoro-H-bonding interaction aligns the *m*- and *para*-isomers for catalysis and enhances turnover. Other mutants that catalyzed similar selectivity were Y125C/N446K/T95A/T97I-OsTAM (Figure 3.3C) and H109S-OsTAM

(Figure 3.4A). This fluoro-dependent turnover is likely absent in F115L-*Os*TAM for the *o*-F- and unsubstituted-phenylalanine substrates, which were turned over slower by F115L-*Os*TAM (Figure 3.5A) than by wild-type *Os*TAM (Figure 3.3D). The *o*-F substrate likely has intramolecular torsional interactions that guide the specificity of F115L-*Os*TAM for fluoro-substrates. The trend shows the conversion of *m*- and *p*-F substrates > *o*-F and phenylalanine substrates (the latter two are turned over at about the same rate).

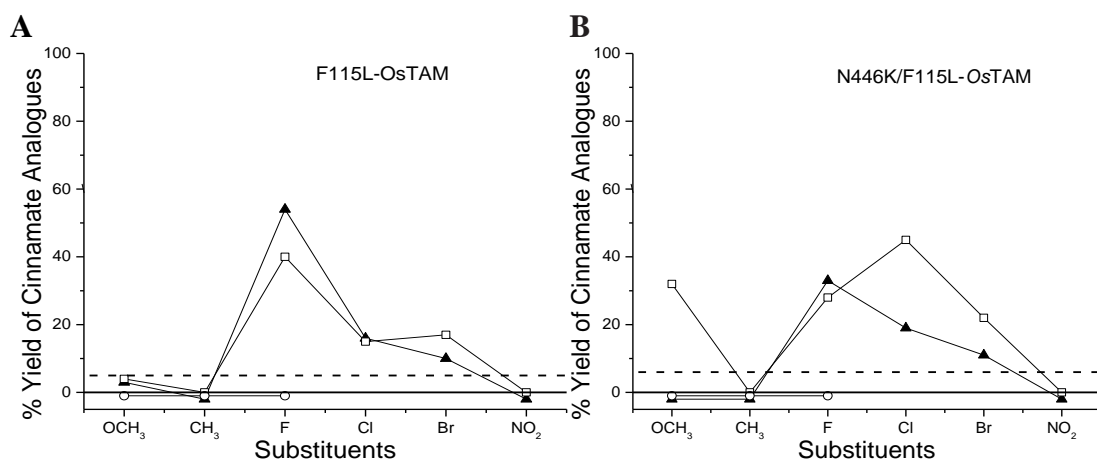


Figure 3.5. The percent yield of trans-cinnamate analogues for A) F115L-*Os*TAM and B) N446K/F115L-*Os*TAM were incubated with *p*- (□), *m*- (▲), and *o*- (○)-substituted α -phenylalanines. The dashed line shows the percent yield of cinnamic acid from phenylalanine, and the solid line shows the percent yield of coumaric acid from tyrosine. Standard error = \pm 5%.

The other active F115L "hinge residue" mutant (N446K/F115L-*Os*TAM) behaved similarly to F115L-*Os*TAM in turning over the substituted phenylalanines. The outlier, the *p*-OCH₃ substrate was turned over 8-fold better by N446K/F115L-*Os*TAM than by F115L-*Os*TAM, suggesting possible steric relief, which was proposed for the same *p*-OCH₃ substrate with N446K-*Os*TAM (see Figure 3.5).

3.3.6 Other Mutants Containing the F115L Mutation.

T95A/T97I/F115L-, Y125C/N446K/T95A/T97I/F115L-, T95A/T97I/H109S/F115L-, and Y125C/N446K/T95A/T97I/H109S/F115L-*Os*TAM barely turned over the substrates (<3%) (Figure S49). The activity of Y125C/N446K/T95A/T97I/H109S/F115L-*Os*TAM was poor like its progenitor Y125C/N446K/T95A/T97I/H109S-*Os*TAM, but significantly poorer than an earlier generation mutant Y125C/N446K/T95A/T97I-*Os*TAM (see Figure 3.3C). The latter observations demonstrate the importance of H109 and F115 to the lyase function of Y125C/N446K/T95A/T97I-*Os*TAM. The introduction of either H109S, F115L or H109S and F115L into progenitor T95A/T97I-*Os*TAM (Figure 3.2C) abrogated the activity with any substrate. Thus, as expected, an F115L exchange in the loop did not recover the function of the inactive Y125C/N446K/T95A/T97I/H109S-*Os*TAM (Figure S49).

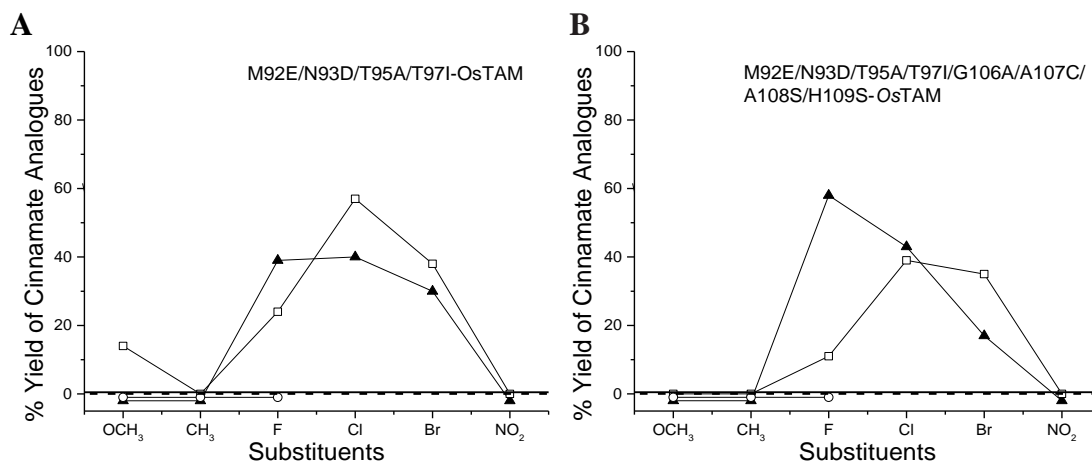


Figure 3.6. The percent yield of trans-cinnamate analogs for A) M92E/N93D/T95A/T97I-*Os*TAM and B) M92E/N93D/T95A/T97I/G106A/A107C/A108S/H109S-*Os*TAM incubated with *p*-(□), *m*-(▲), and *o*-(○)-substituted α -phenylalanines. The dashed line shows the percent yield of cinnamic acid from phenylalanine, and the solid line shows the percent yield of coumaric acid from tyrosine. Standard error = \pm 5%.

3.3.7 Multiple Mutations to "Evolve" the *Os*TAM Loop to that of *Tc*PAM.

A central dogma proposed in an earlier study was that the hydrophobic properties of the inner loop structure covering the active site alone defined the mutase and lyase activities of MIO-dependent catalysts.¹ We thus focused on retaining the wild-type active site residues Y125 and N446 of *Os*TAM but changing its loop sequence to match that of *Tc*PAM. A progenitor loop mutant M92E/N93D/T95A/T97I-*Os*TAM and the entire *Os*TAM→*Tc*PAM loop mutant M92E/N93D/T95A/T97I/G106A/ A107C/A108S/H109S-*Os*TAM were made. The latter mutant lacked the last three C-terminal residues (K113N/E114Q /F115L) of the loop because a suitable cDNA expression plasmid could not be made. We expected to see a least a small amount of β -amino acid made after changing the entire loop of *Os*TAM to look more like that of *Tc*PAM, but the amino acids were below the detection limit of our analysis (data not shown).

The turnover of all the substrates catalyzed by M92E/N93D/T95A/T97I-*Os*TAM (Figure 3.6) in this study followed a trend similar to that seen for Y125C/N446K/T95A/T97I-*Os*TAM, H109S-*Os*TAM, and F115L-*Os*TAM (Figure 3.3C, Figure 3.4A, and Figure 3.5A, respectively). Each mutant turned over the *m*- and *p*-F substrates at a higher rate than that of the *o*-F isomer. With these mutants, the *o*-F-isomer and the other *o*-substituted substrates were not turned over. M92E/N93D/T95A/T97I/G106A/A107C/A108S/H109S-*Os*TAM turned over all the substrates to their acrylates similar to that of its shorter cognate. A noticeable difference in the catalysis by the longer loop mutant is the 6-fold difference in turnover of the *p*- (10% conversion) and *m*-F (~60% conversion) substrates compared to the ~2-fold difference in turnover by M92E/N93D/T95A/T97I-*Os*TAM, where the turnover of the *m*-substrate predominated. These observations enforce that the loop likely helps position the regioisomeric *m*- and *p*-F substrates differently in the active site through a migrant H-bond contact. Consistent with this claim, the

turnover of the larger, non-H-bonding *m*- and *p*-Cl and -Br- substrates changed little between the two loop mutants (see Figure 3.6).

3.4 Conclusions

The active site of an MIO enzyme comprises active site binding contacts and catalytic residues. Another feature of the active site is the inner loop structure that opens and closes over the active site entry port. An earlier study introduced hydrophilic residues into the loop so it would be in a solvent-exposed, open conformation. This effort increased the lyase:mutase product ratio of an aminomutase over that of the cognate wild-type enzyme.¹ We viewed that this seminal earlier study had found a common feature among the MIO-family of aminomutases that could predictably control the ratio of the intrinsic aminomutase and ammonia lyase activities. Here, we employed a reciprocal strategy to mutate residues of the *OsTAM* loop to force it into its purportedly closed conformation, retain the reaction intermediate for reamination, and thus increase the mutase:lyase product ratio. Targeted mutations to increase the hydrophobic character of the loop did not change the intrinsic mutase:lyase activity ratio of *OsTAM* mutants that already worked predominantly as lyases with specificity for phenylalanine analogs. There are likely several unpredictable intramolecular interactions between residues within the MIO enzyme loop structure, between the loop and other parts of the enzyme, and between the loop and the substrate. The complexity of this reaction network makes parsing its details with single experiments complicated. Dissecting the duality of the MIO-enzyme mechanism will likely require examination of multiple family members to find key common structural and sequence features that when altered can predictably shift the balance between the mutase and lyase reactivities.

APPENDIX

Instrumentation

GC-MS analysis was performed on an Agilent 6890N gas chromatograph equipped with a capillary GC column (30 m × 0.25 mm × 0.25 μM; HP-5MS; J & W Scientific) with He as the carrier gas (flow rate, 1 mL/min). The injector port (at 250 °C) was set to splitless injection mode. A 1-μL aliquot of each sample was injected using an Agilent 7683 auto-sampler (Agilent, Atlanta, GA). The column temperature was increased from 200 – 220 °C at 8 °C/min with a 13 min hold, then increased by 50 °C/min to 250 °C, and returned to 200 °C over 5 min, with a 5 min hold for tyrosine and *para*-coumarate detection; the column temperature was increased from 50 – 110 °C at 30 °C/min then increased by 10 °C/min to 250 °C, and returned to 50 °C over 5 min, with a 5 min hold for phenylalanine and cinnamate detection. The gas chromatograph was coupled to a mass selective detector (Agilent, 5973 inert) operated in electron impact mode (70 eV ionization voltage). All spectra were recorded in the mass range of 50 – 400 *m/z* to analyze amino acid and acrylate derivatives.

Table S1. Primers^a Used to Make *ostam* cDNA Mutants.

Y125C: 5'-GAA CTG ATC CGT <u>T</u> G T CTG AAC GCT GGC-3' and 5'-GCC AGC GTT CAG <u>A</u> C A ACG GAT CAG TTC-3'
N446K: 5'-GAC TAT GGC TTT <u>A</u> AG GGT GCG GAA GTG-3' and 5'- CAC TTC CGC ACC <u>C</u>TT AAA GCC ATA GTC-3'
T95A: 5'-CTA CGA TGA ATG <u>G</u> T G CCG ACA CCT ATG G-3' and 5'-CCA TAG GTG TCG <u>G</u> C A CCA TTC ATC GTA G-3'
T97I: 5'-GAA TGG TAC CGA <u>C</u> A T CTA TGG TGT CAC C-3' and 5'-GGT GAC ACC ATA <u>G</u> A T GTC GGT ACC ATT C-3'
T95A/T97I: 5'-CTA CGA TGA ATG <u>G</u> T G CCG ACA <u>T</u> C T ATG GTG TCA C-3' and 5'-GTG ACA CCA TAG <u>A</u> T G TCG <u>G</u> C A CCA TTC ATC GTA G-3'
H109S: 5'-CGG TGC GGC <u>C</u> AG TCG TCG CAC-3' and 5'-GTG CGA CGA <u>C</u>TG GCC GCA CCG-3'
F115L: 5'-CGC ACC AAA GAA <u>T</u> T A GCA GCT CTG CAG-3' and 5'-CTG CAG AGC TGC <u>T</u> A A TTC TTT GGT GCG-3'
Y125F: 5'-GAA CTG ATC CGT <u>T</u> T T CTG AAC GCT GG-3' and 5'-CCA GCG TTC AGA <u>A</u> A A CGG ATC AGT TC-3'
M92E/N93D/T95A/T97I: 5'-CGA TTC TAC <u>G</u> G A <u>G</u> G A TGG <u>T</u> G C CGA <u>C</u> A T CTA TGG TGT CAC-3' and 5'-GTG ACA CCA TAG <u>A</u> T G TCG <u>G</u> C A CCA <u>T</u> C C <u>T</u> C C GTA GAA TCG-3'
G106A/A107C/A108S/H109S: 5'-CCG GTT TTG GCG <u>C</u> T T <u>G</u> T T <u>C</u> C A <u>G</u> T C GTC GCA CC-3' and 5'-GGT GCG ACG <u>A</u> C A <u>G</u> G A <u>A</u> C A <u>A</u> G C GCC AAA ACC GG-3'
K113N/E114Q/F115L: 5'-CGT CGC ACC <u>A</u> A T <u>C</u> A A <u>T</u> T A GCA GCT CTG CAG-3' and 5'-CTG CAG AGC TGC TAA TTG <u>T</u> A A <u>T</u> T G <u>A</u> T T GGT GCG ACG-3'

^aMutated bases are underlined and bold.

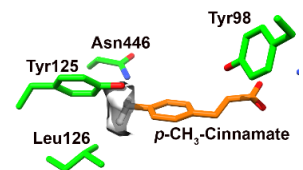
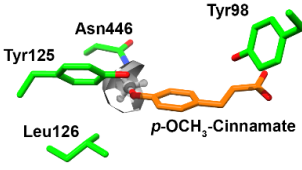
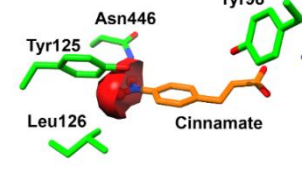
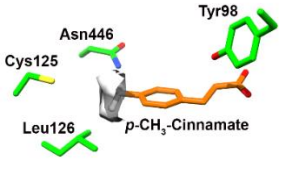
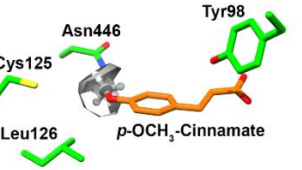
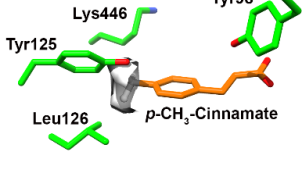
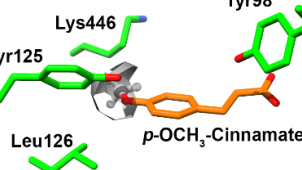
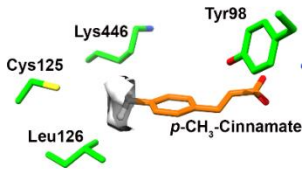
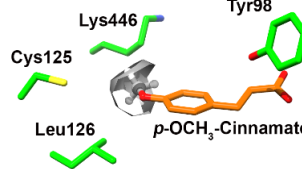
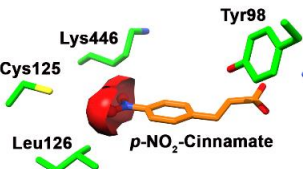
Table S2. Primers Used to Make *Os*TAM Loop Mutations Analogous to Loop of *Tc*PAM.

	Primer 1	Primer 2	Primer 3
<i>Os</i> PAM	ED <u>G</u> A D I YGVTTGFG <u>A</u> C SS <u>R</u> R T NQL		
<i>Os</i> TAM	MNGTDTYGVTTGFGGAAHRRTKEF		
<i>Tc</i> PAM	ED <u>G</u> A D I YGVTTGFG <u>A</u> C SS <u>R</u> R T NQL		
Primer 1:	5'-TTCGATTCTACGGAGGATGGTGCCGACATCTATGGTGTCAC-3'		
Primer 2:	5'-TTGGTGCGACGACTGGAACAAGCGCCAAAACCGG-3'		
Primer 3:	5'-TCGTCGCACCAATCAATTAGCAGCTCTGCAG-3'		

Table S3. Plasmids Containing *ostam* cDNA Mutants.

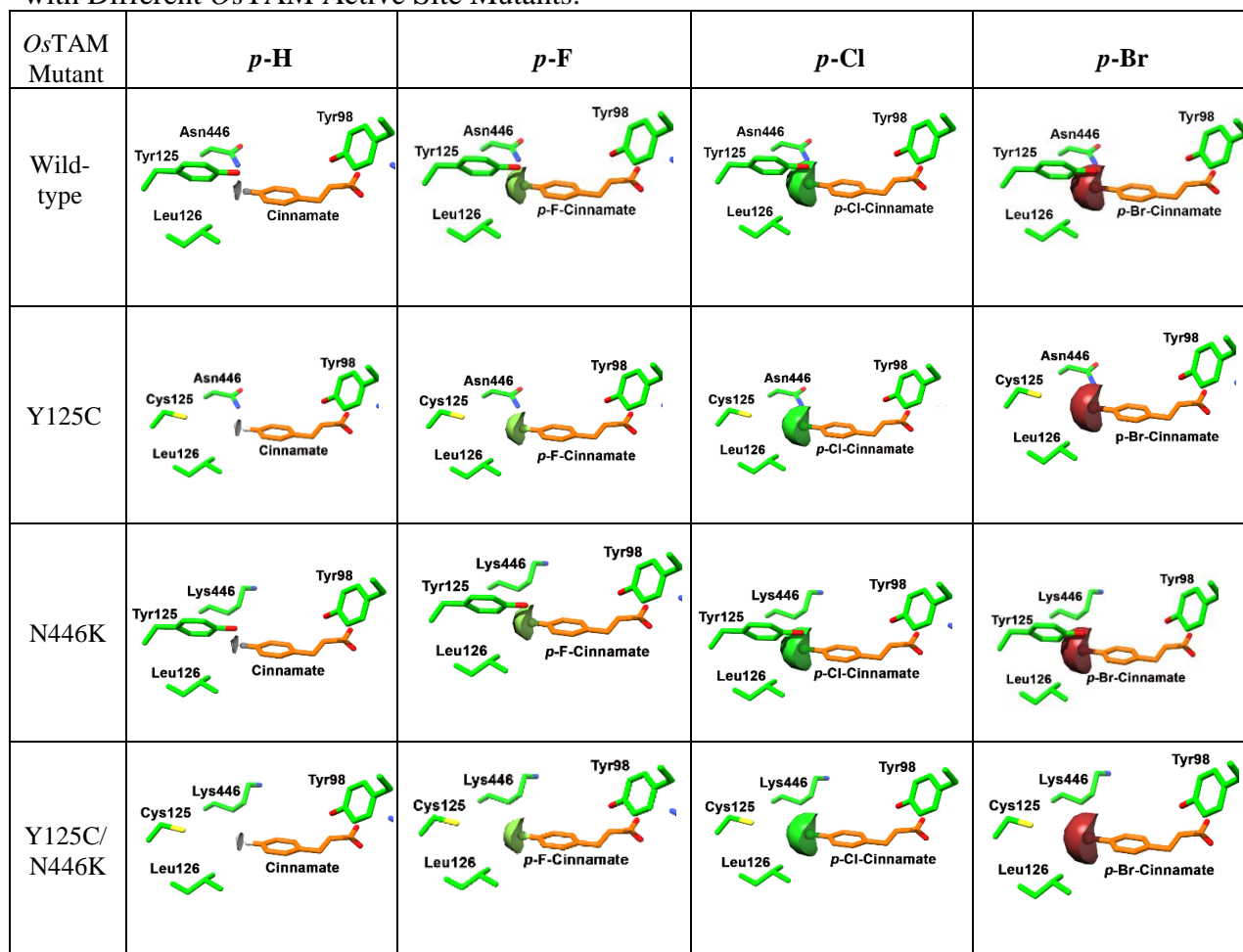
<p>Active Site Mutants pY125C-ostam pN446K-ostam pY125C/N446K-ostam</p> <p>Loop Mutants pT95A-ostam pT97I-ostam pF115L-ostam pH109S-ostam pT95A/T97I-ostam pT95A/T97I/F115L-ostam pT95A/T97I/H109S-ostam pT95A/T97I/F115L/H109S-ostam</p> <p>Active Site and Loop Mutants pY125C/N446K/T95A-ostam pY125C/N446K/T97I-ostam pY125C/N446K/F115L-ostam pY125C/N446K/T95A/T97I-ostam pY125C/N446K/T95A/T97I/F115L-ostam pY125C/N446K/T95A/T97I/H109S-ostam pY125C/N446K/T95A/T97I/F115L/H109S-ostam pN446K/F115L-ostam pN446K/H109S-ostam</p>

Table S4. Space Filling Arrangement of *para*-CH₃, -OCH₃, and -NO₂ Substituted Substrates with Different *Os*TAM Active Site Mutants^a

<i>Os</i> TAM Mutant	<i>p</i> -CH ₃	<i>p</i> -OCH ₃	<i>p</i> -NO ₂
Wild-type			
Y125C			
N446K			
Y125C/ N446K			

^aThe substituted substrates (orange) were modeled in the mutants based on the cinnamate complex in *Tc*PAM (PDB: 3NZ4). Residues in the aryl binding pocket and the catalytic tyrosine-98 of the wild-type and mutants are shown in green (heteroatoms colored as follows: oxygen (red), nitrogen (blue), and sulfur (yellow)). The space-filling rendering was done with UCSF Chimera 1.12. Heteroatom of substituents are colored accordingly: oxygen (red), nitrogen (blue), and carbon (gray).

Table S5. Space Filling Arrangement of *para*-F, -Cl, and -Br Substituted and α -Phenylalanine with Different *Os*TAM Active Site Mutants.^a



^aThe substituted substrates (orange) were modeled in the mutants based on the cinnamate complex in *Tc*PAM (PDB: 3NZ4). Residues in the aryl binding pocket and the catalytic tyrosine-98 of the wild-type and mutants are shown in green (heteroatoms colored as follows: oxygen (red), nitrogen (blue), and sulfur (yellow)). The space-filling rendering was done with UCSF Chimera 1.12. Heteroatom of substituents are colored accordingly: oxygen (red), nitrogen (blue), and carbon (gray).

Table S6. Kinetic Parameters of *OsTAM* T95A/T97I-Mutants for α -Phenylalanine and Its Analogs.

<i>OsTAM</i> type	<i>p</i> -Br		<i>p</i> -Cl		<i>p</i> -F		<i>para</i> -H (no substituent)	
	k_{cat} (10^{-3} s^{-1})	K_M (mM)	k_{cat} (10^{-3} s^{-1})	K_M (mM)	k_{cat} (10^{-3} s^{-1})	K_M (μM)	k_{cat} (10^{-3} s^{-1}) ^a	K_M (mM) ^a
Y125C/N446K/T95A/T97I	47 ± 7	0.4 ± 0.2	46 ± 3	0.3 ± <0.1	21 ± 3	0.2 ± 0.1	23 ± 5	0.4 ± 0.1
T95A/T97I	25 ± 2	0.4 ± 0.1	23 ± 1.5	0.5 ± <0.1	15 ± 3	0.6 ± 0.1	22 ± 3	0.3 ± 0.1

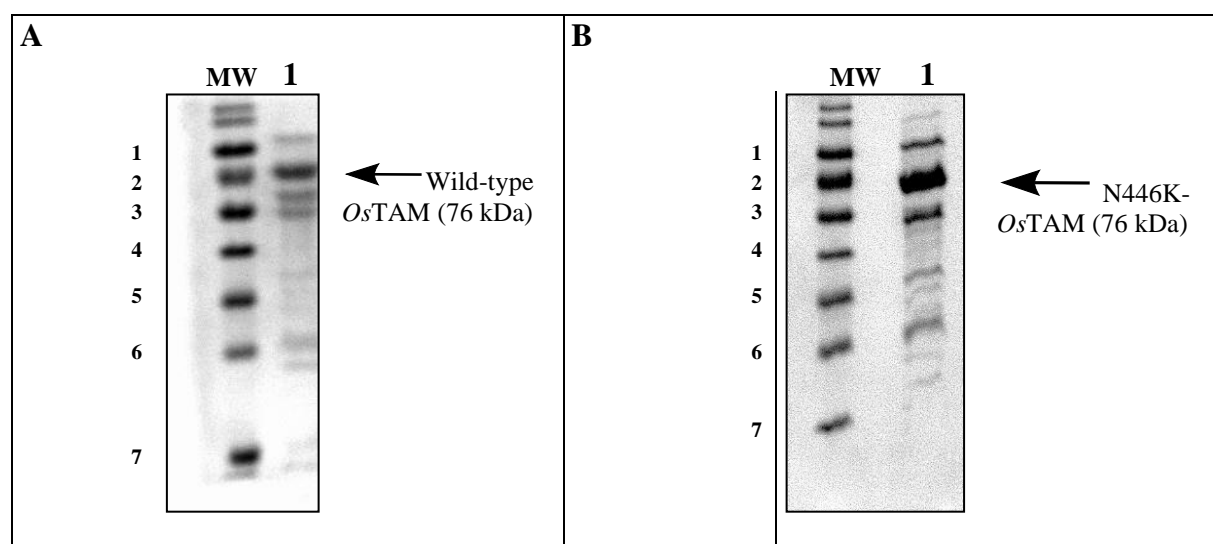


Figure S1. SDS-PAGE gel of A) wild-type *OsTAM* after Coomassie blue staining. Purity (55%) estimated by a Kodak Gel Logic 100 Imaging System; lane MW: PageRuler® Prestained Ladder, lane 1: Enzyme (10 μL of a $\sim 4.2 \text{ mg/mL}$ solution) and of B) N446K-*OsTAM* after Coomassie blue staining. Purity (60%) estimated by a Kodak Gel Logic 100 Imaging System; lane MW: PageRuler® Prestained Ladder, lane 1: Enzyme (10 μL of a $\sim 5.6 \text{ mg/mL}$ solution). PageRuler® Prestained Ladder: MW (kDa) – 1: 100 kDa, 2: 70 kDa, 3: 55 kDa, 4: 40 kDa, 5: 35 kDa, 6: 25 kDa, and 7: 15 kDa.

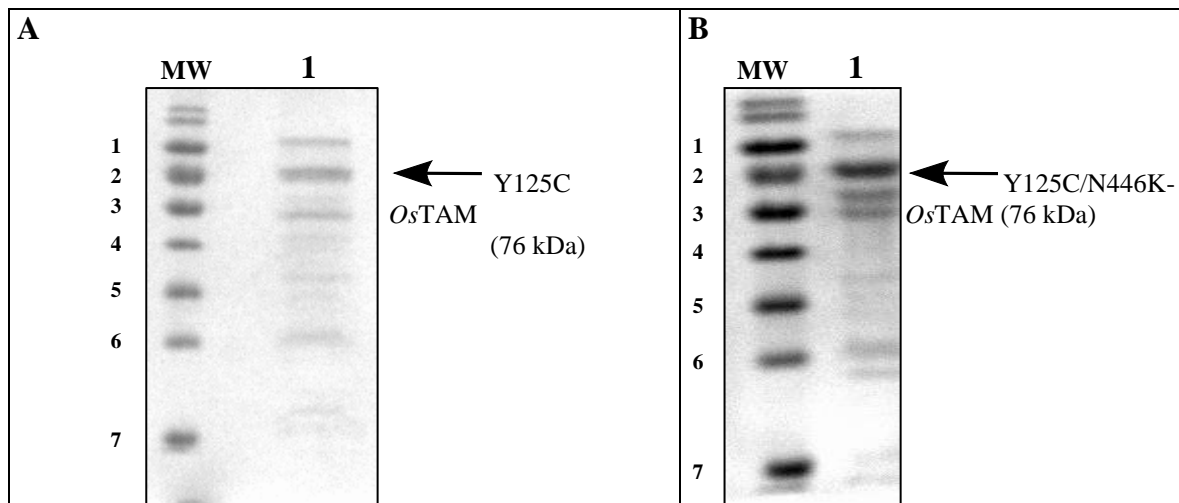


Figure S2. SDS-PAGE gel of A) Y125C-OsTAM after Coomassie blue staining. Purity (55%) estimated by a Kodak Gel Logic 100 Imaging System; lane 1: PageRuler © Pre-stained Ladder (see **Figure S1**), lane MW: Enzyme (5 μ L of a \sim 3.0 mg/mL solution) and of B) Y125C/N446K-OsTAM after Coomassie blue staining. Purity (50%) estimated by a Kodak Gel Logic 100 Imaging System; lane MW: PageRuler © Prestained Ladder (see **Figure S1**), lane 1: Enzyme (10 μ L of a \sim 2.7 mg/mL solution).

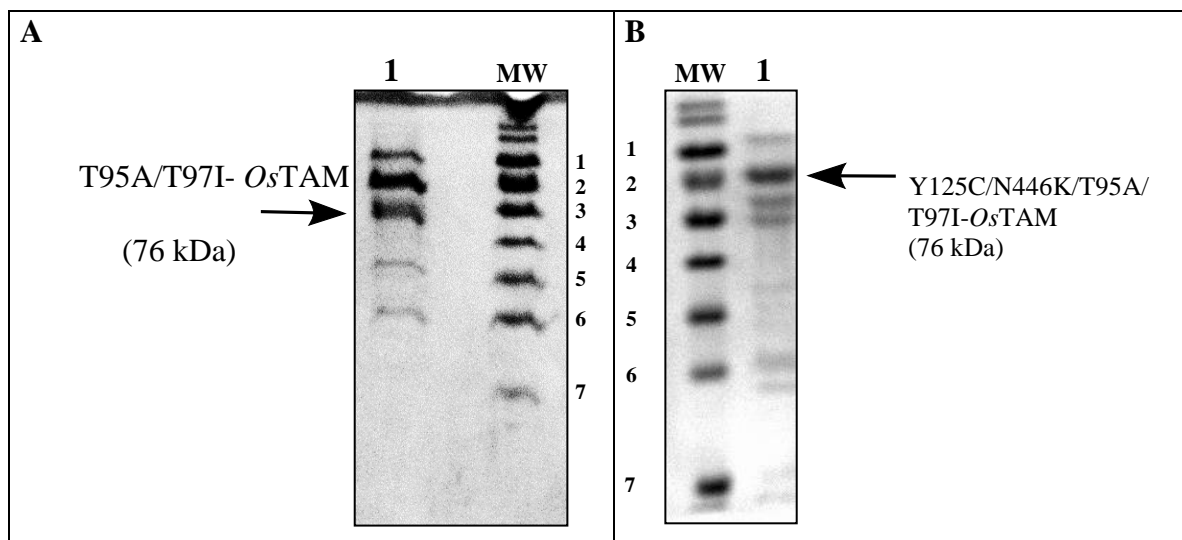


Figure S3. SDS-PAGE gel of A) T95A/T97I-OsTAM after Coomassie blue staining. Purity (65%) estimated by a Kodak Gel Logic 100 Imaging System; lane MW: PageRuler© Prestained Ladder (see **Figure S1**), lane 1: Enzyme (10 μ L of a \sim 2.3 mg/mL solution) and of B) Y125C/N446K/T95A/T97I-OsTAM after Coomassie blue staining. Purity (52%) estimated by a Kodak Gel Logic 100 Imaging System; lane MW: PageRuler © Prestained Ladder (see **Figure S1**), lane 1: Enzyme (10 μ L of a \sim 5.4 mg/mL solution).

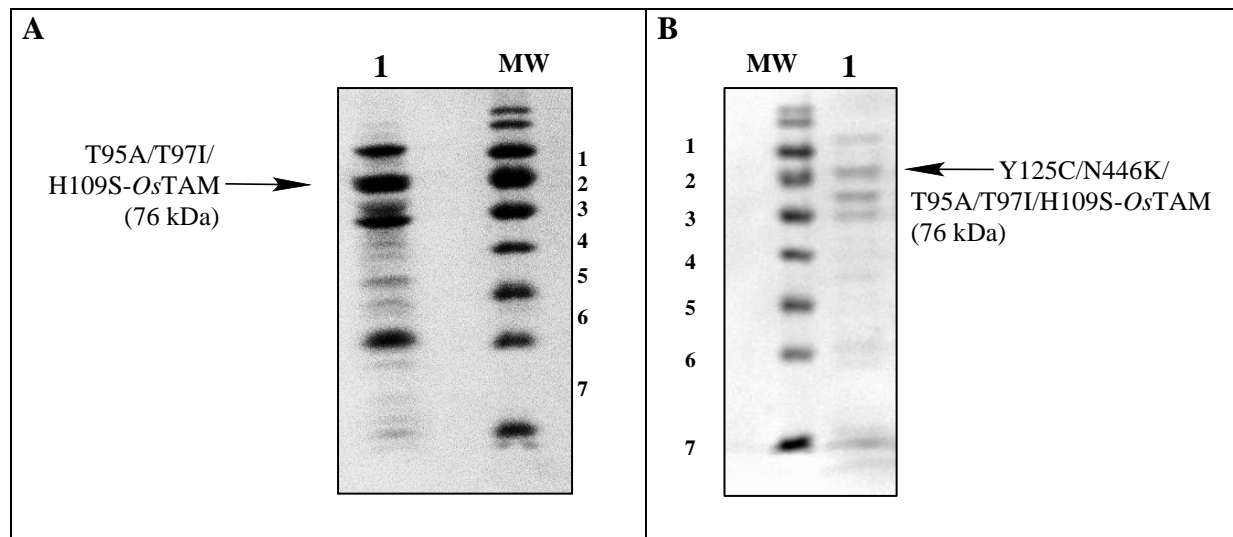


Figure S4. SDS-PAGE gel of A) T95A/T97I/H109S-*OsTAM* after Coomassie blue staining. Purity (62%) estimated by a Kodak Gel Logic 100 Imaging System; *lane MW*: PageRuler © Prestained Ladder (see **Figure S1**), *lane 1*: Enzyme (10 μ L of a \sim 4.6 mg/mL solution) and of B) Y125C/N446K/T95A/T97I/H109S-*OsTAM* after Coomassie blue staining. Purity (48%) estimated by a Kodak Gel Logic 100 Imaging System; *lane MW*: PageRuler © Prestained Ladder (see **Figure S1**), *lane 1*: Enzyme (5 μ L of a \sim 3.4 mg/mL solution).

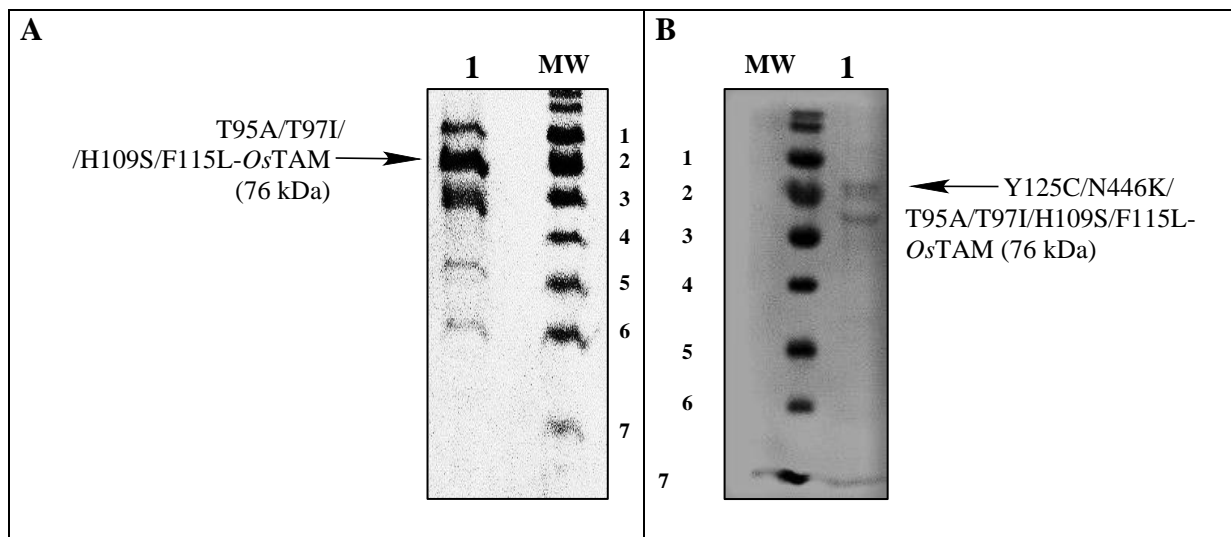


Figure S5. SDS-PAGE gel of A) T95A/T97I/H109S/F115L-*OsTAM* after Coomassie blue staining. Purity (65%) estimated by a Kodak Gel Logic 100 Imaging System *lane* 1: Enzyme (10 μ L of a \sim 5.3 mg/mL solution), *lane* MW: PageRuler $\text{\textcircled{C}}$ Prestained Ladder (see **Figure S1**), and of B) Y125C/N446K/T95A/T97I/H109S/F115L-*OsTAM* after Coomassie blue staining. Purity (55%) estimated by a Kodak Gel Logic 100 Imaging System, *lane* MW: PageRuler $\text{\textcircled{C}}$ Prestained Ladder (see **Figure S1**), *lane* 1: Enzyme (5 μ L of a \sim 6.2 mg/mL solution).

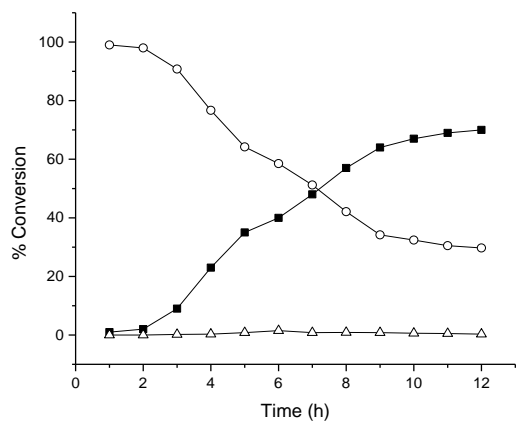
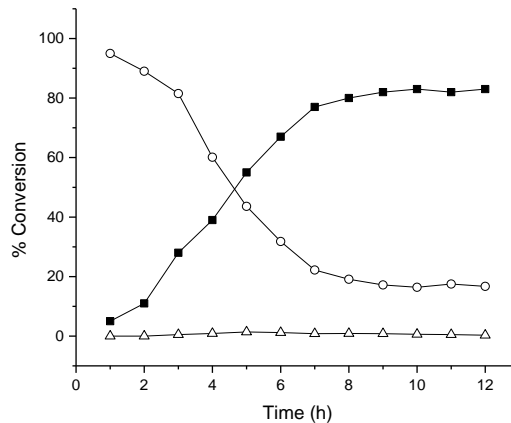
A**B**

Figure S6. Conversion of *p*-Br-phenyl- α -alanine (\circ) (3 mM) to *p*-Br-phenyl- β -alanine (Δ) and *p*-Br-cinnamate (\blacksquare) over 12 h by A) Y125C/N446K-*OsTAM* and B) N446K-*OsTAM*.

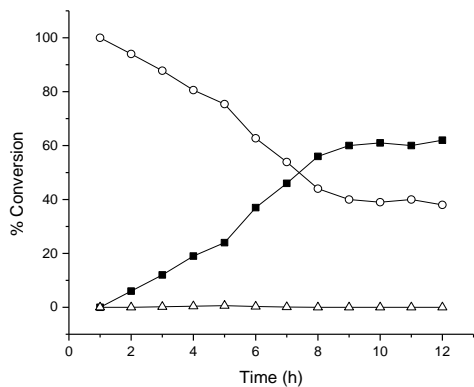


Figure S7. Conversion of α -phenylalanine (\circ) (3 mM) to β -phenylalanine (Δ) and cinnamate (\blacksquare) over 12 h by wild type-*OsTAM*.

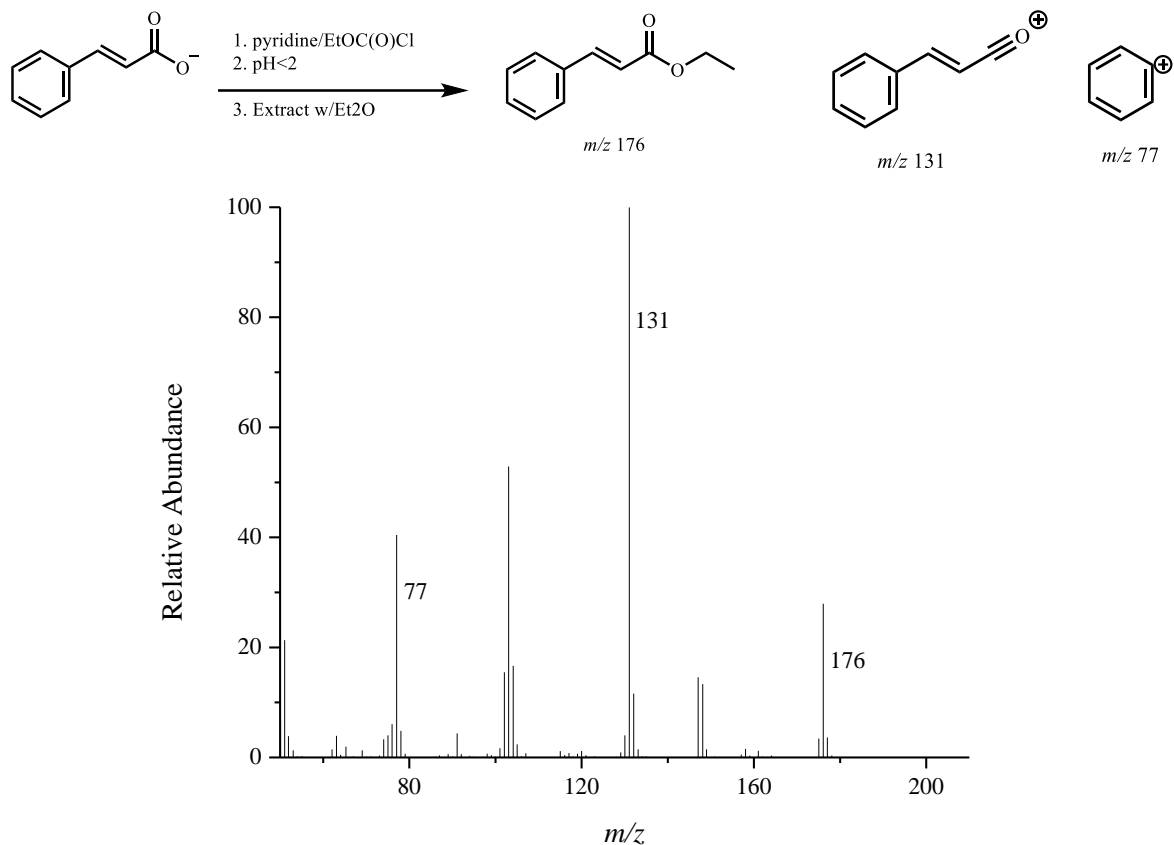


Figure S8. EI-MS of ethyl ester of authentic (*E*)-cinnamate.

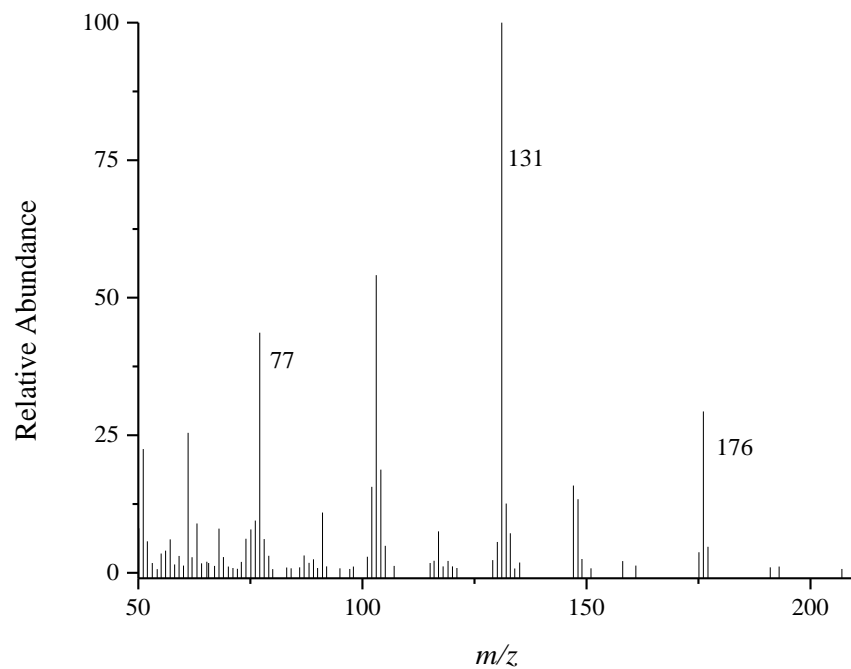


Figure S9. EI-MS of ethyl ester of (*E*)-cinnamate biocatalyzed by N446K-*Os*TAM from (*2S*)- α -phenylalanine.

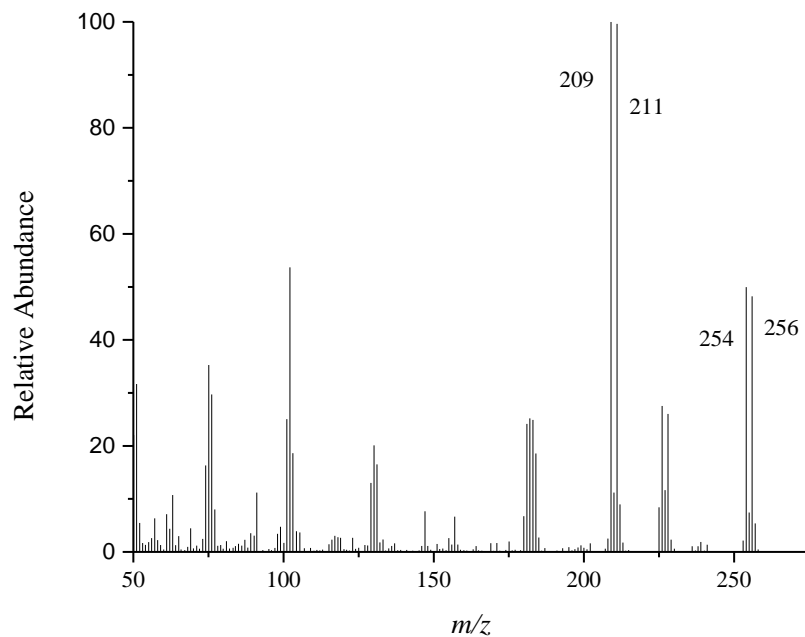
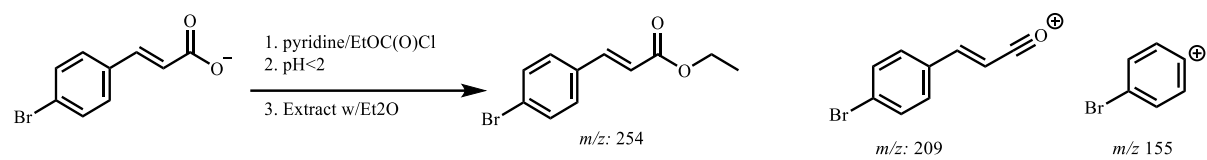


Figure S10. EI-MS of ethyl ester of authentic (*E*)-*p*-Br-cinnamate.

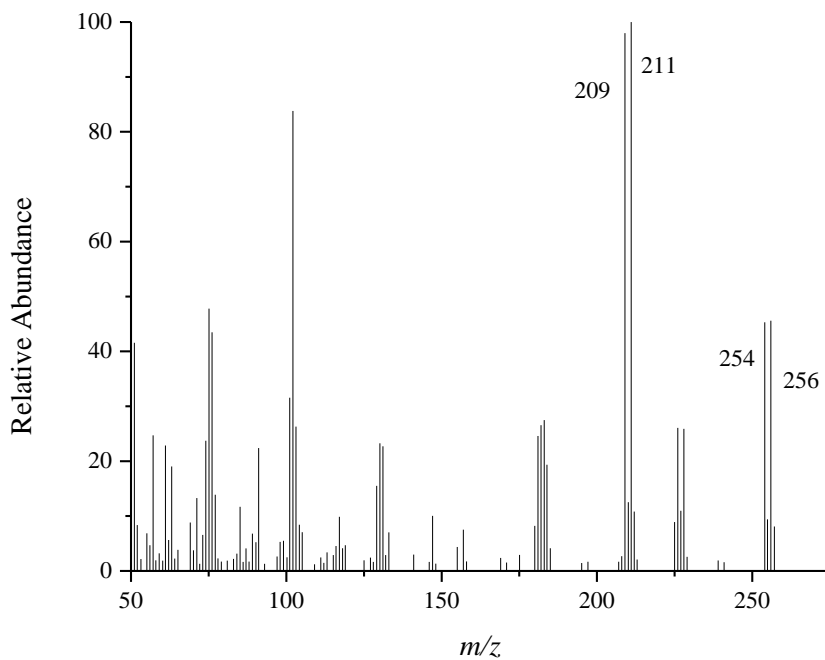


Figure S11. EI-MS of ethyl ester of (*E*)-*p*-Br-cinnamate biocatalyzed by N446K-*Os*TAM from (*2S*)- α -*p*-Br-phenylalanine.

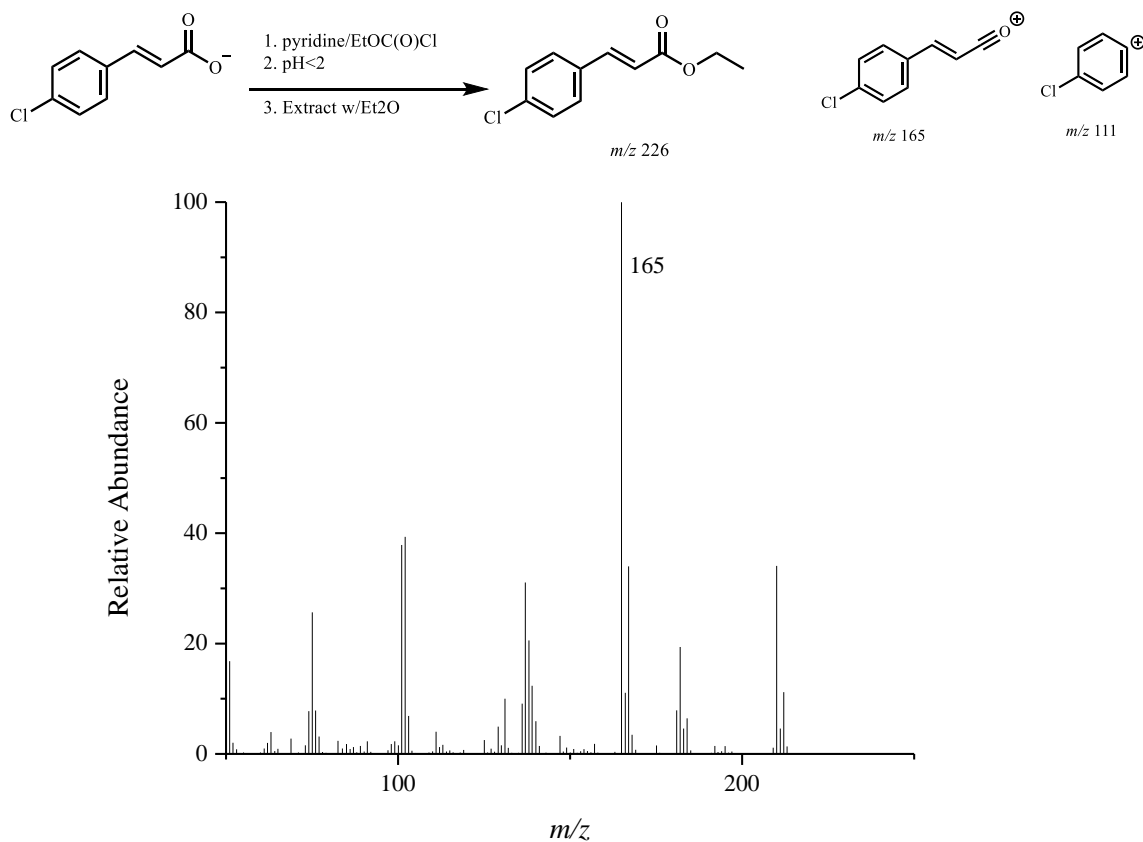


Figure S12. EI-MS of ethyl ester of authentic (*E*)-*p*-Cl-cinnamate.

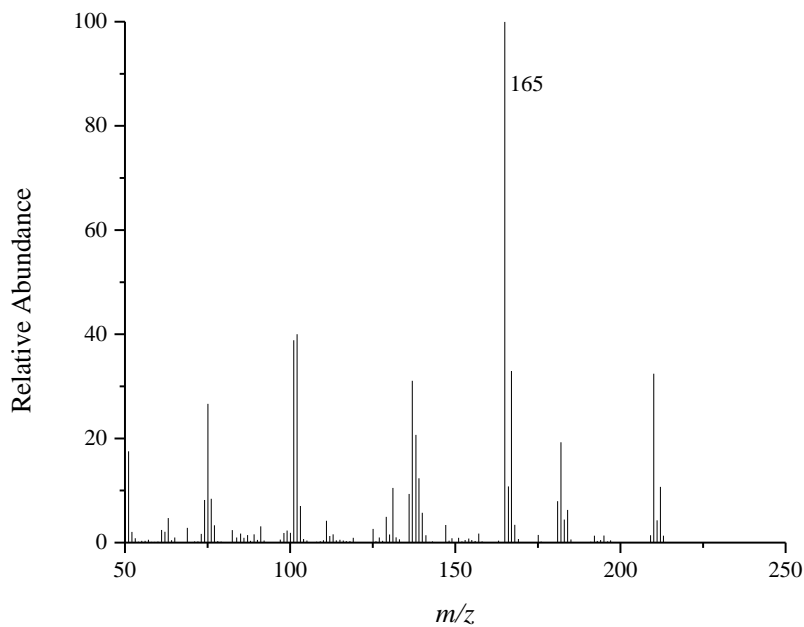


Figure S13. EI-MS of ethyl ester of (*E*)-*p*-Cl-cinnamate biocatalyzed by N446K-*O*_sTAM from (*2S*)- α -*p*-Cl-phenylalanine.

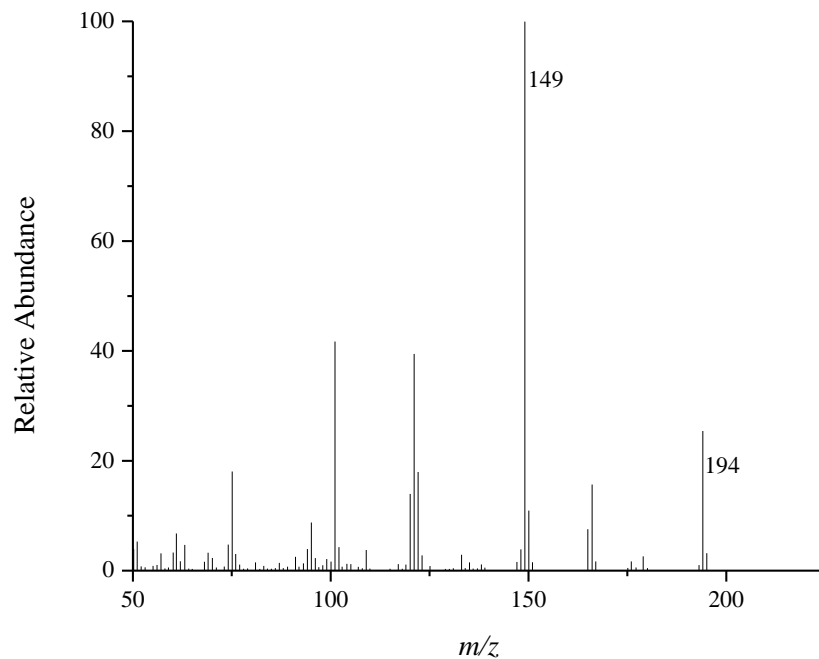
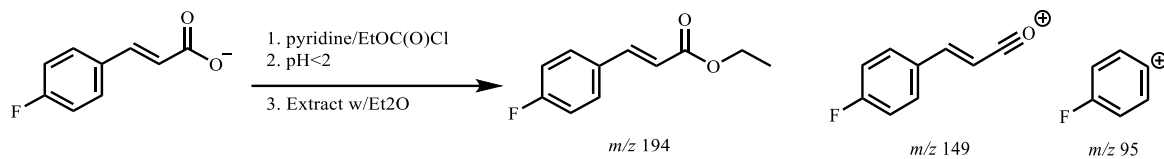


Figure S14. EI-MS of ethyl ester of authentic (*E*)-*p*-F-cinnamate.

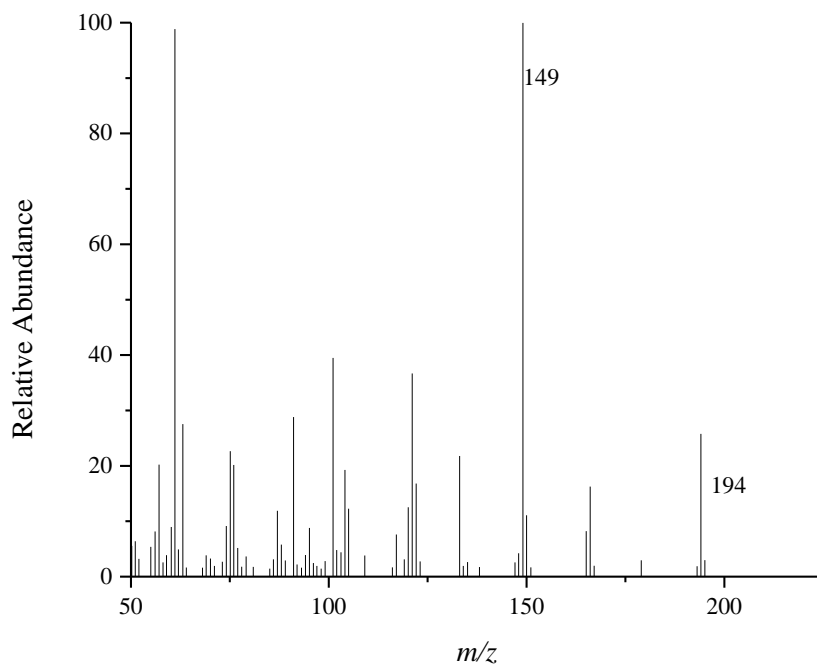


Figure S15. EI-MS of ethyl ester of (*E*)-*p*-F-cinnamate biocatalyzed by N446K-*O*_sTAM from (*2S*)- α -*p*-F-phenylalanine.

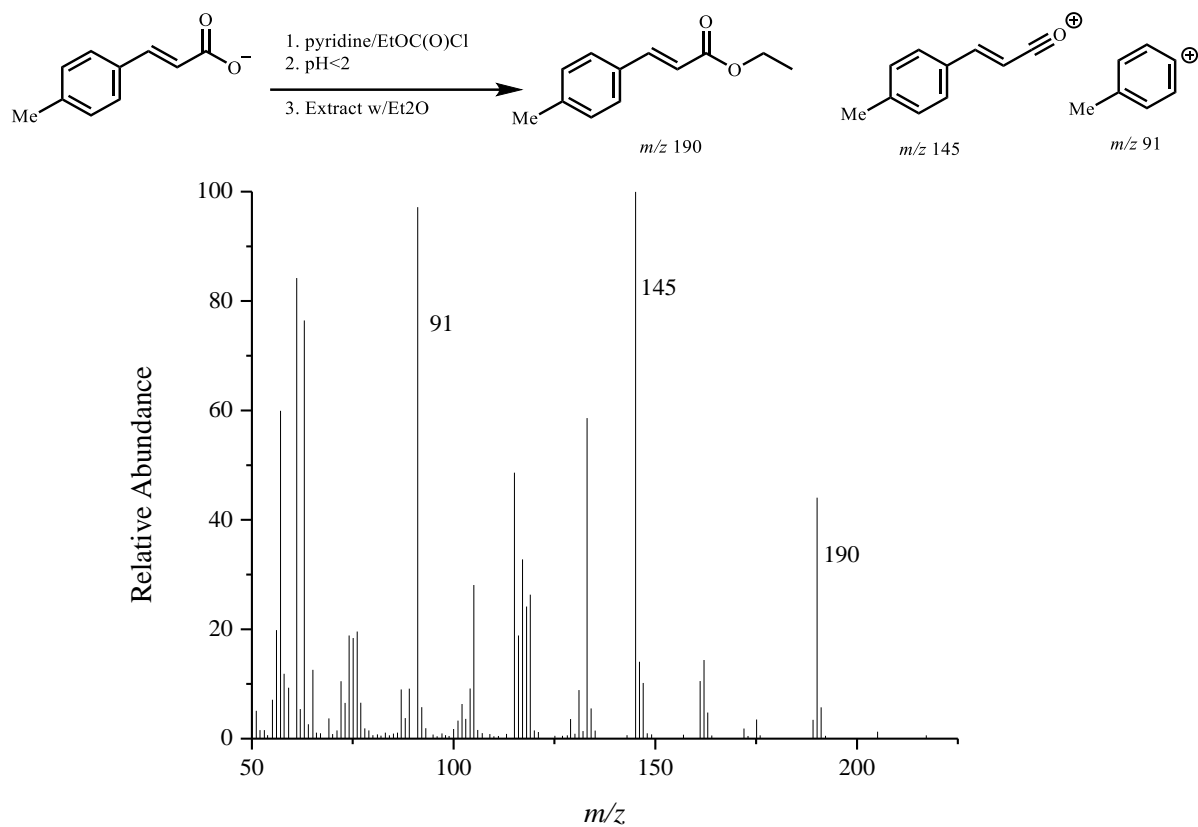


Figure S16. EI-MS of ethyl ester of authentic (*E*)-*p*-CH₃-cinnamate.

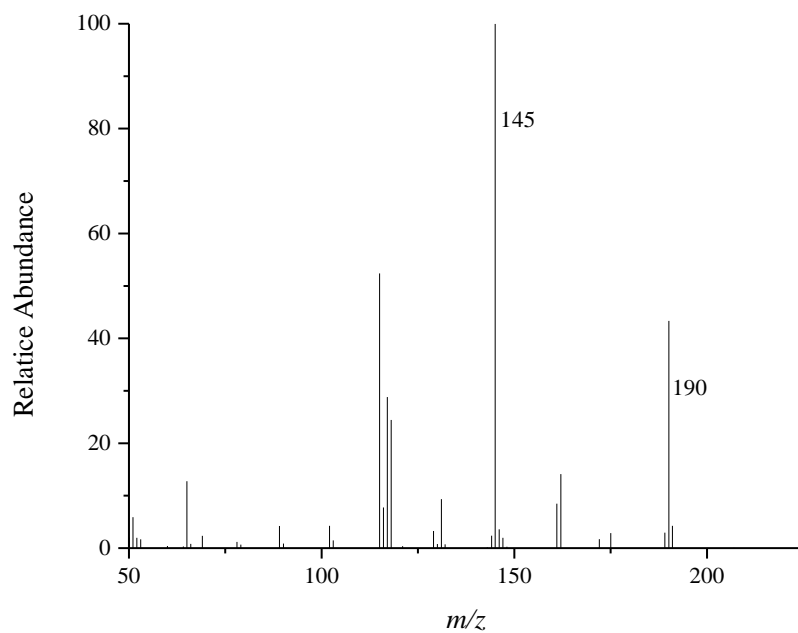


Figure S17. EI-MS of ethyl ester of (*E*)-*p*-CH₃-cinnamate biocatalyzed by N446K-*OsTAM* from (*2S*)- α -*p*-CH₃-phenylalanine.

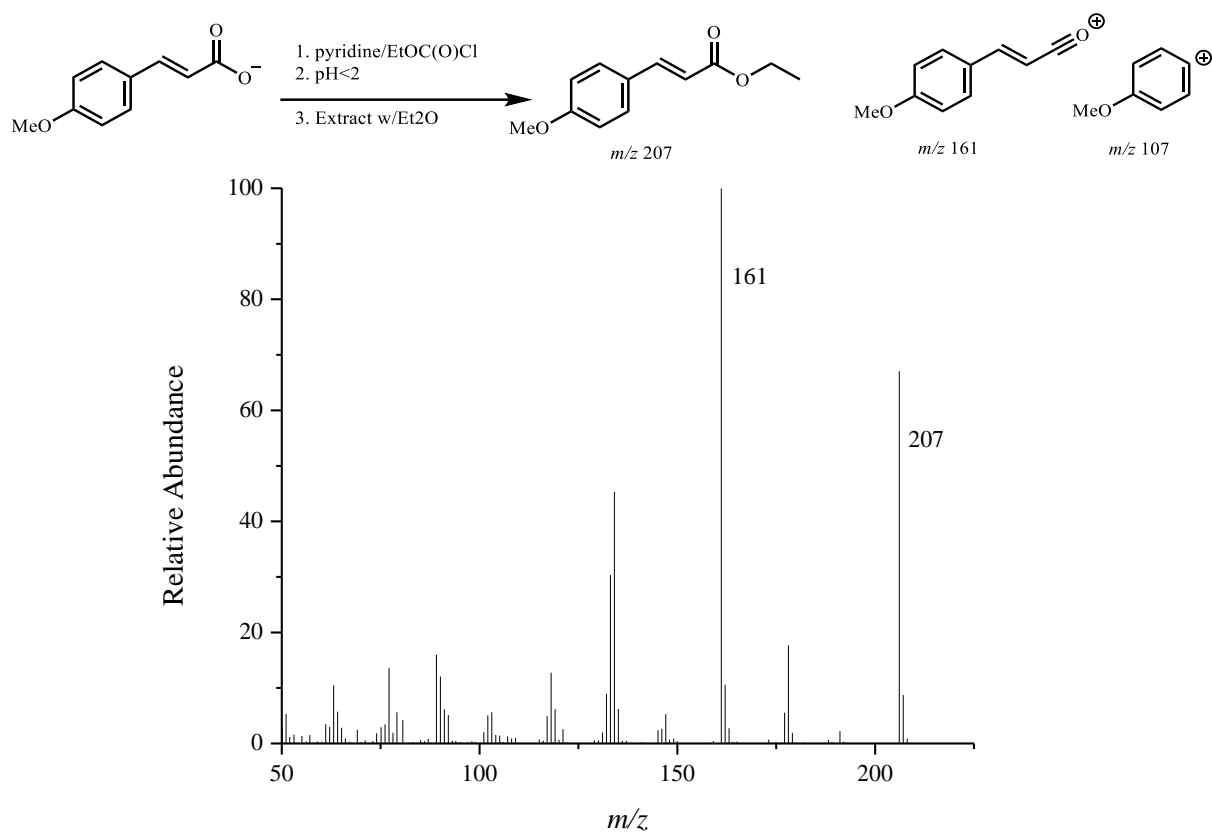


Figure S18. EI-MS of ethyl ester of authentic (*E*)-*p*-OCH₃-cinnamate.

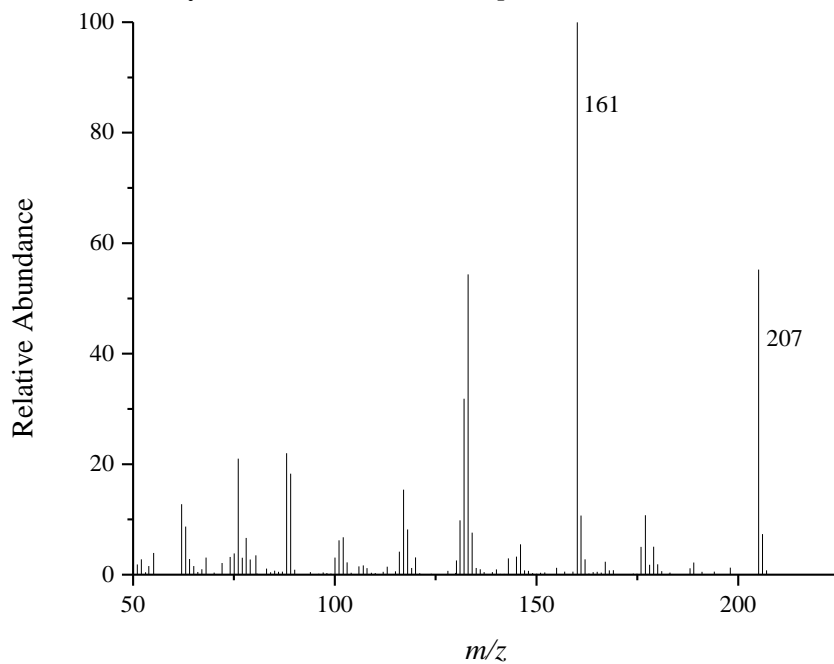


Figure S19. EI-MS of ethyl ester of (*E*)-*p*-OCH₃-cinnamate biocatalyzed by N446K-*O*_sTAM from (*2S*)- α -*p*-OCH₃ phenylalanine.

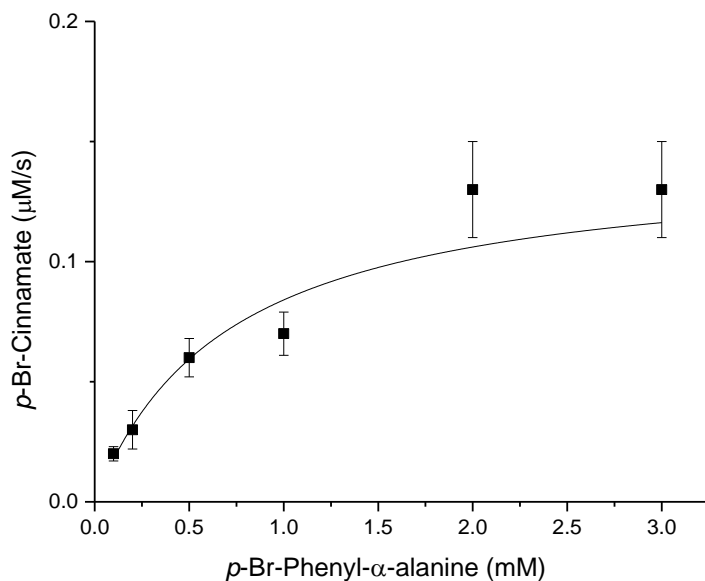


Figure S20. Michaelis-Menten kinetics plot for *p*-Br-cinnamic acid biocatalyzed by wild-type *OsTAM*. Standard error < 5%. $v = ([E] \times k_{cat} \times [S]) / (K_M + [S])$, where $K_M = 710 \mu\text{M}$, $k_{cat} = 0.014 \text{ s}^{-1}$.

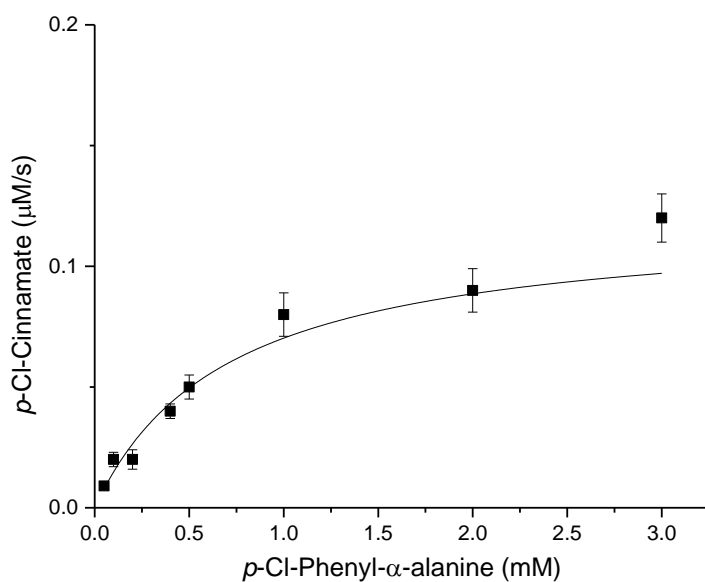


Figure S21. Michaelis-Menten kinetics plot for *p*-Cl-cinnamic acid biocatalyzed by wild-type *OsTAM*. Standard error < 5%. $v = ([E] \times k_{cat} \times [S]) / (K_M + [S])$, where $K_M = 708 \mu\text{M}$, $k_{cat} = 0.012 \text{ s}^{-1}$.

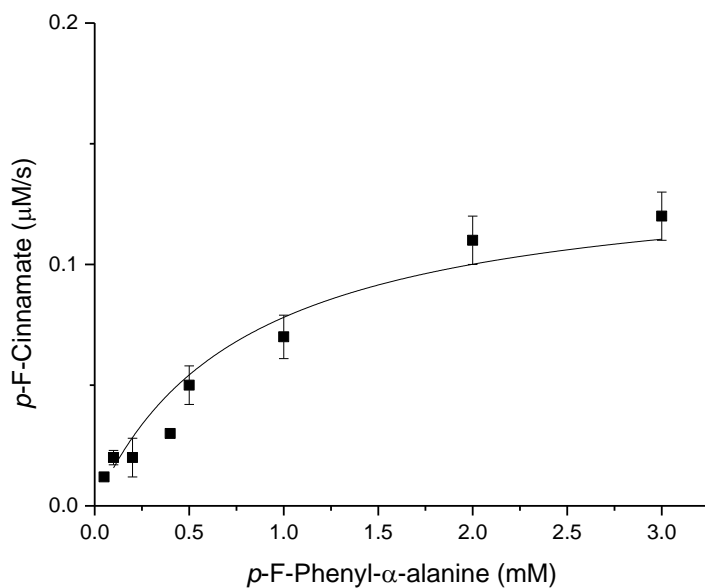


Figure S22. Michaelis-Menten kinetics plot for *p*-F-cinnamic acid biocatalyzed by wild-type *OsTAM*. Standard error < 5%. $v = ([E] \times k_{\text{cat}} \times [S]) / (K_M + [S])$, where $K_M = 713 \mu\text{M}$, $k_{\text{cat}} = 0.010 \text{ s}^{-1}$.

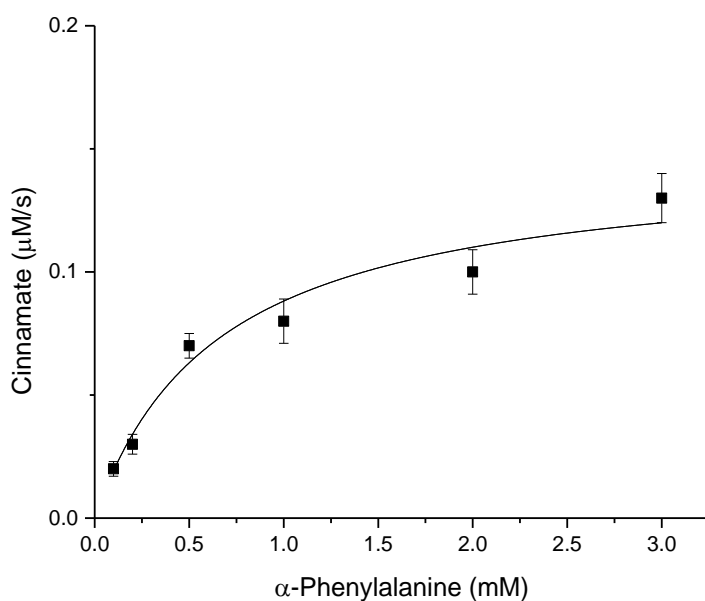


Figure S23. Michaelis-Menten kinetics plot for cinnamic acid biocatalyzed by wild-type *OsTAM*. Standard error < 5%. $v = ([E] \times k_{\text{cat}} \times [S]) / (K_M + [S])$, where $K_M = 660 \mu\text{M}$, $k_{\text{cat}} = 0.013 \text{ s}^{-1}$.

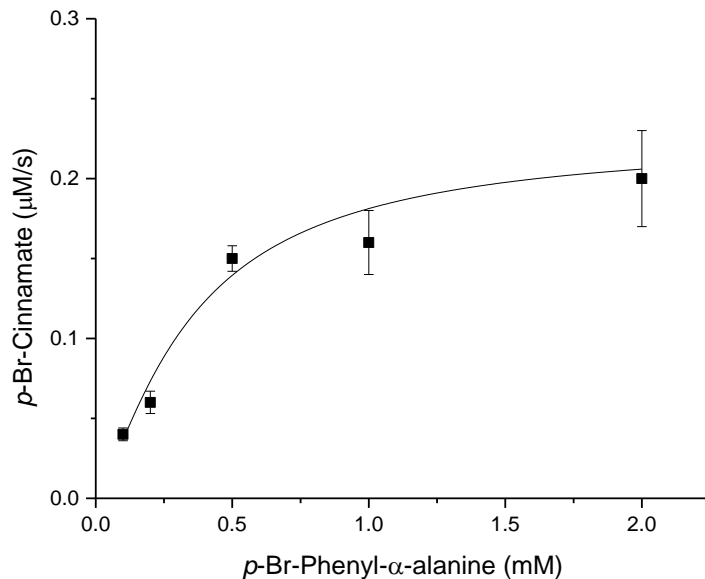


Figure S24. Michaelis-Menten kinetics plot for *p*-Br-cinnamic acid biocatalyzed by Y125C-*Os*TAM mutant. Standard error < 5%. $v = ([E] \times k_{cat} \times [S]) / (K_M + [S])$, where $K_M = 349 \mu\text{M}$, $k_{cat} = 0.021 \text{ s}^{-1}$.

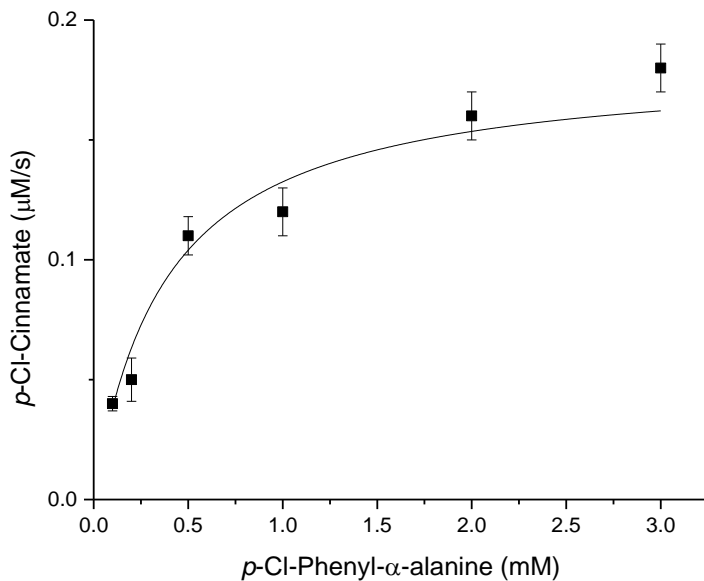


Figure S25. Michaelis-Menten kinetics plot for *p*-Cl-cinnamic acid biocatalyzed by Y125C-*Os*TAM mutant. Standard error < 5%. $v = ([E] \times k_{cat} \times [S]) / (K_M + [S])$, where $K_M = 377 \mu\text{M}$, $k_{cat} = 0.017 \text{ s}^{-1}$.

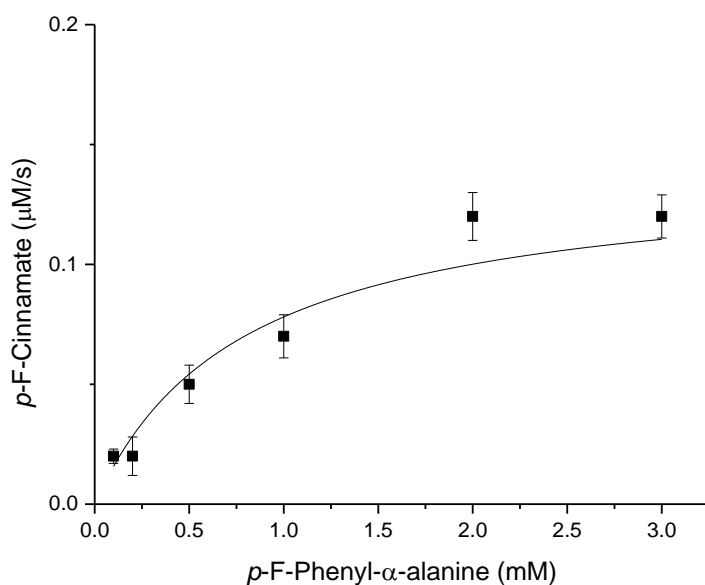


Figure S26. Michaelis-Menten kinetics plot for *p*-F-cinnamic acid biocatalyzed by Y125C-*Os*TAM mutant. Standard error < 5%. $v = ([E] \times k_{\text{cat}} \times [S]) / (K_M + [S])$, where $K_M = 785 \mu\text{M}$, $k_{\text{cat}} = 0.012 \text{ s}^{-1}$.

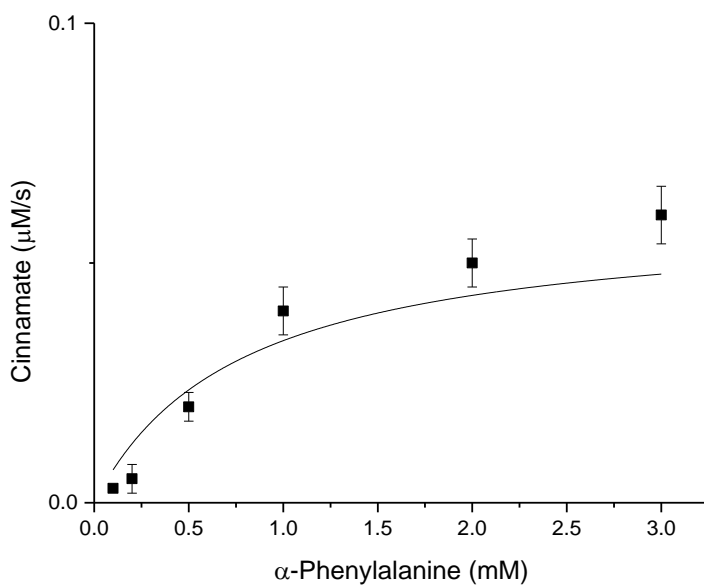


Figure S27. Michaelis-Menten kinetics plot for cinnamic acid biocatalyzed by Y125C-*Os*TAM. Standard error < 5%. $v = ([E] \times k_{\text{cat}} \times [S]) / (K_M + [S])$, where $K_M = 787 \mu\text{M}$, $k_{\text{cat}} = 0.006 \text{ s}^{-1}$.

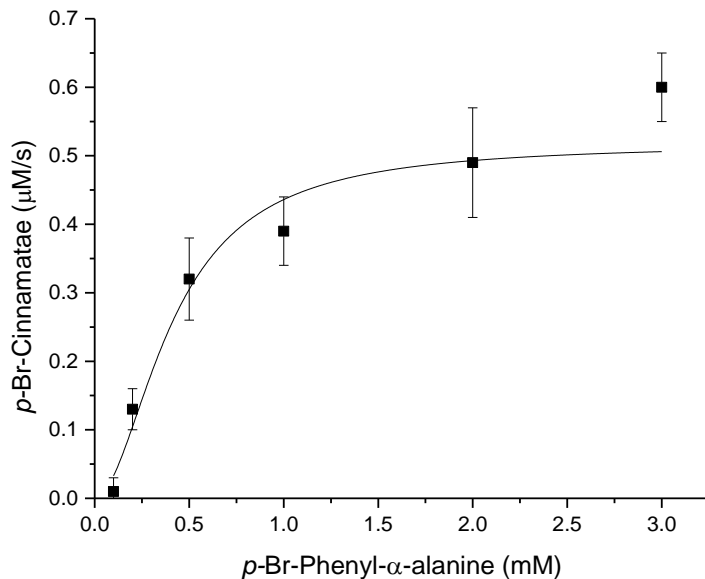


Figure S28. Michaelis-Menten kinetics plot for *p*-Br-cinnamic acid biocatalyzed by N446K-*O*sTAM mutant. Standard error < 5%. $v = ([E] \times k_{cat} \times [S]) / (K_M + [S])$, $K_M = 414 \mu\text{M}$, $k_{cat} = 0.048 \text{ s}^{-1}$.

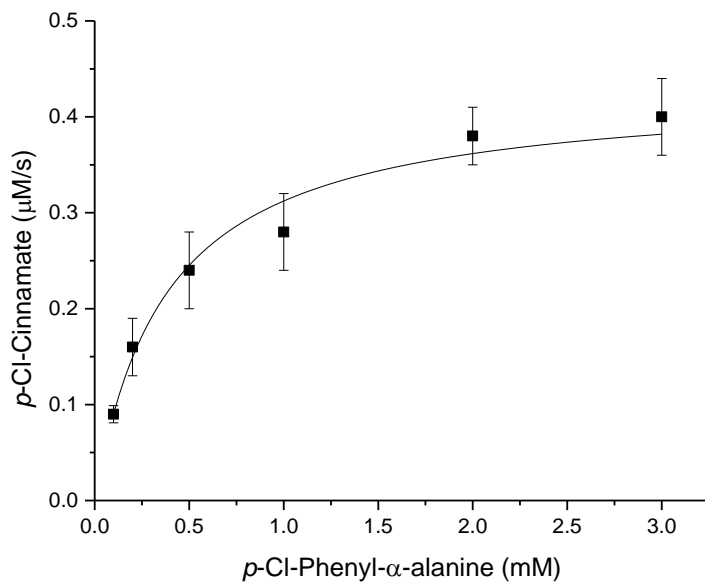


Figure S29. Michaelis-Menten kinetics plot for *p*-Cl-cinnamic acid biocatalyzed by N446K-*O*sTAM mutant. Standard error < 5%. $v = ([E] \times k_{cat} \times [S]) / (K_M + [S])$, where $K_M = 376 \mu\text{M}$, $k_{cat} = 0.040 \text{ s}^{-1}$.

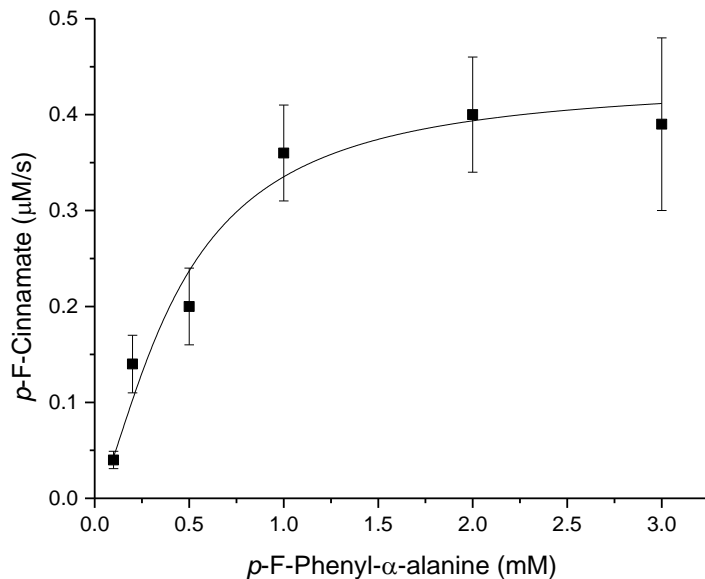


Figure S30. Michaelis-Menten kinetics plot for *p*-F-cinnamic acid biocatalyzed by N446K-*O*sTAM mutant. Standard error < 10%. $v = ([E] \times k_{cat} \times [S]) / (K_M + [S])$, where $K_M = 376 \mu\text{M}$, $k_{cat} = 0.040 \text{ s}^{-1}$.

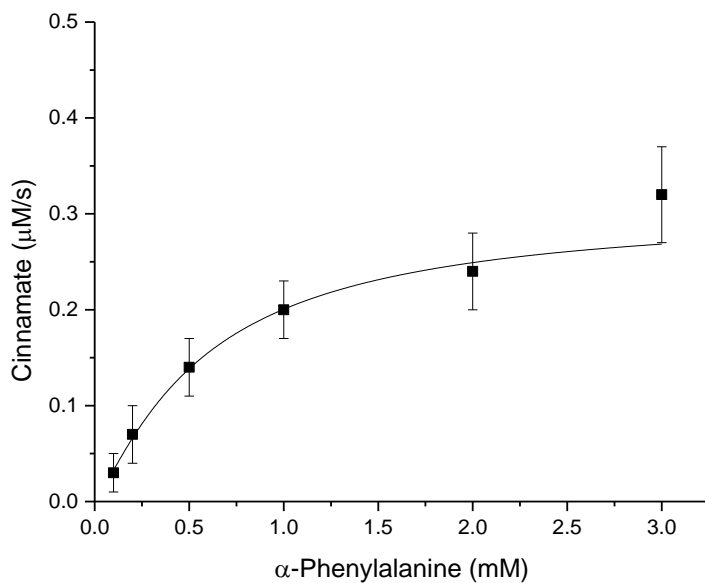


Figure S31. Michaelis-Menten kinetics plot for cinnamic acid biocatalyzed by N446K-*O*sTAM. Standard error < 5%. $v = ([E] \times k_{cat}) / (K_M + [S])$, where $K_M = 503 \mu\text{M}$, $k_{cat} = 0.033 \text{ s}^{-1}$.

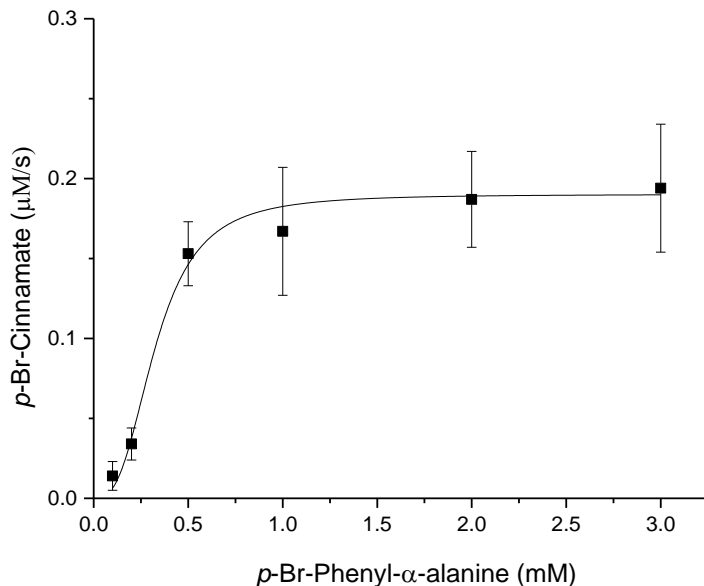


Figure S32. Michaelis-Menten kinetics plot for *p*-Br-cinnamic acid biocatalyzed by Y125C/N446K-*OsTAM* mutant. Standard error < 5%. $v = ([E] \times k_{\text{cat}} \times [S]) / (K_M + [S])$, where $K_M = 327 \mu\text{M}$, $k_{\text{cat}} = 0.018 \text{ s}^{-1}$.

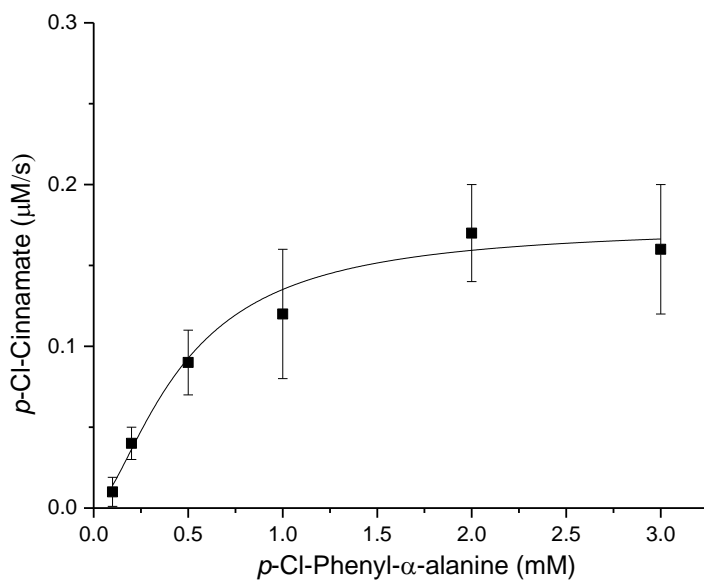


Figure S33. Michaelis-Menten kinetics plot for *p*-Cl-cinnamic acid biocatalyzed by Y125C/N446K-*OsTAM* mutant. Standard error < 10%. $v = ([E] \times k_{\text{cat}} \times [S]) / (K_M + [S])$, where $K_M = 463 \mu\text{M}$, $k_{\text{cat}} = 0.016 \text{ s}^{-1}$.

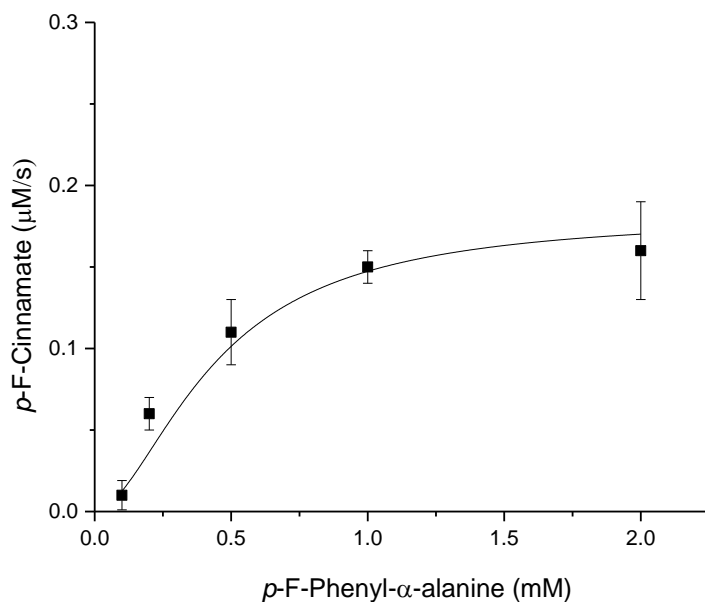


Figure S34. Michaelis-Menten kinetics plot for *p*-F-cinnamic acid biocatalyzed by Y125C/N446K-*OsTAM* mutant. Standard error < 5%. $v = ([E] \times k_{\text{cat}} \times [S]) / (K_M + [S])$, where $K_M = 439 \mu\text{M}$, $k_{\text{cat}} = 0.016 \text{ s}^{-1}$.

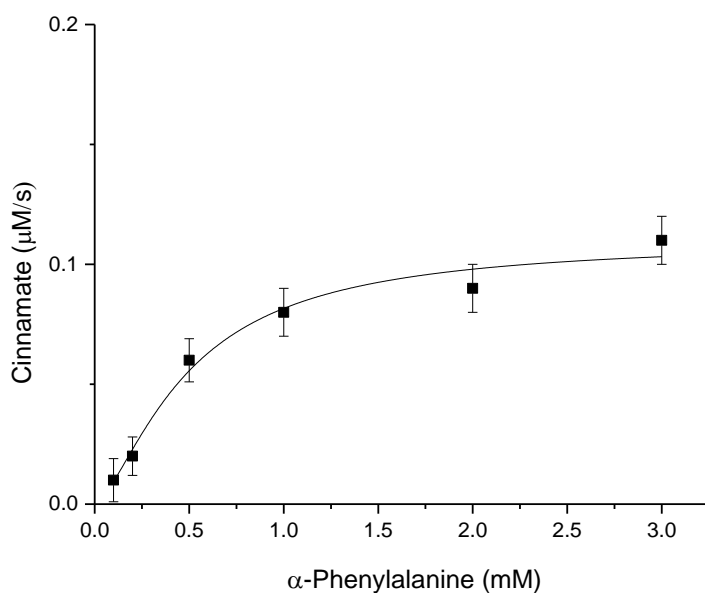


Figure S35. Michaelis-Menten kinetics plot for cinnamic acid biocatalyzed by Y125C/N446K-*OsTAM*. Standard error < 5%. $v = ([E] \times k_{\text{cat}} \times [S]) / (K_M + [S])$, where $K_M = 494 \mu\text{M}$, $k_{\text{cat}} = 0.011 \text{ s}^{-1}$.

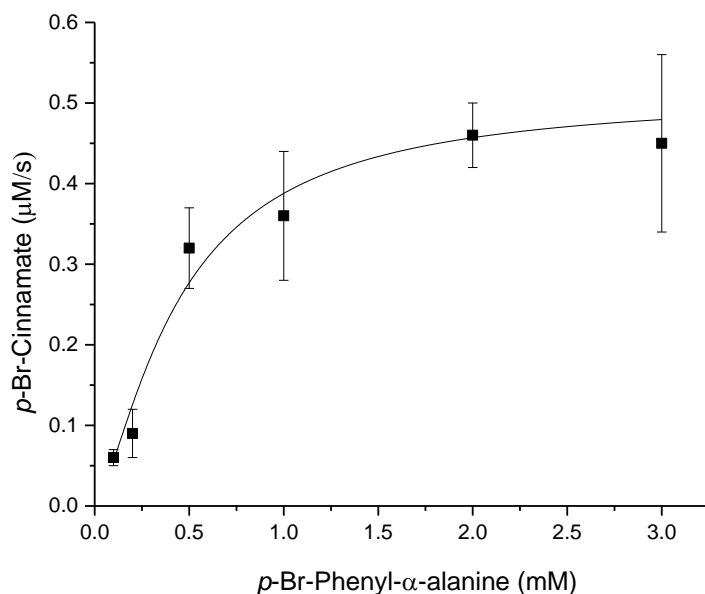


Figure S36. Michaelis-Menten kinetics plot for *p*-Br-cinnamic acid biocatalyzed by Y125C/N446K/T95A/T97I-*OsTAM* mutant. Standard error < 5%. $v = ([E] \times k_{\text{cat}} \times [S]) / (K_M + [S])$ $K_M = 445 \mu\text{M}$, $k_{\text{cat}} = 0.047 \text{ s}^{-1}$.

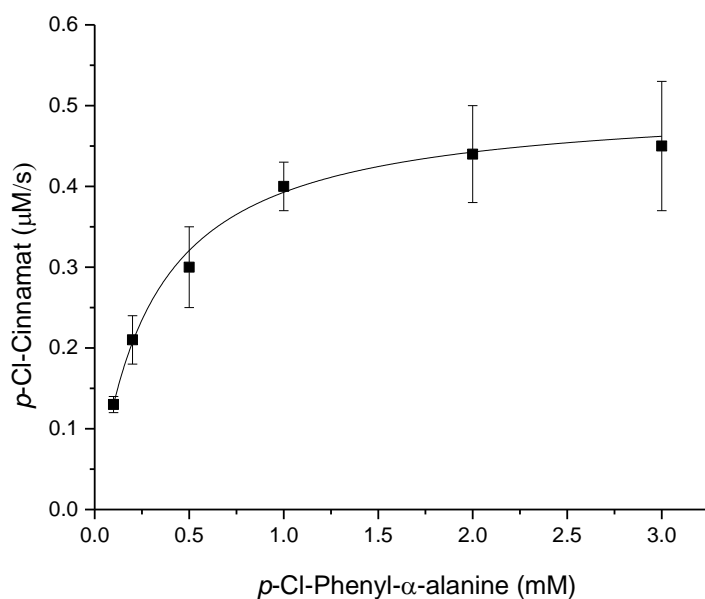


Figure S37. Michaelis-Menten kinetics plot for *p*-Cl-cinnamic acid biocatalyzed by Y125C/N446K/T95A/T97I-*OsTAM* mutant. Standard error < 5%. $v = ([E] \times k_{\text{cat}} \times [S]) / (K_M + [S])$, where $K_M = 290 \mu\text{M}$, $k_{\text{cat}} = 0.046 \text{ s}^{-1}$.

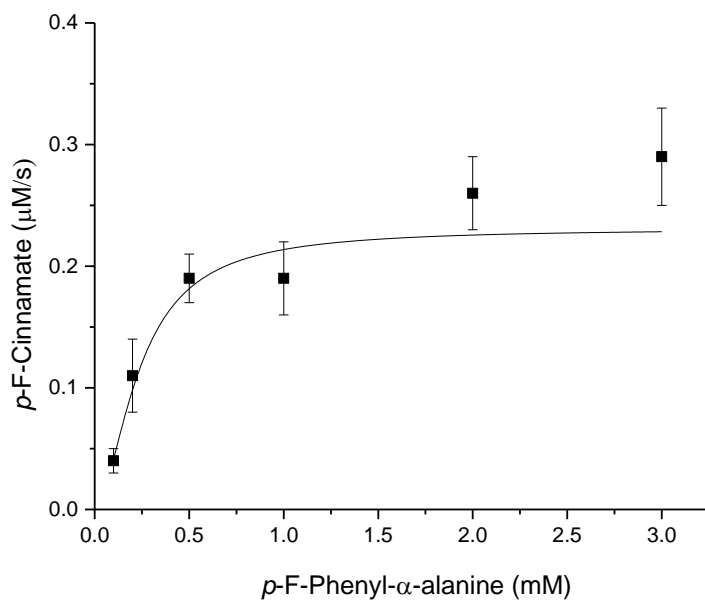


Figure S38. Michaelis-Menten kinetics plot for *p*-F-cinnamic acid biocatalyzed by Y125C/N446K/T95A/T97I-*OsTAM* mutant. Standard error < 5%. $v = ([E] \times k_{\text{cat}} \times [S]) / (K_M + [S])$, where $K_M = 238 \mu\text{M}$, $k_{\text{cat}} = 0.021 \text{ s}^{-1}$.

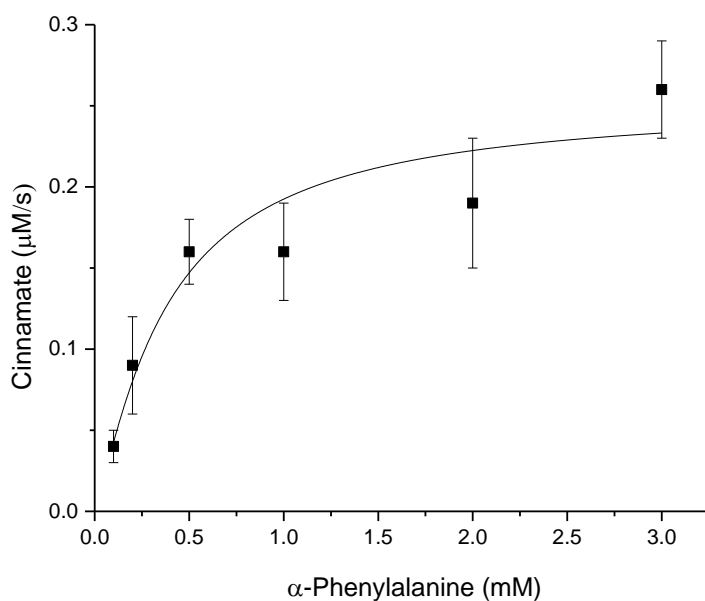


Figure S39. Michaelis-Menten kinetics plot for cinnamic acid biocatalyzed by Y125C/N446K/T95A/T97I-*OsTAM* mutant. Standard error < 10%. $v = ([E] \times k_{\text{cat}} \times [S]) / (K_M + [S])$, where $K_M = 379 \mu\text{M}$, $k_{\text{cat}} = 0.023 \text{ s}^{-1}$.

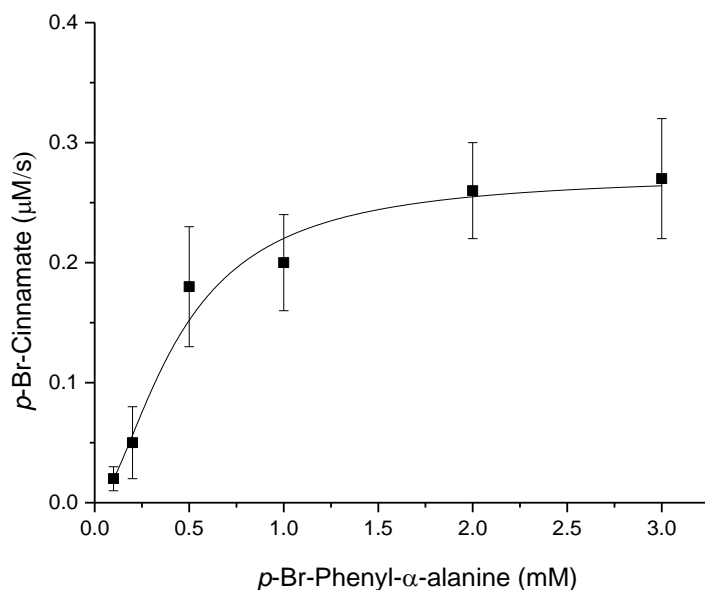


Figure S40. Michaelis-Menten kinetics plot for *p*-Br-cinnamic acid biocatalyzed by T95A/T97I-*O*sTAM mutant. Standard error < 5%. $v = ([E] \times k_{\text{cat}} \times [S]) / (K_M + [S])$, where $K_M = 439 \mu\text{M}$, $k_{\text{cat}} = 0.025 \text{ s}^{-1}$.

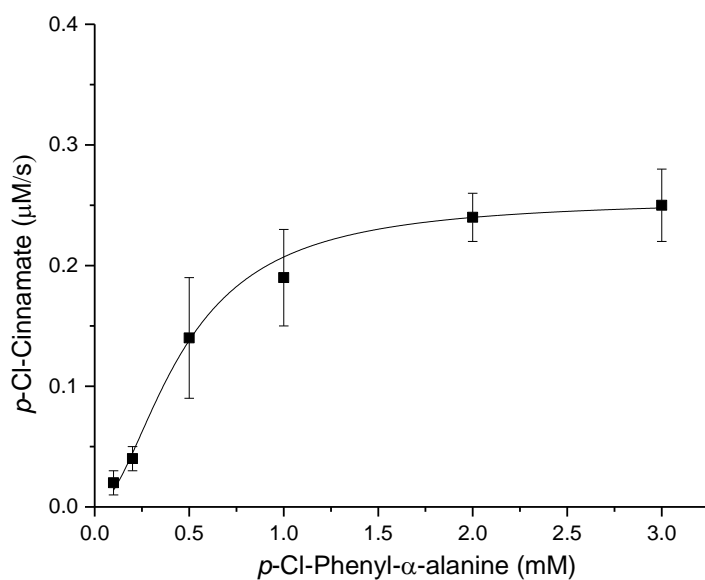


Figure S41. Michaelis-Menten kinetics plot for *p*-Cl-cinnamic acid biocatalyzed by T95A/T97I-*O*sTAM mutant. Standard error < 5%. $v = ([E] \times k_{\text{cat}} \times [S]) / (K_M + [S])$, where $K_M = 458 \mu\text{M}$, $k_{\text{cat}} = 0.023 \text{ s}^{-1}$.

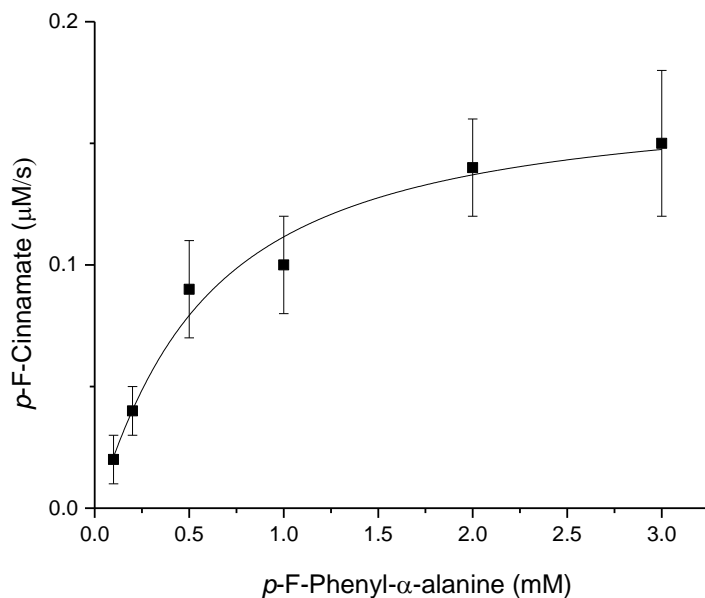


Figure S42. Michaelis-Menten kinetics plot for *p*-F-cinnamic acid biocatalyzed by T95A/T97I-*O*sTAM mutant. Standard error < 5%. $v = ([E] \times k_{\text{cat}} \times [S]) / (K_M + [S])$, where $K_M = 562 \mu\text{M}$, $k_{\text{cat}} = 0.015 \text{ s}^{-1}$.

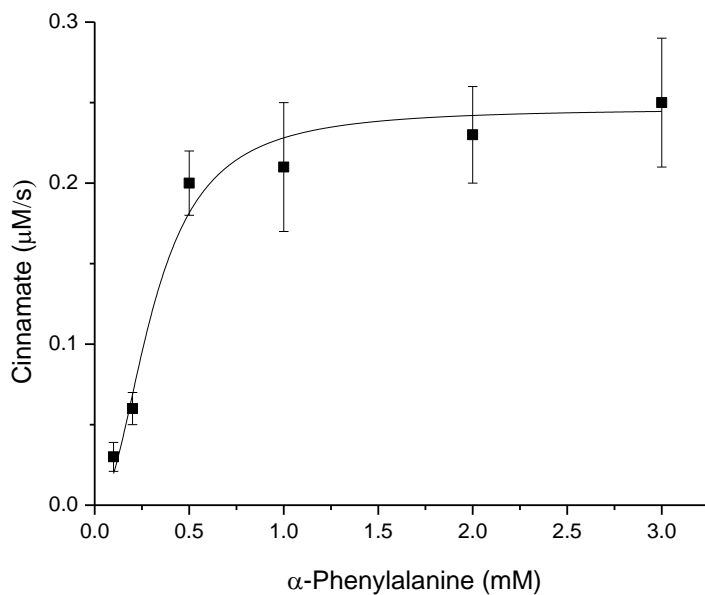


Figure S43. Michaelis-Menten kinetics plot for cinnamic acid biocatalyzed by T95A/T97I-*O*sTAM mutant. Standard error < 5%. $v = ([E] \times k_{\text{cat}} \times [S]) / (K_M + [S])$, where $K_M = 311 \mu\text{M}$, $k_{\text{cat}} = 0.022 \text{ s}^{-1}$.

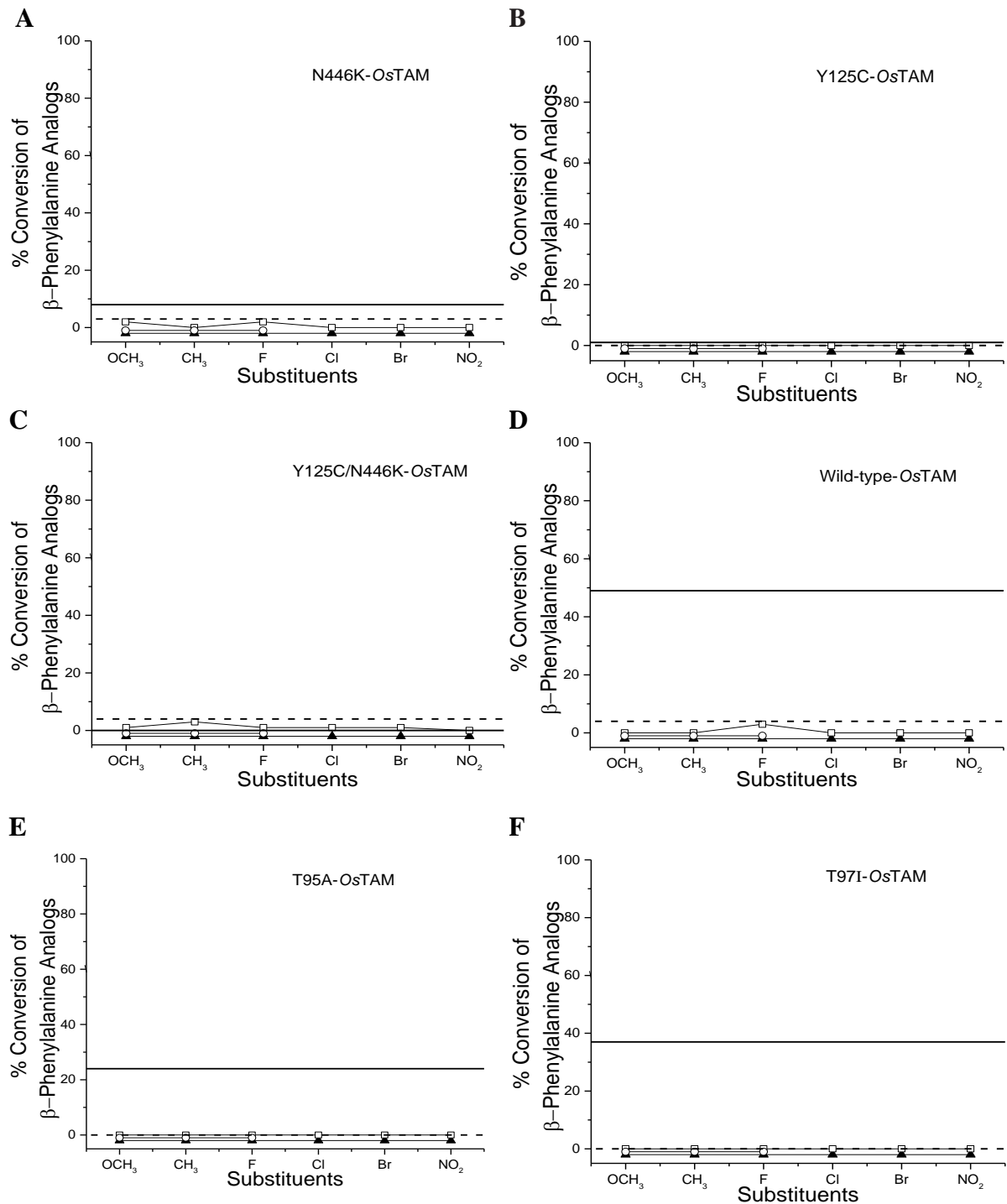


Figure S44. Percent conversion of β -phenylalanine analogs for A) N446K-*OsTAM*, B) Y125C-*OsTAM*, C) Y125C/N446K-*OsTAM* D) wild type-*OsTAM* E) T95A-*OsTAM*, and F) T97I-*OsTAM* were incubated with *para*-(\square), *meta*-(\blacktriangle), and *ortho*-(\circ)-substituted α -phenylalanines. The dotted line represents the percent yield β -phenylalanine analogs, and the solid line shows the percent yield of β -tyrosine. Standard error = $\pm 5\%$; n = 3.

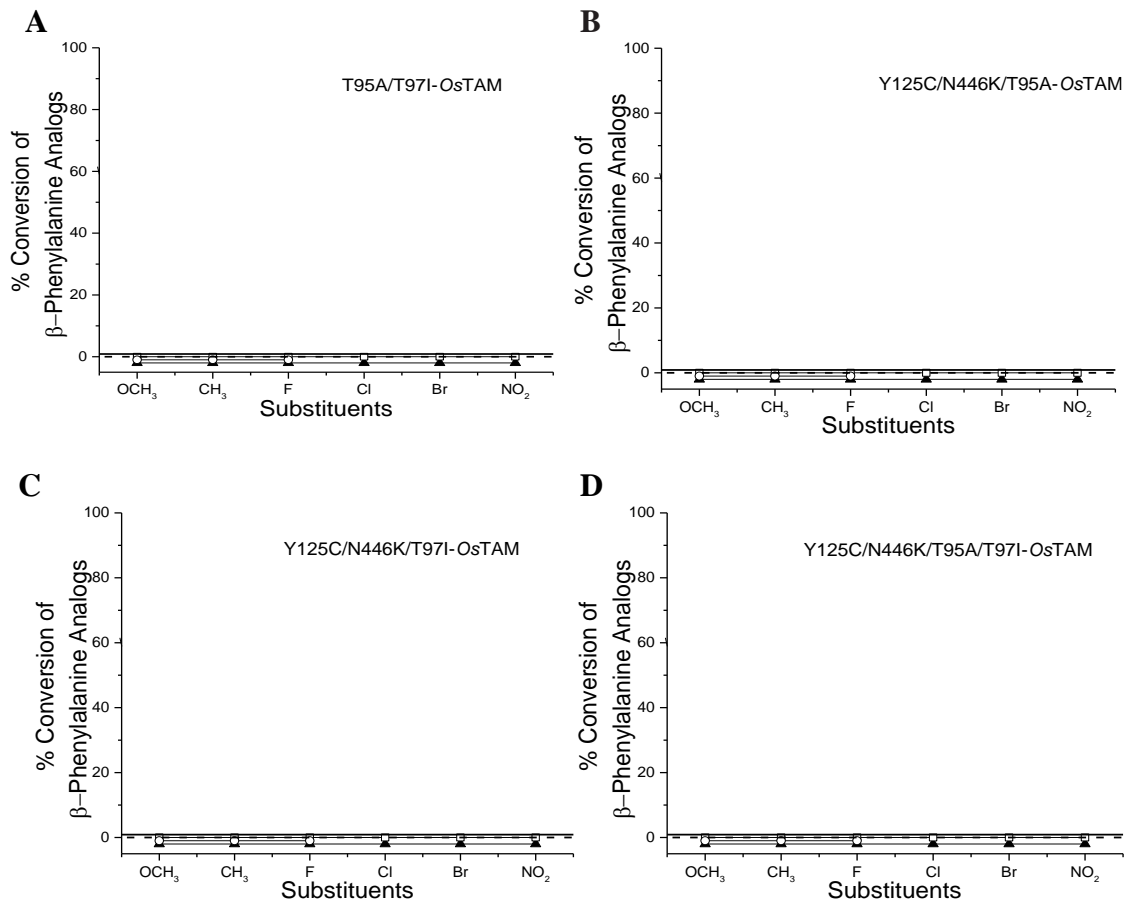


Figure S45. Percent conversion of β -phenylalanine analogs for A) T95A/T97I-OsTAM, B) Y125C/N446K/T95A-OsTAM, C) Y125C/N446K/T97I-OsTAM, and D) Y125C/N446K/T95A/T97I-OsTAM were incubated with *para*-(\square), *meta*-(\blacktriangle), and *ortho*-(\circ)-substituted α -phenylalanines. The dotted line represents the percent yield β -phenylalanine analogs, and the solid line shows the percent yield of β -tyrosine. Standard error = $\pm 5\%$; $n = 3$.

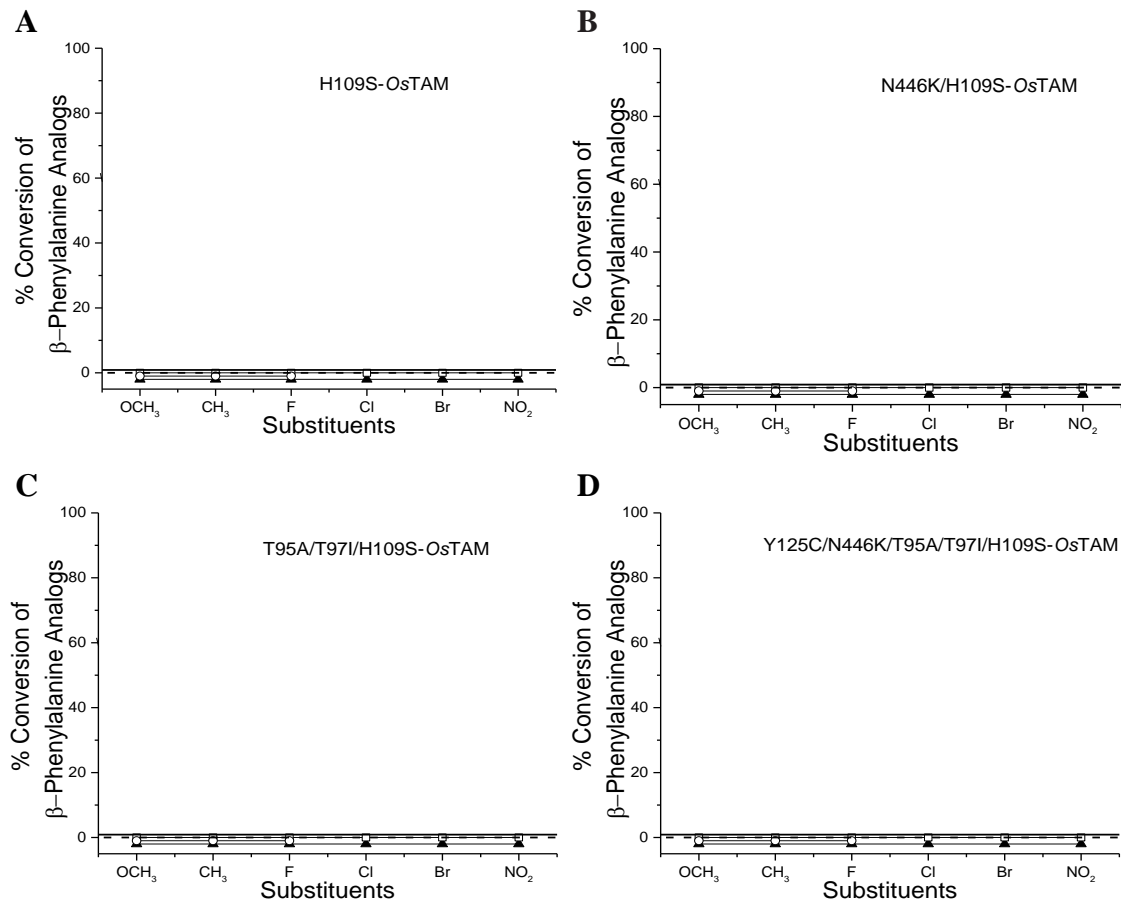


Figure S46. Percent conversion of β -phenylalanine analogs for A) H109S-OsTAM, B) N446K/H109S-OsTAM, C) T95A/T95I/H109S-OsTAM, and D) Y125C/N446K/T95A/T97I/H109S-OsTAM were incubated with *para*-(\square), *meta*-(\blacktriangle), and *ortho*-(\circ)-substituted α -phenylalanines. The dotted line represents the percent yield β -phenylalanine analogs, and the solid line shows the percent yield of β -tyrosine. Standard error = $\pm 5\%$; $n = 3$.

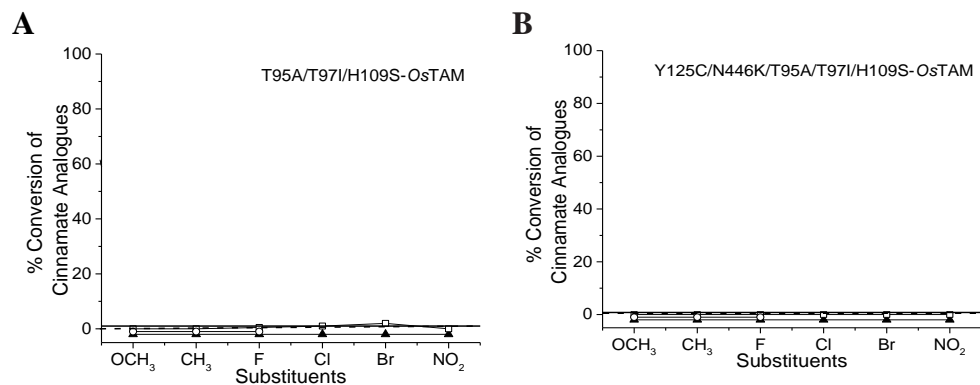


Figure S47. The percent yield of *trans*-cinnamate analogs made biocatalytically from A) H109S-*OsTAM*, B) N446K/H109S-*OsTAM*, C) T95A/T97I/H109S-*OsTAM*, D) Y125C/N446K/T95A/T97I/H109S-*OsTAM*, E) F115L-*OsTAM*, and F) N446K/F115L-*OsTAM* incubated with *p*-(\square), *m*-(\blacktriangle), and *o*-(\circ)-substituted α -phenylalanines. The dashed line shows the percent yield of cinnamic acid from phenylalanine, and the solid line shows the percent yield of coumaric acid from tyrosine. Standard error = $\pm 5\%$; $n = 3$.

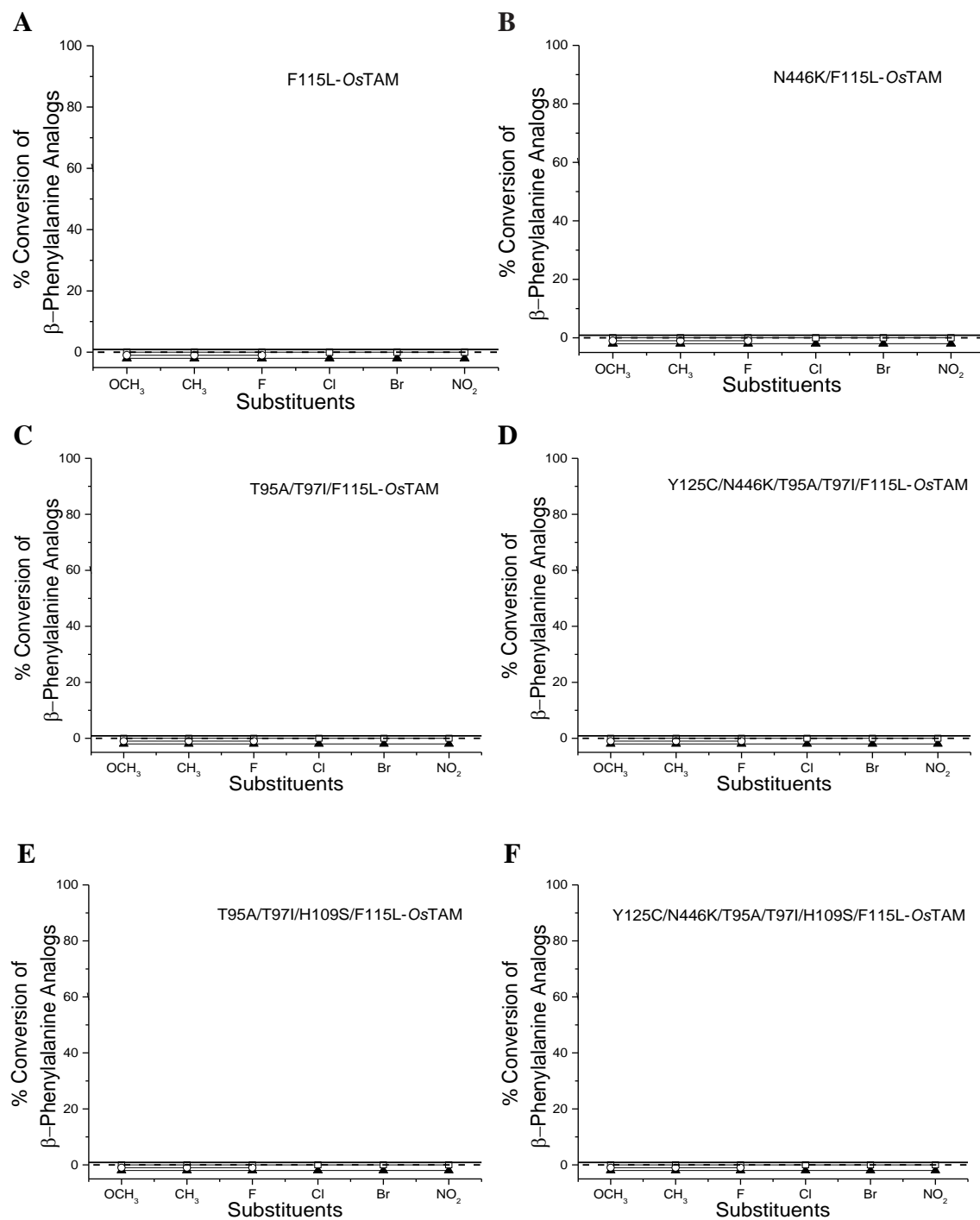


Figure S48. Percent conversion of β -phenylalanine analogs made biocatalytically from A) F115L-OsTAM, B) N446K/F115L-OsTAM, C) T95A/T97I/F115L-OsTAM D) Y125C/N446K/T95A/T97I/F115L-OsTAM E) T95A/T97I/H109S/F115L-OsTAM, and F) Y125C/N446K/T95A/T97I/H109S/F115L-OsTAM were incubated with *para*-(\square), *meta*-(\blacktriangle), and *ortho*-(\circ)-substituted α -phenylalanines. The dotted line represents the percent yield β -phenylalanine analogs, and the solid line shows the percent yield of β -tyrosine. Standard error = $\pm 5\%$; n = 3.

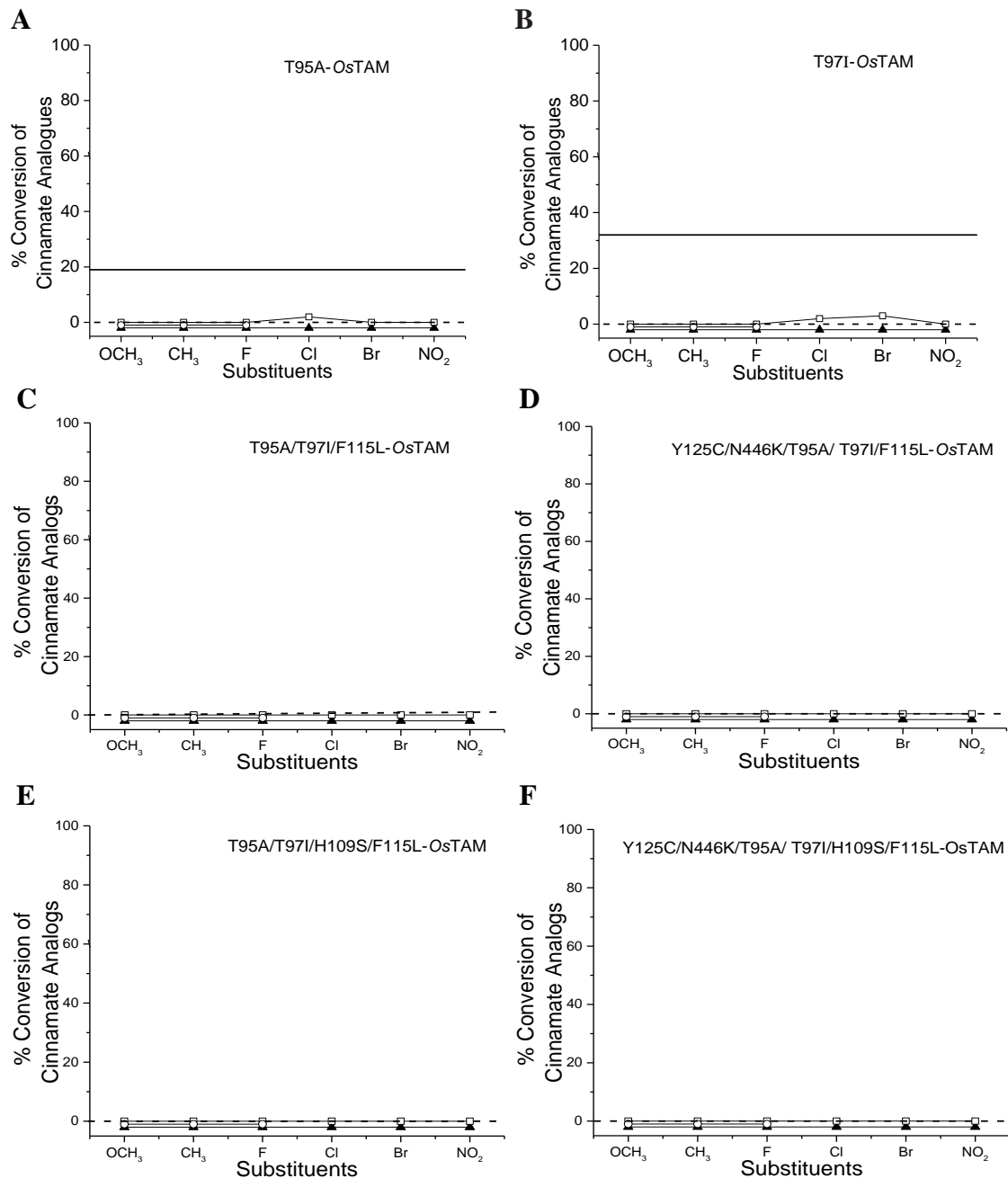


Figure S49. The percent yield of *trans*-cinnamate analogs made biocatalytically from A) T95A-OsTAM, B) T97I-OsTAM, C) T95A/T97I/F115L-OsTAM, D) Y125C/N446K/T95A/T97I/F115L-OsTAM, E) T95A/T97I/H109S/F115L-OsTAM, and F) Y125C/N446K/T95A/T97I/H109S/F115L-OsTAM were incubated with *para*-(□), *meta*-(▲), and *ortho*-(○)-substituted α -phenylalanines. The dashed line shows the percent yield of cinnamic acid from phenylalanine, and the solid line shows the percent yield of coumaric acid from tyrosine. Standard error = \pm 5%; n = 3.

REFERENCES

REFERENCES

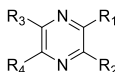
1. Heberling, M. M.; Masman, M. F.; Bartsch, S.; Wybenga, G. G.; Dijkstra, B. W.; Marrink, S. J.; Janssen, D. B., Ironing Out their Differences: Dissecting the Structural Determinants of a Phenylalanine Aminomutase and Ammonia lyase. *ACS chemical biology* **2015**, *10* (4), 989-997.
2. Bartsch, S.; Wybenga, G. G.; Jansen, M.; Heberling, M. M.; Wu, B.; Dijkstra, B. W.; Janssen, D. B., Redesign of a Phenylalanine Aminomutase into a Phenylalanine Ammonia Lyase. *ChemCatChem* **2013**, *5* (7), 1797-1802.
3. Walter, T.; King, Z.; Walker, K. D., A Tyrosine Aminomutase from Rice (*Oryza sativa*) Isomerizes (*S*)- α -to (*R*)- β -tyrosine with Unique High Enantioselectivity and Retention of Configuration. *Biochemistry* **2015**, *55* (1), 1-4.
4. Hansch, C.; Leo, A.; Taft, R., A Survey of Hammett Substituent Constants and Resonance and Field Parameters. *Chemical Reviews* **1991**, *91* (2), 165-195.
5. Hamano, H.; Hamaka, H., On the Dipole Moments and Chemical Properties of Pyrazole and Imidazole. *Tetrahedron* **1962**, *18* (8), 985-990.
6. Rankin, D. W., CRC Handbook of Chemistry and Physics, edited by David R. Lide. Taylor & Francis: 2009.

Chapter 4 . Developing a Coupling Reaction Toward Regioselectively Enriched Ethyl Dimethyl Pyrazine Isomers via Semibiocatalysis.

4.1 Introduction

4.1.1 Pyrazines in Food Chemistry.

Alkylpyrazines (AlkPyr), acylpyrazines (AcylPyr), and alkyl/alkoxy pyrazines (Alk/AlkO-Pyr) are six-member heterocyclic aromatic compounds alkylated, acylated, and alkoxyated at various positions on the ring (Figure 4.1). These 1,4-diazine compounds are distributed in nature and have been widely studied,¹⁻⁴ isolated and characterized from plants,⁵ insects,^{6,7} fermentation broth,⁸ coffee, roasted nuts, cereals, meat products, and wine.⁹⁻¹³ AlkPyr and Alk/AlkO-Pyr are used to flavor chocolate, roasted nuts, and meat because of their aromas perceived as, for example, coffee, nutty, roasted, earthy, roasted cocoa, beef-like, and woody.¹⁴ AlkPyr are principally formed during the thermal processing of foodstuff,^{4,14,15} similar to the Maillard reaction,^{16,17} where a diketo compound and amino acid condense to form imine intermediates.



Mono-, Di-, Tri, and Tetra-Alkylpyrazines

R₁=CH₃, R₂/R₃/R₄=H; Methylpyrazine (MP)

R₁,R₂=CH₃, R₃,R₄= H; 2,3-Dimethylpyrazine (23-DMP)

R₁/R₄=H, R₂/R₃=CH₃; 2,5-Dimethylpyrazine (25-DMP)

R₁, R₃=CH₃, R₂/R₄=H; 2,6-Dimethylpyrazine (26-DMP)

R₁=Ethyl, R₂=CH₃, R₃/R₄=H; 2-Ethyl-3-methylpyrazine (2-E-3MP)

R₁/R₂/R₃=CH₃, R₄=H; 2,3,6-Trimethylpyrazine (236-TMP)

R₁/R₃=CH₃, R₂=Ethyl, R₄=H; 2-Ethyl-3,5-dimethylpyrazine (235-EDMP)

R₁=Ethyl, R₂/R₃= CH₃, R₄=H; 3-Ethyl-2,5-dimethylpyrazine (325-EDMP)

R₁/R₂/R₃/R₄=CH₃; 2,3,5,6-Tetramethylpyrazine (236-TetMP)

Acylpyrazines (AcylPyr)

R₁=Acetyl, R₂/R₃/R₄=H; Acetylpyrazine (AcP)

2-acetyl-6-methylpyrazine

Alkyl/Alkoxy pyrazines (Alk/AlkO-Pyr)

Isopropyl R₂=OCH₃, R₃/R₄=H; 2-Alkyl-3-methoxy pyrazines

Isobutyl

R₁=
sec-Butyl

Ethyl

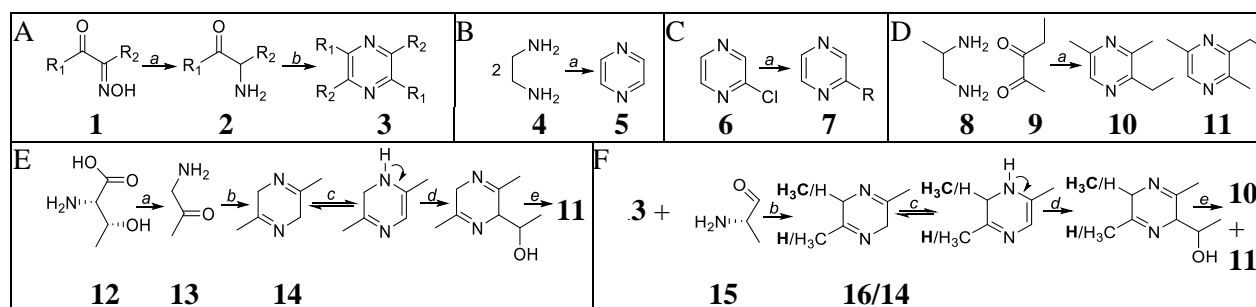
Figure 4.1. Important alkylpyrazines (AlkPyr), Acylpyrazines (AcylPyr), and alkyl/alkoxy pyrazines (Alk/AlkO-Pyr) in food chemistry.

4.1.2 Developed Synthetic Routes for Alk Pyrazines.

The growing demand for AlkPyrs and Alk/AlkO-Pyrs as additives or ingredients is limited by the low occurrence of pyrazines in plants or animal sources, such as 0.003 – 0.2 µg/100 g in various cocoa bean varieties.¹⁸ Generally, to solve this supply limitation, the industry looks to organic synthesis to address production bottlenecks. The first pyrazine synthesis of 2,3,5,6-tetraphenylpyrazine in 1897 involved self-condensation of 2-(benzylideneamino)-2-phenylacetonitrile.¹⁹ Another early method of synthesizing pyrazine isomers was discovered fortuitously when nitrosated ketones (**1**) were reduced to an aminoketone (**2**) with hydrogen. This synthesis demonstrated the intermediate formation of dihydropyrazines by isolating them under anaerobic conditions and subsequent oxidation to the corresponding tetralkylpyrazines (**3**) (Scheme 4.1A).²⁰ One more approach to pyrazine (**5**) started with the deaminocyclisation of ethylenediamine (**4**), followed by dehydrogenation over copper chromite catalysts (Scheme 4.1B).²¹ Later, microwave irradiation was used to form substituted pyrazines by coupling 2-chloropyrazine (**6**) with nucleophiles of PhSNa, MeSNa, EtONa, and PhONa in *N*-methylpyrrolidone (NMP) that gave the desired monothioether/ether products (**7**) (Scheme 4.1C).²²

Access to alkylpyrazines from the pyrazine core has been done with alkyllithium. However, one example demonstrated a downside to this approach using methylpyrazines where the alkyllithium either alkylated the pyrazine ring, the methyl group of methylpyrazine, or both, leading to undesired, low yielding product mixtures.²³ Another alkylpyrazine, 2-alkyl-3,6-dimethylpyrazine, was made by thermal electrocyclozation or zirconium-mediated alkenylation of 2,5-dimethylpyrazine with acetylenes. However, this method was of little practical value because the requisite zirconium catalyst is extremely air-sensitive, and the preparation of the cationic complex needs expensive inert atmosphere equipment.²⁴

Today, pyrazines are assembled synthetically by condensation between dicarbonyl and diamino compounds (Scheme 4.1D) or biosynthetically between self-condensation of an aminocarbonyl (**2**) followed by oxidation on the proposed biosynthetic pathway to 325-EDMP (**11**) in *Serratia marcescens* (Scheme 4.1E).^{25,26} Symmetry in one reagent in the condensation reaction gives the best isomeric selectivity in the product en route to pyrazines.²⁵ Several variations of the condensation reactions have been developed by adding metal catalysts and making solvent alterations. However, the main drawbacks of the synthetic approaches are low yields, prolonged reaction time, toxic solvents and metals, and complicated separation techniques to isolate the products.²⁵



Scheme 4.1. A) a) H_2 , b) dehydration/oxidation.²⁰ B) a) deaminocyclisation and $Cu_2Cr_2O_5$ dehydrogenation.²¹ C) a) thioalk/phenoxide or alk/phenoxide nucleophiles, methylpyrrolidone, microwave radiation.²² D) Example of coupling a diamine and diketone to make a 50:50 mixture of 235-EDMP/325-EDMP isomers. a) rt, 1 h, Et_2O , KOH . E) Proposed 325-EDMP biosynthesis in *Serratia marcescens* from L-threonine (**12**), showing a self-condensation step of **13**. a) oxidation/decarboxylation; b) spontaneous iminization condensation; c) tautomerization; d) acetyltransferase/Acetyl CoA, reductase (H^-/H^+ ; e) dehydratase, O_2 . F) Proposed 235-EDMP biosynthesis from mixed aminocarbonyl compounds, showing intermediates and products from self- and cross condensation. Steps b – e) are the same as in *Panel E*.

While green chemistry is becoming vital in the modern era, developing environment-friendly methods to synthesize pyrazines is a priority. Also, as the food and beverage industries continue to increase using pyrazines as ingredients for foodstuffs, a desire to develop "natural" pyrazines is growing.²⁷ It is interesting to note that synthetically derived pyrazines are not considered "natural" despite being structurally identical to a natural product.²⁸ Thus, a niche to address

growing consumer demand for "natural" ingredients has emerged, and biocatalytic processes are sought as alternatives to produce specific substituted pyrazine isomers by enzymatic methods.²⁷

Alk/AlkO-Pyrs are mainly used to improve the odor of cosmetics and toiletries in the perfume industry,^{27,29} while AlkPyrs have garnered interest recently and are supplied at ~2200 kg/year, as of 2004.^{27,30} The seven most extracted pyrazines from natural resources include 2,3,5-trimethylpyrazine (235-TMP); 2-ethyl-3-methylpyrazine (23-EMP); 2,5-dimethylpyrazine (25-DMP); 2,6-dimethylpyrazine (26-DMP); 2-ethyl-3,5-dimethylpyrazine (235-EDMP) and its constitutional isomer 3-ethyl-2,5-dimethyl (325-EDMP); 2,3-dimethylpyrazine (23-DMP); and methylpyrazine (MP). These compounds are used to favorably augment taste notes in various beverages, sauces, breakfast cereals, chocolate, coffee, cocoa, meat, potatoes, peanut products, popcorn, and bread.^{27,31}

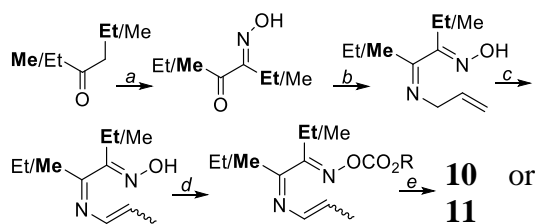
Among the many alkylpyrazines, the ethyl-dimethylpyrazines are among the most potent odorants (perceived as roasty and sweet). For example, 235-EDMP and 325-EDMP isomers are significant contributors to the desirable taste of Houjicha green tea.³¹ These EDMP isomers are only available by extraction from natural sources as mixtures in foodstuff, such as coffee aroma and raw plants, vegetables, fish, poultry, and beef.³

However, one account found 325-EDMP as a single isomer in the bacterium *Serratia marcescens*. The biosynthetic pathway to 325-EDMP was proposed to proceed through a C2-symmetrical 2,5-dimethyl-2,5-dihydropyrazine (25-DMDHP) intermediate derived after dehydration of a self-condensation product from 1-aminopropan-2-one (**13**) (Scheme 4.1E).³² A subsequent Friedel Crafts reaction with acetyl CoA followed by a keto-reduction, dehydration, and tautomerization are proposed to add the ethyl substituent found in 325-EDMP.³² Extrapolation of a similar biosynthetic route to 235-EDMP compared to that proposed for 325-

EDMP is less probable. The biosynthetic route to 235-EDMP needs to proceed through an analogous 26-DMDHP, and the amino carbonyl coupling partners require 1-aminopropan-2-one (**13**) and 2-aminopropanal (**15**) (Scheme 4.1F), analogous to aminoacetone needed on the 325-EDMP pathway. The drawback, in this case, is that **13** and **15** will self- and cross-couple to generate 2,6-dimethyl-2,5-dihydropyrazine (**16**) and 3,6-dimethyl-2,5-dihydropyrazine (**14**), and the downstream enzymatic steps, keto-reduction, dehydration, and tautomerization, would, unfortunately, lead to a 235- and 325-EDMP isomeric mixture.

The broad market appeal of pyrazines as additives is increasing; thus, additional resources for accessing EDMP as single isomers are needed. 235- and 325-EDMP isomers are used as flavoring agents, food additives, and fragrances,³³ and are found as added ingredients in cigarettes,³⁴ and related AlkPyr are found in e-cigarettes.³⁵ Given this broad chemosensory application of pyrazines, several accounts highlight the synthesis and separation of these commodity compounds.^{25,36,37} Commercially available mixtures of 235- and 325-EDMP isomers were chromatographically separated to show that each had a distinct effect on the behavioral response of fire ants in an electroantennogram study.³⁸ Earlier synthetic attempts to make 235- and 325-EDMP separately were successful but are challenged by multiple steps that increase the start-stop assembly sequences and affect the yield (Scheme 4.2).²⁴ Likely, the most direct route to the pyrazine framework is coupling a carbonyl compound with an alkyl amine partner in a condensation reaction. However, the chemical synthesis of a single constitutional isomer of EDMP by condensing an amine with a carbonyl compound occurs rapidly without regioselectivity. In this study, we evaluated the regioselectivity of the coupling

reaction between a diamine and α -hydroxy ketone. An earlier independent study evaluated the production of alkyl di- and tetrahydropyrazines, including the 5,6-dihydropyrazine precursors of 235- and 325-EDMP from α -hydroxy ketone made in baker's yeast whole cells and diamines.³⁹ This earlier study evaluated the products by GC-olfactometry (GC-O) and did not measure the selectivity of the condensation reaction. We used the enzyme pyruvate decarboxylase (PDC) isolated from baker's yeast (*Saccharomyces cerevisiae*) to obtain hydroxypentanone reactants to couple with propane-1,2-diamine, followed by KOH treatment to enrich each EDMP isomers regioselectively.



Scheme 4.2. a) isoamyl nitrite, conc HCl, Et₂O, 10-20 °C, 2 h; b) allylamine, hexane, reflux; c) potassium tert-butoxide, DMSO, 50 °C, 1-2 h; d) C1COOCH₃, Et₃N, CH₂Cl₂, 10-20 °C; e) short contact-time pyrolysis in toluene solution at ~300 °C.

4.2 Experimental

4.2.1 Chemicals, Reagents, and Instrumental Analysis.

All chemicals and reagents used for this study were obtained from Sigma-Aldrich (St. Louis, MO) and used without further purification unless noted otherwise.

4.2.2 Instrumentations.

Gas chromatography/electron-impact mass spectrometry (GC/EI-MS) analysis was performed on an Agilent 6890N gas chromatograph equipped with a capillary GC column (30 m × 0.25 mm × 0.25 μm; HP-5MS; J & W Scientific) with He as the carrier gas (flow rate, 1 mL/min). The injector port (at 250 °C) was set to splitless injection mode. A 1-μL aliquot of each sample was injected using an Agilent 7683 auto-sampler (Agilent, Atlanta, GA). The column temperature was increased from 40 to 150 °C at 10 °C/min, then increased by 20 °C/min to 250 °C with a 5 min hold, and returned to 40 °C. The gas chromatograph was coupled to a mass selective detector (Agilent 5973 *inert*) operated in electron impact mode (70 eV ionization voltage).

NMR experiments were recorded on an Agilent DDR2 500 MHz NMR spectrometer (500 MHz (¹H)) at 25 °C. ¹H NMR data was acquired using a recycle delay of 20 s and 32 scans. For Heteronuclear Single Quantum Correlation (HSQC) 2D-NMR experiments, the number of transients (nt) = 16 and the number of increments (ni) = 128. For acquiring Heteronuclear Multiple Bond Correlation (HMBC) 2D-NMR spectra nt = 16 and ni = 400. The ¹H NMR chemical shifts were referenced to that of residual protonated solvent in CDCl₃ (7.24 ppm).

An Agilent HP 1100 instrument (Agilent Technologies, San Diego, CA, USA) coupled to an analytical column (Alltech, 250 mm x 2.1 mm i.d., 5 μm particle size) or a semipreparative Alltech Econosil C-18 column (250 mm x 22 mm i.d., 10 μm particle size) attached to a UV-diode array detector were used to monitor (*A*₂₇₈) and separate the EDMP isomers. Guided by earlier HPLC solvent systems to separate pyrazines by C-18 RP-HPLC,^{38,40,41} various isocratic mixtures of CH₃CN (20% to 50%) in water were tested

as the eluent to optimize the resolution of elution (R_S). A volume of 1 μL of a 37 mM EDMP solution (dissolved in CH_3CN) was loaded onto the analytical column to determine a suitable solvent system of CH_3CN /water suitable for the semipreparative column. A 100 μL of a 37 mM EDMP solution (dissolved in CH_3CN) was loaded onto the semipreparative column and eluted with an isocratic CH_3CN /water mixture (20:80) at 5 mL/min. The elution volumes of the chromatographically separated EDMP isomers from multiple injections were collected, acidified to pH 1 (6M HCl) to convert the compounds to the pyrazinium chloride salts, and the solvent was removed under a stream of nitrogen.

4.2.3 Synthetic approach to produce 2-ethyl-3,5-dimethylpyrazine through diketone and diamine coupling.

Substrates propane-1,2-diamine (1 mM, 74 μL) and pentane-2,3-dione (1 mM, 100 μL) were incubated in diethyl ether (2 mL) at 25 $^\circ\text{C}$, 1 h, and the reaction was monitored by GC-MS analysis.

4.2.4 Assessing conditions for the diketone and diamine coupling reaction to increase the regioselectivity.

The coupling reaction between diketone and diamine was followed by different temperatures (-25 $^\circ\text{C}$, 0 $^\circ\text{C}$, rt) and changing the addition order of the reactants (pentane-2,3-dione and propane-1,2-diamine) to the reaction mixture. Different Zeolites (**ZBH**: Zeolite beta, hydrogen ($\text{SiO}_2/\text{Al}_2\text{O}_3$ –360:1); **ZYH**: Zeolite Y, hydrogen ($\text{SiO}_2/\text{Al}_2\text{O}_3$ – 80:1); **ZMA**: Zeolite mordenite, ammonium ($\text{SiO}_2/\text{Al}_2\text{O}_3$ – 20:1); **ZSM**: Zeolite ZSM-5, ammonium ($\text{SiO}_2/\text{Al}_2\text{O}_3$ –200 to 400:1)) were used as a blocking agent and followed the coupling reaction.

4.2.5 Synthesis of hydroxypentanones **17** and **18**.

A pyruvate decarboxylase (PDC) (E.C. 4.1.1.1) (10 mg, 5 U) from baker's yeast (*S. cerevisiae*) was added to 0.1 M sodium citrate buffer (pH 6.0) (4 mL) containing 2 mM thiamine diphosphate (3.68 mg) and 20 mM MgSO₄ (9.6 mg). Acetaldehyde (2 mmol, 88 μ L) and 2-oxobutanoate sodium salt (1.5 mmol, 185 mg) were added to the reaction mixture and incubated at 25 °C for 48 h. The reaction mixture was extracted with diethyl ether (3 \times 2 mL). The organic fractions were combined, and the solvent was removed under a stream of nitrogen. The resulting residue (~82 mg) without further purification was dissolved in CDCl₃ and analyzed by ¹H NMR to judge the 2-hydroxypentan-3-one (**17**) at ~43% converted yield (Figure S58 of the Supporting Information). An aliquot of the crude sample was dissolved in ether and analyzed by GC/EI-MS in selected-ion and total ion modes.

The synthesis and workup of 3-hydroxypentan-2-one (**18**) were similar to those described for **17** except that propionaldehyde (2.5 mmol, 145 μ L) and 2-oxopropanoate (i.e., pyruvate) sodium salt (2 mmol, 220 mg) were used in place of acetaldehyde and 2-oxobutanoate, respectively, during the synthesis. These co-substrates were incubated with the PDC enzyme (10 mg, 10 U).

After concentrating the sample, the resulting residue (~90 mg) without further purification was dissolved in CDCl₃ and analyzed by ¹H NMR (Figure S60 of the Supporting Information). An aliquot of the crude sample was dissolved in ether and analyzed by GC/EI-MS in selected-ion and total ion modes.

4.2.6 Synthesis of EDMP isomers.

Propane-1,2-diamine (1 mmol, 74 μ L) and **1** or **2** (~0.9 mmol, ~90 mg) were mixed in ether (2 mL) and incubated at rt for 1 h. KOH pellets (1 mmol, 56 mg) were stirred with the reaction mixture at rt in an open-air container for 2 h to convert the dihydropyrazine intermediates to the aromatic EDMP isomers. The resulting mixture was filtered, and the ether layer was separated from the residual water made during the dehydration steps of the reaction. An aliquot (1 μ L) from the ether layer was analyzed by GC/EI-MS. The EDMP isomers were quantified using a standard curve with 2,5-DMP as the internal standard. The converted yields were calculated based on the amount of substrate added to the reaction mixture.

In complex samples, the TIC chromatogram often provides limited information as multiple analytes elute simultaneously, obscuring individual species. We understand that the ionization of different molecules analyzed by GC/EI-MS can vary, often seen in different total ion abundances for different compounds present at a 1:1 molar ratio in a sample analyzed by GC/EI-MS. The ionization efficiency and production of fragment ions depend strongly on the chemistry of the analyte and the energy of the ionizing electrons.⁴² As a consequence, mass spectrometry is not inherently quantitative because of differences in the ionization efficiency of various compounds in a given sample. However, to estimate an approximate purity of the synthesized EDMP isomers in the crude sample, we assumed the average ionization potential for all analytes present in the crude EDMP sample mixtures were the same when analyzed by GC/EI-MS.

4.2.7 HPLC separation to isolate 235-EDMP from a commercially available EDMP mixture.

The EDMP isomeric mixture (Sigma-Aldrich, St. Louis, MO) contained a 50:50 mixture of each isomer (235-EDMP and 325-EDMP), as determined by GC/MS analysis. A 1 μL -aliquot (from a 5 mg EDMP/mL sample dissolved in CH_3CN) was loaded onto the analytical column (Alltech, C18, 250 mm x 2.1 mm i.d., 5 μm particle size) to determine that a solvent mixture of CH_3CN /water (20:80, isocratic) was suitable as the mobile phase for the larger-scale separation.

For the preparative-scale separation of the EDMP isomers, a 100 μL -aliquot (from a 5 mg EDMP/mL sample dissolved in CH_3CN) was loaded onto a preparative column (Alltech Econosil, C18, 250 mm x 22 mm i.d., 10 μm particle size) and eluted with CH_3CN /water (20:80, isocratic) at 5 mL/min. The elution volume of each of the two peaks was separately collected. The fractions from multiple 100 μL -injections for each peak were combined, acidified to pH 1 (6M HCl) to convert the pyrazines to their HCl salts, and concentrated under a stream of nitrogen. The separated EDMP isomers were analyzed by NMR and GC-MS to characterize the 235-EDMP and 325-EDMP isomers.

4.3 Results and Discussion

4.3.1 Separation of the EDMP Isomers.

This study aimed to develop a method to make 2-ethyl-3,5-dimethylpyrazine (235-EDMP, **10**) selectively over its 3-ethyl-2,5-dimethylpyrazine (325-EDMP, **11**) isomer. Each individual isomer is not available commercially; thus, we needed to separate them and characterize their identities unequivocally to help differentiate the products from our

synthetic trials. A commercial-grade 50:50 mixture of EDMP isomers was used to separate **10** from **11**. Separation by fractional distillation was not practical because the boiling points of **10** and **11** are similar (181-182 °C).⁴³ Therefore, we separated the isomers by preparative, reverse-phase HPLC with UV monitoring of the effluent (Figure 4.2A), based on a previous technique.³⁸ We evaluated the relative purity of each isomer by GC/EI-MS before (Figure 4.2B) and after purification, judged to be ~95% pure (Figure 4.2C, D). The shorter retention-time pyrazine on the GC/EI-MS was designated as **11** (Figure 4.2C), and the longer retention-time compound was assigned as **10** (Figure 4.2D) based on separate validation of each compound by NMR experiments.

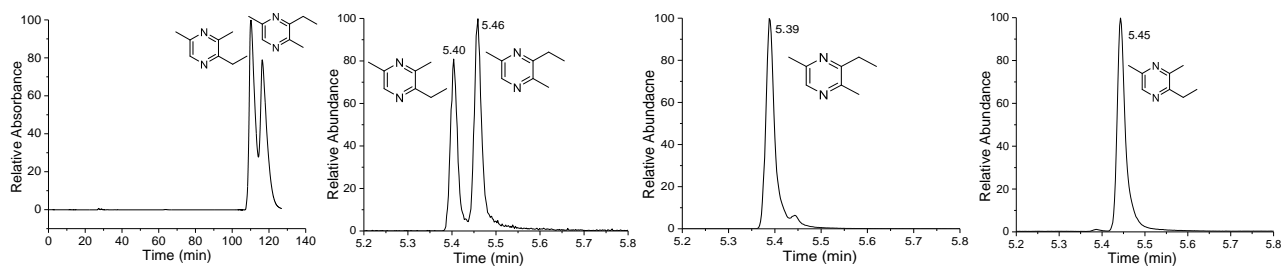


Figure 4.2. A) HPLC chromatogram of 1:1 mixture of commercial **10** and **11** (mobile phase: 20:80 CH₃CN/H₂O on an Alltech Econosil C-18 column, 10 μ (250 mm \times 22 mm) with a 5 mL/min flow rate with A₂₇₈ monitoring of the effluent. B) GC/EI-MS profiles (selected-ion mode, *m/z* 136) of 1:1 mixture of commercial **10** and **11**, C) purified 325-EDMP (**11**) and D) 235-EDMP (**10**).

NMR Characterization of the EDMP Isomers. The separate eluent fractions isolated from the reverse-phase HPLC were acidified to convert the pyrazines to their nonvolatile HCl salts. Each fraction was concentrated and analyzed by 1D-¹H- and ¹³C-NMR, 2D-HSQC (Heteronuclear Single Quantum Coherence Spectroscopy), and 2D-HMBC (Heteronuclear Multiple Bond Correlation) to unambiguously characterize each EDMP. The HSQC NMR spectrum showed one-bond C-H (¹J_{CH}) correlations for the methyl, ethyl, and aryl ring carbons and attached hydrogens and confirmed distinct chemical shift differences for each EDMP isomer (Figure S52 - Figure S56) of the Supporting Information).

The HSQC data alone provided important information about the alkyl substitution on the aromatic ring but was not conclusive to distinguish one isomer from the other.

A combination of long-range, diagnostic correlations were made from the HMBC data that showed two and three through-bond C-H correlations ($^2J_{\text{CH}}$ and $^3J_{\text{CH}}$) that helped distinguish the purified EDMP isomers **10** and **11**. The spectrum for one EDMP isomer had correlations between the aryl hydrogen (H-6), C-2 (ethyl attachment), C-5 (methyl attachment) and C10 (methyl), and between the ethyl substituent hydrogens (H-7 and H-8) and C-2 (Figure 4.3A,). This combination of $^2J_{\text{CH}}$ and $^3J_{\text{CH}}$ HMBC correlations helped validate the alkyl substitution patterns on the pyrazine ring that were consistent with the 235-EDMP structure (**10**). The distinct long-range HMBC correlations in **10** (Figure S53 of the Supporting Information) contrasted those in **11** (Figure S57 of the Supporting Information), which were between the aryl hydrogen (H-6), C-2 (methyl-7 attachment), and C-5 (methyl-10 attachment) (Figure 4.3B, Figure S57). This spin-coupled system revealed the "*ortho*"/"*meta*"-locations of the methyl substituents relative to H-6. Reciprocally, H-10 correlated with C-6, the unsubstituted aryl carbon, and this spin system reinforced the C-10 (methyl) position. There was no crosstalk between H-6 and either of the ethyl carbons, suggesting a >3-bond distance between these sets of atoms and supporting the 325-EDMP structure (**11**).

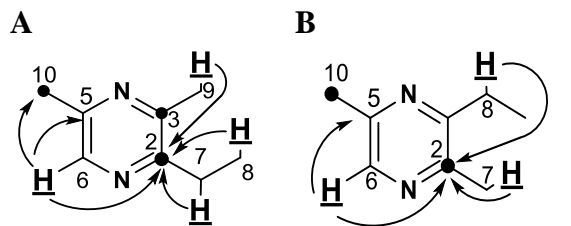


Figure 4.3. Key structural $^2J_{\text{CH}}$ and $^3J_{\text{CH}}$ HMBC correlations within A) 235-EDMP (**10**) and B) 325-EDMP (**11**) between carbon (●) and hydrogen (shown explicitly as **bold** and underlined). The pyrazine ring numbering is shown.

4.3.2 Regioselective Assembly of EDMP Isomer.

4.3.2.1 Synthetic Assembly of 235 EDMP.

A direct route to the pyrazine framework is to couple a carbonyl compound with an alkyl amine partner in a condensation reaction, but this coupling occurs rapidly without regioselectivity. We explored different reaction conditions to couple pentan-2,3-dione and propane-1,2-diamine to direct the regioselectivity. First, the coupling reaction was carried out at different temperatures (-25 °C, 0 °C, and room temperature (~23 °C)) to assess if the temperature could, in part, control the steric approach of the reagents. We envisioned that at sub-ambient temperatures, the terminal amine of the propane-1,2-diamine reactant could preferentially select for the less encumbered methyl-substituted ketone of the pentan-2,3-dione co-reactant. For each of the temperature control reactions, the order and rate (dropwise or single bolus) in which the reactants were added to the reaction mixture were changed. We also hypothesized that various microporous zeolites could provide cavitation to coordinate the internal ammonium group of the diamine and the least sterically blocked methyl keto group of the 2,3-diketone through protonation. These interactions were imagined to direct regioselective imine

formation between the terminal amino group and the ethyl keto group of the reactants toward the desired 235-EDMP. Undesirably, all these approaches resulted in 50:50 isomeric mixtures of 235-EDMP and 325-EDMP (Figure 4.4). It was apparent that the steric in each of the reactants provide little regioselective control in the transition state to yield the 235-EDMP preferentially under the tested conditions.

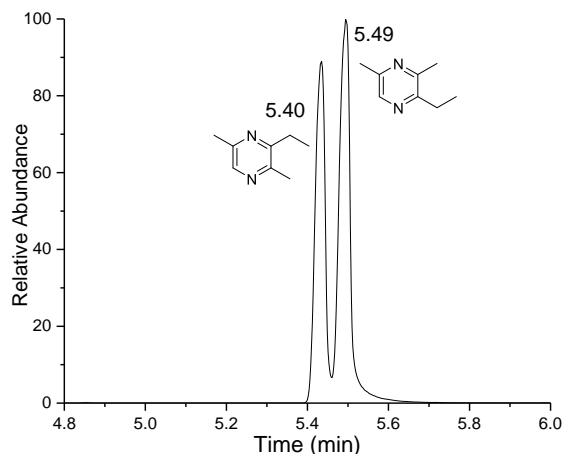


Figure 4.4. A representative partial GC/EI-MS chromatogram with selected-ion monitoring (m/z 136) of 235- and 325-EDMP at 50:50 relative abundance in the product mixture after incubating 1,2-diaminopropane and pentan-2,3-dione (dropwise addition) at 0 °C for 1 h and then air oxidation.

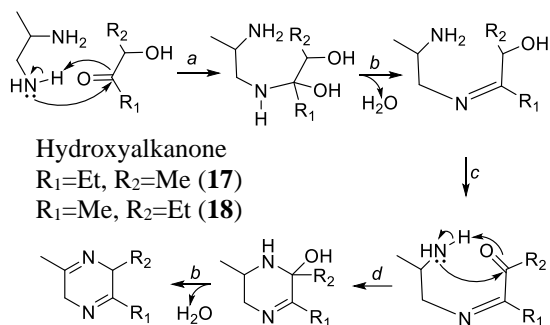
We considered the benefits of synthetic strategies for assembling aromatic *N*-heterocycles, including metal-free and metal-catalyzed methods for multicomponent reactions.⁴⁴ Specifically, many earlier successful efforts to synthesize 235- and 325-EDMP separately were less appealing because they progressed through multistep procedures, high temperature, and toxic solvents, resulting in moderate yield.²⁴ In this study, we pursued an alternative semibiocatalytic method using inexpensive starting materials to prepare the desired commodity 235-EDMP (and 325-EDMP) heterocycles.

4.3.3 Semibiocatalytic Assembly of Isomerically Enriched EDMP Isomers.

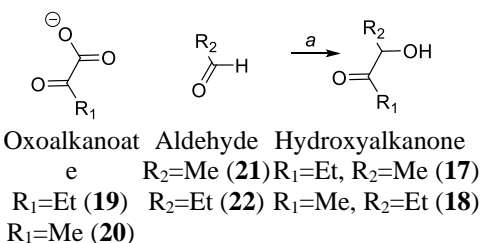
4.3.3.1 Biocatalysis of Alkyl Acyloins.

Our approach looked at changing the functional group reactivity of the electrophilic reactant (pentan-2,3-dione, **9**). The diketone electrophile substrate was replaced with a hydroxy ketone reactant to couple with the diamine (**8**) nucleophile. An earlier study demonstrated the coupling reaction success, using whole-cell yeast to make an array of α -hydroxy ketones from exogenously fed aldehydes and pyruvate.³⁹ Ultimately, the hydroxy ketones were coupled with alkyl-diamine **8** in situ to make various alkyl dihydro- and tetrahydropyrazines. With the application of α -hydroxy ketones as the electrophile, we imagined a similar mechanism proposed in an earlier study³⁹ showing the terminal amino group of diamine **8** reacting selectively with the keto functional group of 2-hydroxypentan-3-one (**17**). This initial coupling preference would influence the overall reaction selectivity toward the 235-EDMP isomer (Scheme 4.3). We tested this hypothesis by preparing **17** biocatalytically (Scheme 4.3) with commercial pyruvate decarboxylase (PDC) isolated from *S. cerevisiae*. In nature, PDC catalyzes the nonoxidative decarboxylation of pyruvate to acetaldehyde using thiamine diphosphate and Mg^{2+} ions as cofactors in ethanol production in plants and fungi.³⁹ PDC can also catalyze off-pathway carbonylation reactions to form acyloins by condensing an acetaldehyde and 2-oxoalkanoic acids to make dialkyl acyloins^{39,45} that are desired for this study. We incubated PDC with acetaldehyde (**21**, C₂-moiety) and propanal (**22**, C₃-moiety) and oxoalkanoate sodium salts **19** and **20** to make **17** and **18** hydroxypentanones (Scheme 4.4), respectively. In this study, the carbon building blocks (acetaldehyde for the C₂-moiety and 2-oxobutanoic acid as a precursor for the C₃-moiety) differed from those

used as feedstocks (pyruvate as a precursor for the C₂-moiety and propanal for the C₃-moiety) in the earlier report on the whole-cell assembly of a mixture of hydroxy pentanones **17** (3.9% yield) and **18** (0.5% yield).³⁹



Scheme 4.3. A proposed mechanism for the formation of 5,6-dihydropyrazine intermediates toward pyrazines from condensation between acylalans and 1,2-propanediamine: *a*) condensation between the less hindered amine with the keto group of the hydroxyketone substrate, *b*) proton transfer and dehydration, *c*) enolization and tautomerization, and *d*) condensation between the internal amine and the keto group.



Scheme 4.4. Synthesis of hydroxypentanones (**17** and **18**) from the appropriate aldehyde and oxoalkanoate incubated with a) pyruvate decarboxylase (PDC), MgSO₄, and thiamine diphosphate in sodium citrate buffer.

Here, we extracted the biocatalyzed 2-hydroxypentan-3-one (**17**) from the aqueous enzyme incubation buffer with ether and removed the organic solvent to obtain a crude product mixture. ¹H NMR analysis of **17** without purification had diagnostic chemical shifts at δ 1.18 (3H, triplet,

$J = 7.2$ Hz) and δ 3.01 (2H, quartet, $J = 7.5$ Hz) for the ethyl attached to the keto group and at δ 1.43 (3H, doublet, $J = 6.7$ Hz) and δ 4.86 (1H, quartet, $J = 6.1$ Hz) for the hydroxyethyl attached to the other side of the keto group (Figure S58 of the Supporting Information for product numbering). In the sample containing **17**, **18** was not easily identified by signature ^1H NMR signals.

The crude sample containing the biocatalyzed 3-hydroxypentan-2-one (**18**) was extracted and analyzed identically to the methods described for **17**. ^1H NMR data for the crude sample of **18** was more challenging to interpret because diagnostic chemical shifts were not readily discernible. The homonuclear COSY spectra of a reference compound 3-hydroxy-2-hexanone⁴⁶ with similar structural features to 3-hydroxy-2-ketone **18**, made in our study, were used to assign the expected chemical shift values for **18**. The COSY spectrum for putative **18** made biocatalytically had putative ^1H - ^1H correlations between H4 and H5 (the terminal ethyl group) but lack diagnostic correlations between H3 (attached to the C-OH) and the neighboring protons (Figure S60 of the Supporting Information) as seen for 3-hydroxy-2-hexanone (Figure S59 of the Supporting Information). Therefore, the sample was analyzed by GC/EI-MS to determine if **18** had been made.

A selected ion chromatogram of the crude sample putatively containing **18** showed a chromatographic peak corresponding to a compound that fragmented into ions consistent with 3-hydroxypentan-2-one (Figure 4.5A,B). Diagnostic fragment ions for the 2-hydroxypentan-3-one isomer **17** (at 40% abundance relative to **18**) were also detected for a peak eluting at 5.43 min (see Figure 4.6B for ion fragments). Evaluation of the GC/EI-MS total ion chromatogram for the crude sample, where **18** was the intended biocatalysis product, showed several other peaks with

ion abundances above those for **17** and **18**. The compound identities of the most abundant peaks were identified by comparing their fragment ion profiles against those in spectral databases (Figure 4.5C). Each off-pathway product can arise from the excess propanal substrate used to stimulate the reaction biocatalyzed by the PDC enzyme. These other compounds included 2-methylpent-2-enal (5.74 min) resulting from dehydration of 3-hydroxy-2-methylpentanal, 3-hydroxy-2-methylpentanal (7.93 min) derived from aldol condensation between two propanal molecules, and 2,6-diethyl-5-methyl-1,3-dioxan-4-ol (12.15 min) resulting from condensation between 3-hydroxy-2-methylpentanal and propanal (Figure 4.5C).

We evaluated the selected-ion chromatogram of the crude sample containing **17** to gain insight into why the ^1H NMR for **17** biocatalyzed by PDC from 2-oxobutanoate and acetaldehyde was more interpretable than the ^1H NMR for **18**. The selected-ion chromatogram showed a chromatographic peak (at 5.42 min) corresponding to a compound that fragmented into ions consistent with 2-hydroxypentan-3-one (Figure 4.6A,B). Diagnostic fragment ions for the 3-hydroxypentan-2-one isomer **18** (at ~30% abundance relative to **17**) were also detected for a peak eluting at 5.29 min (see Figure 4.5B for ion fragments). GC/EI-MS total-ion analysis of the crude sample, where **17** was the intended biocatalysis product, showed other peaks with significantly lower ion abundances than those for **17** and **18** (Figure 4.6C). One relatively abundant peak eluting at 4.85 min was identified as paraldehyde resulting from self-condensation of the acetaldehyde cosubstrate.

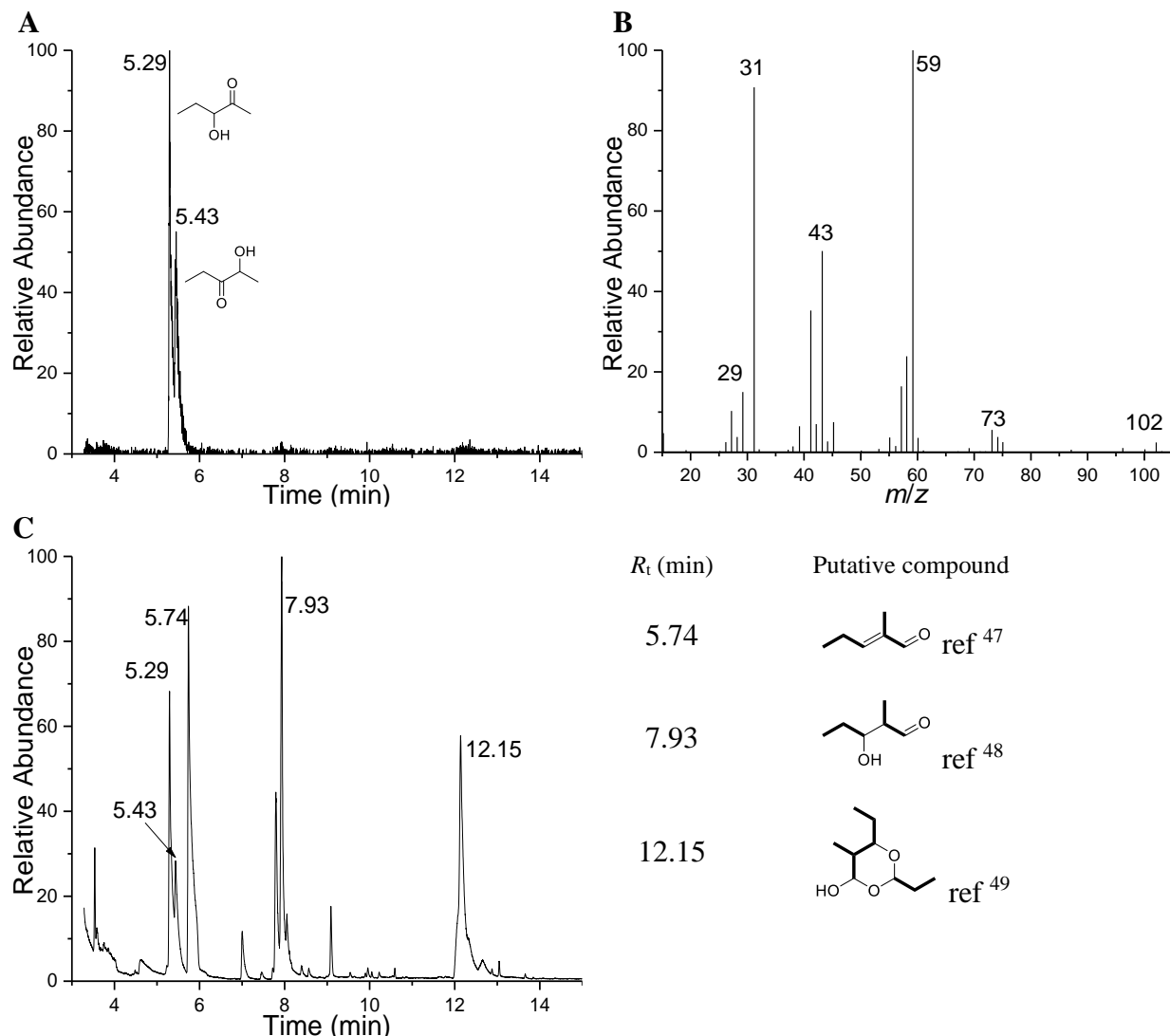


Figure 4.5. A) The GC/EI-MS selected-ion (m/z 102) profile of the crude product extracted from the reaction mixture after incubating PDC, propanal, and pyruvate to make 3-hydroxypentan-2-one. B) The compound eluting at $R_t = 5.29$ min in *Panel A* had EI-MS fragment ions consistent with the α -cleavage sites of 3-hydroxypentan-2-one. The compound eluting at $R_t = 5.43$ min in *Panel A* had EI-MS fragment ions consistent with α -cleavage sites of 2-hydroxypentan-3-one (see Figure 4.6B). C) The GC/EI-MS total ion chromatogram of the crude product described for *Panel A*. Putative compounds within the biocatalysis-derived sample whose peak thresholds were greater than or equal to those for the hydroxypentanones at $R_t = 5.29$ min and 5.43 min and had relative fragment ions abundances like those listed in a spectral database (see Figure S61 - Figure S63 for fragment ion profiles).^{47,48} The coupled carbon-chain moieties originating from propanal are highlighted with **bold** C-C bonds.

We concluded that the PDC carboligation efficiency for substrates 2-oxobutanoate (**19**, non-natural substrate) and acetaldehyde (**21**, natural substrate) to make **17** was more significant (~43% converted yield) than for pyruvate (**20**, natural substrate) and propanal (**22**, non-natural substrate) substrates to make **18** (~15% converted yield) (Table 4.1). This notion suggests that PDC is more permissive for non-natural 2-oxo-alkanoate substrates than for non-native alkanal substrates longer than acetaldehyde. The greater relative abundance of **17** made biocatalytically within its crude sample matrix enabled diagnostic NMR analysis, and a similar analysis was precluded for the lower abundant **18** made biocatalytically within its sample milieu.

^aArb. Units: Arbitrary Units; ^bSM: starting material; ^cbased on 1.5 mmol of **19** and **21** each; ^dbased on 2 mmol of **20** and **22** each

Table 4.1. Estimated Yield of Hydroxyketone (HK) Synthesis

	Reaction between 19 and 21 to obtain HK 17	Reaction between 20 and 22 to obtain HK 18
Total-Ion Area of all Peaks (Arb. Units) ^a	92,034,784	834,567,459
Total-Ion Area of HK peaks (Arb. Units)	72,903,474	275,348,978
Estimated HK Purity (based on peak area)	80%	33%
Gravimetric Yield of Crude Product	82 mg	90 mg
Estimated Yield of HK in Crude Product	65 mg (0.6 mmol)	30 mg (0.3 mmol)
Converted Yield (based on SM ^b)	43% ^c	15% ^d

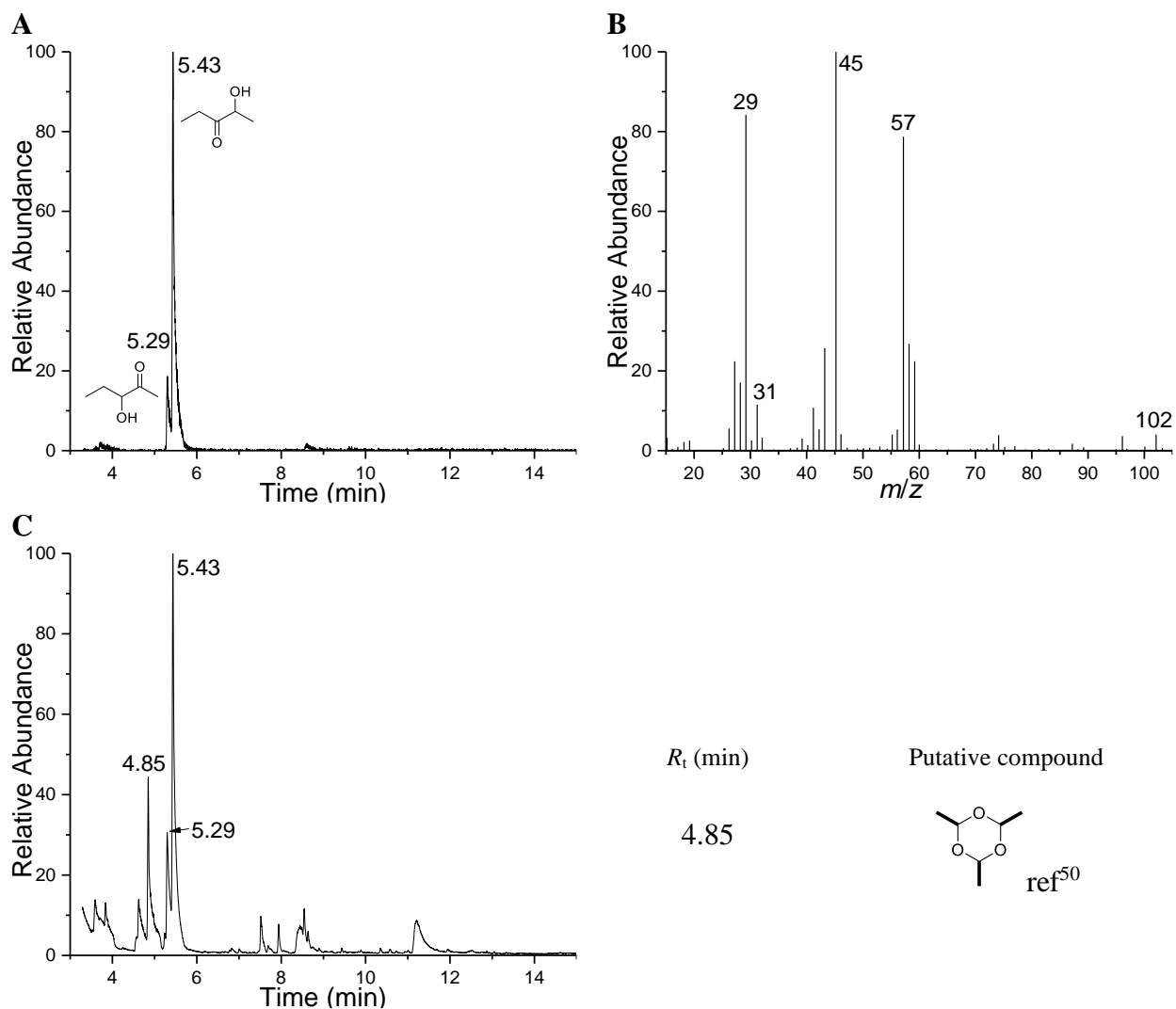


Figure 4.6. A) The GC/EI-MS selected-ion (m/z 102) profile of the crude product extracted from the reaction mixture after incubating PDC, acetaldehyde, and 2-oxobutanoate to make 2-hydroxypentan-3-one. B) The compound eluting at $R_t = 5.43$ min in *Panel A* had EI-MS fragment ions consistent with the α -cleavage sites of 2-hydroxypentan-3-one. The compound eluting at $R_t = 5.29$ min in *Panel A* had EI-MS fragment ions consistent with α -cleavage sites of 3-hydroxypentan-2-one (see Figure 4.5). C) The GC/EI-MS total ion chromatogram of the crude product described for *Panel A*. A compound ($R_t = 4.85$ min) within the biocatalysis-derived sample whose peak threshold was approximately equal to those for the hydroxypentanones at $R_t = 5.29$ min and 5.43 min and had relative fragment ions abundances like those listed in a spectral database⁵⁰ (see Figure S64 for fragment ion profile). The coupled carbon-chain moieties originating from acetaldehyde are highlighted with bold C-C bonds.

4.3.4 Assembly of Isomerically Enriched 235-EDMP.

Diamine (**8**) and the crude sample of **17** (Scheme 4.3) were mixed in ether for 2 h. GC/EI-MS analysis of the product mixture showed that dihydropyrazine intermediates of the EDMP isomers were made at a 70:30 ratio, based on the peak area (Figure 4.7A); the identity of each putative trialkyl dihydropyrazines was not characterized by NMR or comparison against authentic standards. The sample containing the putative dihydropyrazines were oxidized in open-air conditions in a basic (KOH pellets) ether emulsion to obtain the EDMP isomers at a 70:30 ratio; the 235-EDMP isomer (**10**) predominated (Figure 4.7C). The products corresponding to the GC/EI-MS peaks were identified based on an earlier preparative HPLC separation and characterization of the EDMP isomers by NMR analysis. The converted yield of 235-EDMP (~77 mg) and 325-EDMP (~33 mg) was estimated from the relative ion abundance of each isomer in the sample and the 110 mg total calculated from a standard curve for EDMP. The approximate purity of the synthesized EDMP isomers in the crude sample was estimated at 29 % (Table 4.2).

4.3.5 Assembly of Isomerically Enriched 325-EDMP.

We biocatalyzed an isomerically enriched sample of 325-EDMP (**11**) from the hydroxyketone isomer (**18**, Scheme 4.3) incubated with diamine **8**. GC/EI-MS analysis of the product mixture showed that dihydropyrazine intermediates of the EDMP isomers were obtained at a 40:60 ratio (Figure 4.7C). The dihydropyrazines were oxidized in open-air conditions in a basic (KOH pellets) ether emulsion and converted to a 40:60 mixture of the EDMP isomers with 325-EDMP (**11**) predominating over its isomer **10** (Figure 4.7D). The products corresponding to the GC/EI-MS peaks were identified based on an earlier preparative HPLC separation and characterization of the EDMP isomers by NMR analysis. The yield of 325-EDMP (~57 mg) and

235-EDMP (~38 mg) was estimated from the relative ion abundance of each isomer in the sample and the 95 mg total calculated from a standard curve for EDMP. The approximate purity of the synthesized EDMP isomers in the crude sample was estimated at 9 % (Table 4.2).

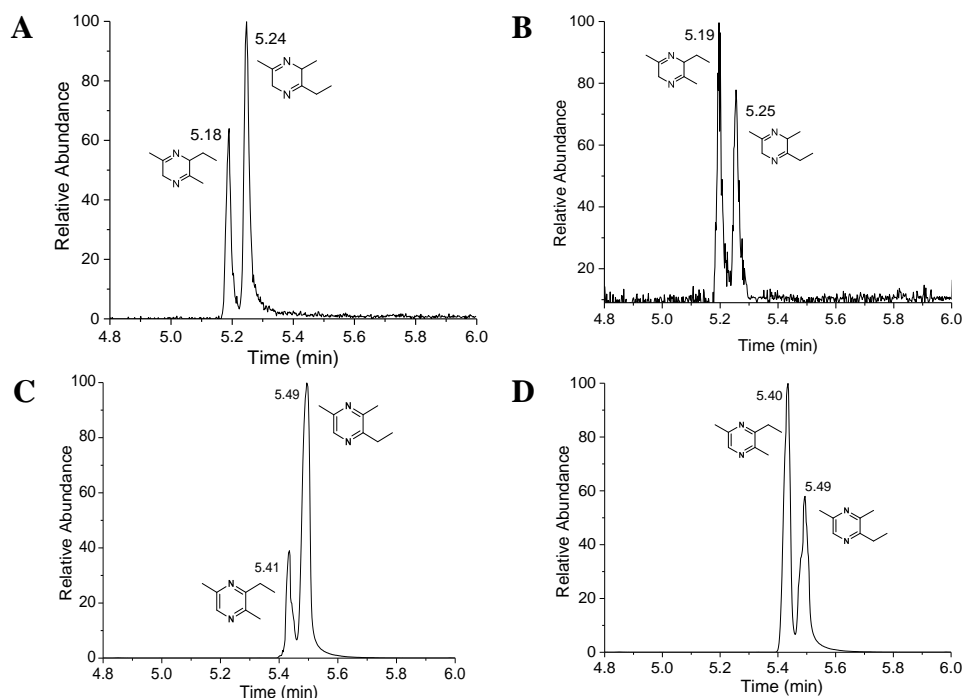


Figure 4.7. Partial GC/EI-MS chromatograms with selected-ion monitoring of the dihydropyrazines (m/z 138) in the product mixture after incubating propane-1,2-diamine (8) with A) 2-hydroxypentan-3-one (17) and B) 3-hydroxypentan-2-one (18). Partial GC/EI-MS profile with selected-ion monitoring of the EDMPs (m/z 136) after air-oxidation of the dihydropyrazines in the sample analyzed C) in Panel A and D) in Panel B.

Table 4.2. Estimated Purity of the Isomerically Enriched EDMPs

	Reaction between 17 and 8	Reaction between 18 and 8
Total-Ion Area of all Peaks (Arb. Units) ^a	120,009,233	1,443,120,234
Total-Ion Area of EDMP Peaks (Arb. Units)	34, 593,456	125,235,678
Estimated EDMP Purity (based on peak area)	29%	9%
Total EDMP Yield (mmol) (from standard curve; Rel. Abund. Figure 7C)	0.81mmol (110 mg) 235-EDMP (77 mg); 325- EDMP (33 mg) ^c	0.70 mmol (95 mg) 235-EDMP (38 mg); 325- EDMP (57 mg) ^d
Converted Yield (based on SM ^b)	235-EDMP (63%); 325- EDMP (27%)	235-EDMP (35%); 325- EDMP (53%)

^aArb. Units: Arbitrary Units; ^bSM: starting material; ^cbased on 0.9 mmol of **17** and **8** each; ^dbased on 0.8 mmol of **18** and **8** each

4.3.6 Putative side-products in EDMP Preparations.

The GC/EI-MS total ion chromatogram for the crude sample, where **10** was predominant at 70:30 over its EDMP isomer **11**, showed several other peaks with ion abundances similar to those for **10** and **11** (Figure 4.8A). The side products putatively identified were either formed chemically during the coupling reaction between the diamine (**8**) and off-pathway products in the crude sample of **17** or by unexpected, accelerated reactions of unreacted starting reagents in the hot injector port (235 °C) of the GC instrument.⁵¹ The compound identities of some most abundant peaks were identified by comparing their fragment ion profiles against those in spectral databases. For example, the side products eluting from the GC (Figure 4.8A) whose EI-MS fragmentation matched best to those in mass spectral databases included *cis/trans*-2,6-dimethylpiperazine (Figure 4.8C,D) and *cis/trans*-2,5-dimethylpiperazine (Figure 4.8E,F) resulting from parallel and antiparallel dimerization, respectively, of diamine (**8**). Other compounds eluting at 3.87, 4.12, 4.51, 4.60, and 4.79 min did not have fragment ion

profiles matching those in the mass spectral databases but contained fragment ions that could be inferred from related azo-compounds⁵² (Figure S67A, B, C of the Supporting Information). The compound eluting at 7.52 min (Figure 4.8A) fragmented into ions that were consistent with those for a putative alkyl ester with a molecular formula of C₉H₁₆O₂ (Figure S67D of the Supporting Information).

The GC/EI-MS total ion chromatogram for the crude sample, where **11** was predominant at 60:40 over its EDMP isomer **10**, showed other peaks with ion abundances greater than those for **10** and **11** (Figure 4.8B). Curiously, several of the side products coeluted from the GC for this crude sample compared to the more resolved compounds in the sample where **10** was predominant over its EDMP isomer **11** (Figure 4.8A). Many of the same fragment ions (*m/z* 114, 99, 85, 70, 56, 58) consistent with azo-compounds were identified as before (Figure S67 E, F).

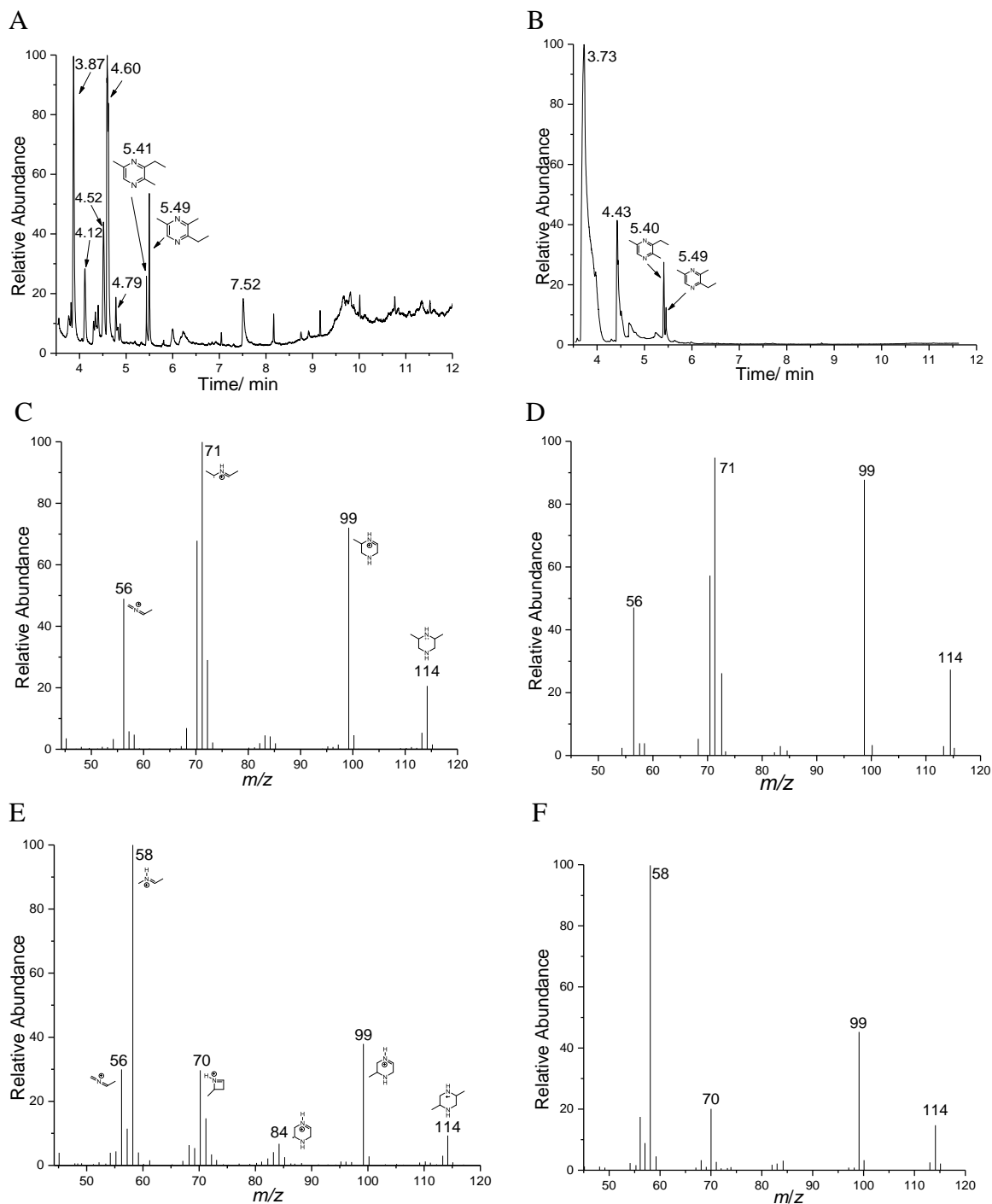


Figure 4.8. GC/EI-MS total ion chromatogram (TIC) of products isolated from the crude reaction mixture after incubating 1,2-diaminopropane with A) 2-hydroxy-3-pentanone and B) 3-hydroxy-2-pentanone. The EDMPs **10** (~5.40 min) and **11** (5.49 min) are highlighted. C) EI-MS fragmentation profile of compound eluting from the GC at 4.60 min in the TIC profile (*Panel A*); D) a similar fragmentation ion profile was identified for 2,6-dimethylpiperazine in a mass spectral database.⁵³ E) EI-MS fragmentation profile of peak eluting from the GC at 4.79 min in the TIC profile (*Panel A*); F) a similar fragmentation ion profile was identified in a mass spectral database for 2,5-dimethylpiperazine.⁵⁴

4.4 Conclusion

Pyrazines are used as synthetic precursors in medicinal chemistry and are of interest within the pharmaceutical sector.⁵⁵ A SciFinderⁿ database query for all types of substituted pyrazines reports ~950 compounds. Of these, ~185 are a combination of tri-*n*-alkyl- / cycloalkyl-substituted pyrazines. This dearth of citations reflects limited methods for alkylpyrazine preparation.⁵⁶ The application of a green, all-natural route to 325-EDMP alkylpyrazine via a viable, proposed biosynthetic route is promising toward potentially increasing titers. However, a parallel biosynthetic route to the 235-EDMP isomer cannot be envisaged without invoking carbonyl/amine reagents that would self- and cross-couple to produce an uncontrolled mixture of intermediate products. Here, we reported a semibiocatalytic method that employed a decarboxylase to access a sample enriched in the prerequisite 2-hydroxypentan-3-one (**17**) reactant. The electrophile **17** was reacted with propane-1,2-diamine (**8**) to make a 70:30 isomerically enriched mixture of 235-EDMP (**10**) over 325-EDMP (**11**). We intuit the 70:30 isomeric ratio of **10**: **11** is established by the 70:30 ratio of hydroxypentanones (**17**:**18**) (Figure 4.6A) made in the carboligation reaction catalyzed by the decarboxylase from cosubstrates 2-oxobutanoate and acetaldehyde. We view this reaction as being controlled by the greater reactivity of the carbonyl group over the hydroxyl of the acyloin and the terminal amine over the internal amine of the diamine **8**. As proof-of-principle, 3-hydroxypentan-2-one (**18**) was used in place of **17** to make the 325-EDMP isomer when reacted with diamine **8** in modest 60:40 enrichment over the 235-isomer. Again, the 60:40 enrichment was considered to result mainly from the 60:40 ratio of hydroxypentanones **18**:**17** made in the carboligation reaction catalyzed by the decarboxylase from cosubstrates pyruvate and propanal (Figure 4.5A).

This synthetic enrichment step is a significant advance in the assembly of trialalkylpyrazines from typical reagents involving a diamine and bifunctional alkadiones that produce statistical mixtures of all condensation products or self-condensation of an alkoxy amine that produces a limited number of symmetrical pyrazines. Further mechanistic and kinetic studies of the enzyme-catalyzed PDC carbonylation and imine condensation reactions are anticipated to understand better how to enrich each EDMP isomer regioselectively.

APPENDIX

APPENDIX

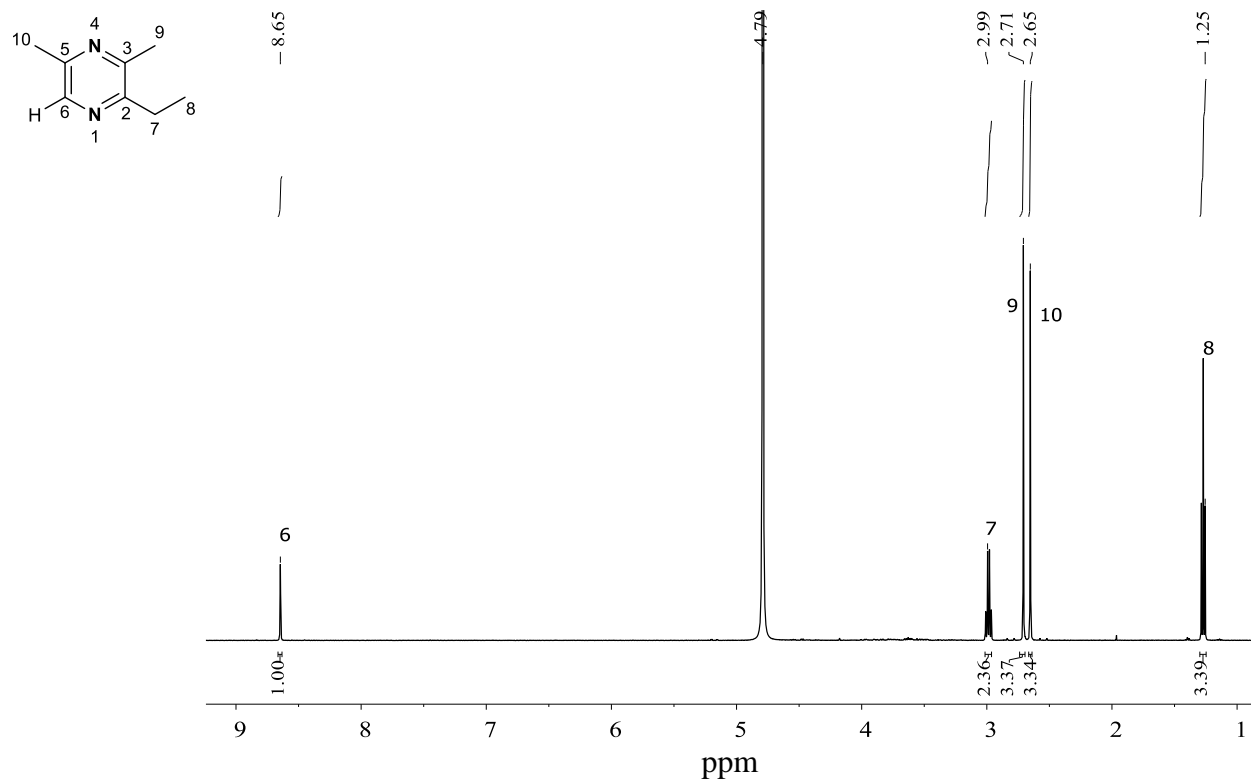


Figure S50. ^1H NMR (500 MHz, D_2O) of 235-EDMP.

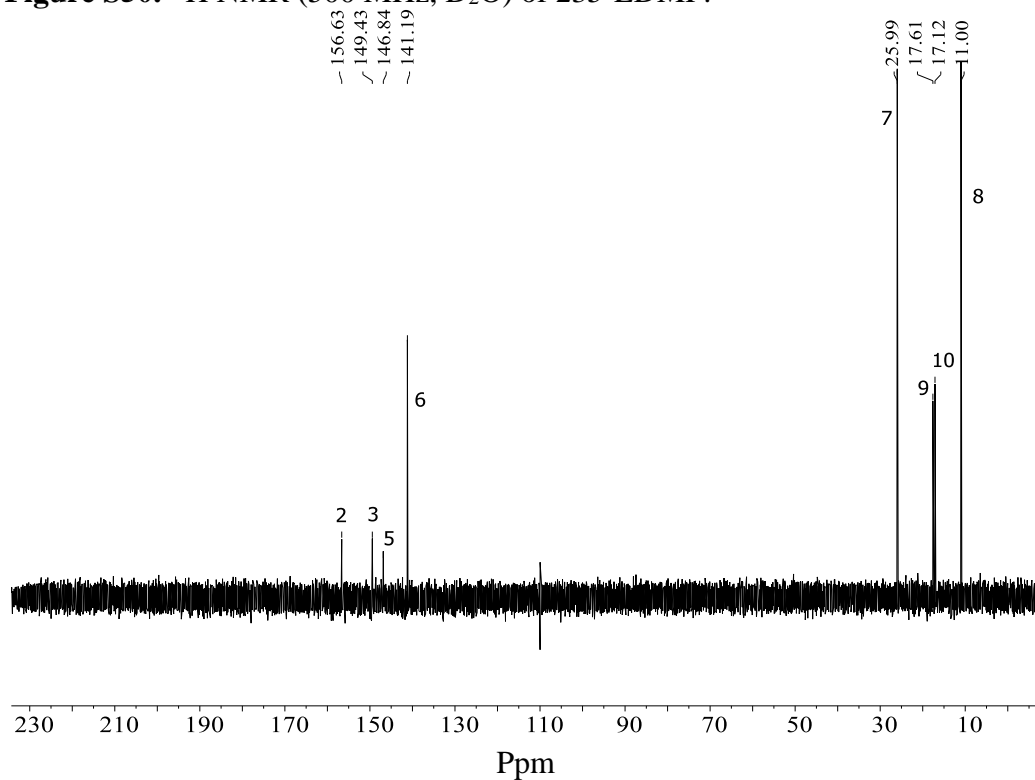


Figure S51. ^{13}C NMR (126 MHz, D_2O) of 235-EDMP.

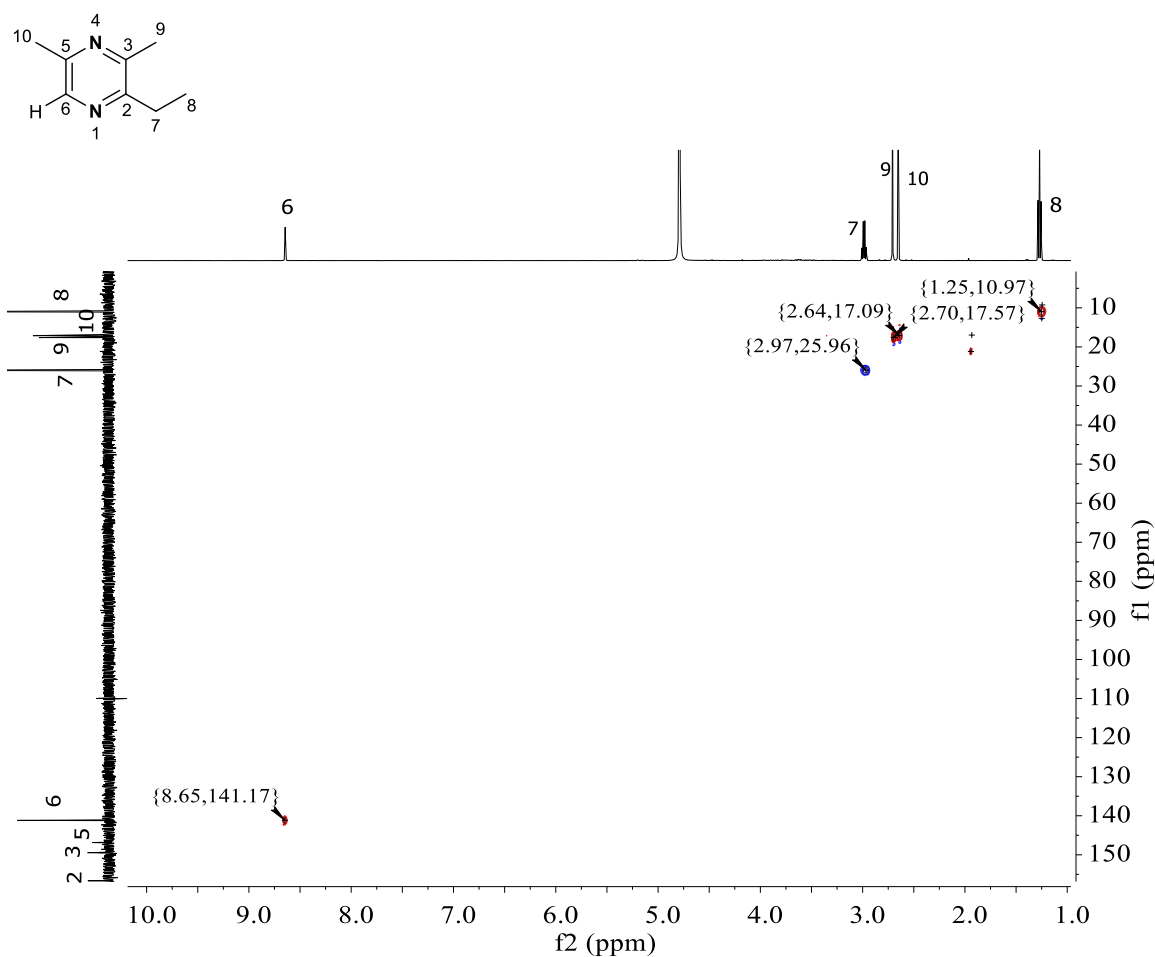


Figure S52. $^1J_{C,H}$ (^{13}C - 1H HSQC, D_2O) spectrum of 235-EDMP. Correlation data is summarized in Table S7.

Table S7. $^1J_{C,H}$ (^{13}C - 1H HSQC) correlation data for 235-EDMP.

C	DEPT	δ_C	H	δ_H (multiplicity)
6	CH	141.1	6	8.65 (<i>s</i>)
7	CH ₂	25.9	7	2.97 (<i>q</i>)
8	CH ₃	10.9	8	1.25 (<i>t</i>)
9	CH	17.6	9	2.70 (<i>s</i>)
10	CH	17.1	10	2.64 (<i>s</i>)

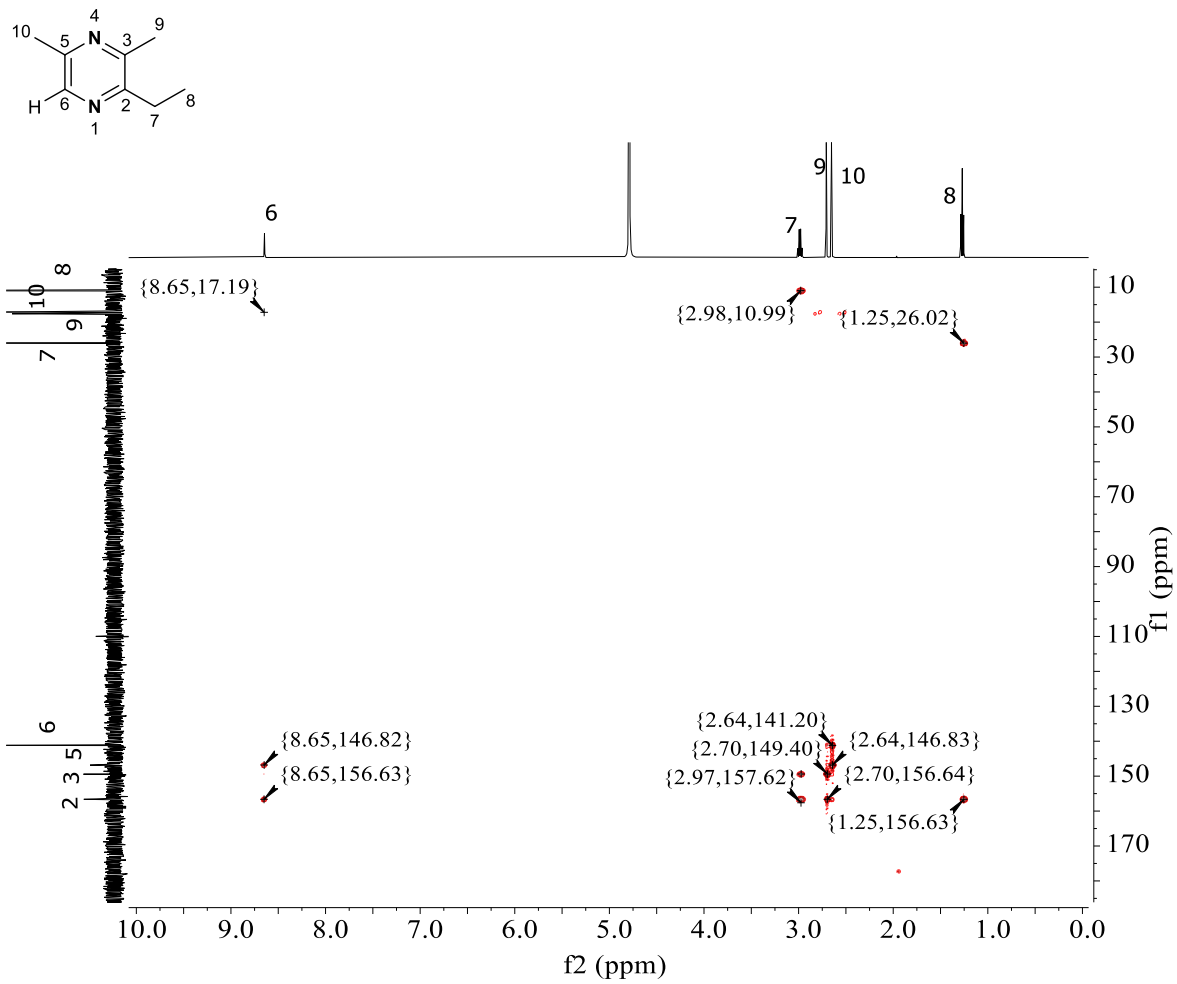
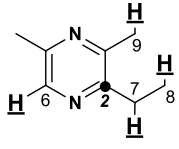
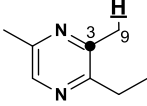
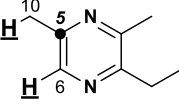
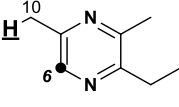
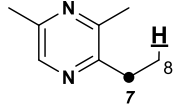
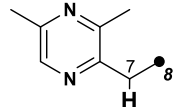
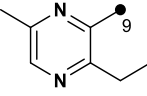
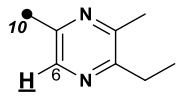


Figure S53. $^2J_{\text{C,H}}$, $^3J_{\text{C,H}}$ (^{13}C - ^1H HMBC) spectrum of 235-EDMP. Correlation data are summarized in Table S8.

Table S8. ${}^2J_{C,H}$, ${}^3J_{C,H}$ (${}^{13}C$ - 1H HMBC) correlation data for 235-EDMP

C	δ_C	H	δ_H (multiplicity)	HMBC (${}^nJ_{C,H}$ correlations) ^a
2	156.6	6	8.65 (s, ${}^3J_{C,H}$)	
		7	2.97 (q, ${}^2J_{C,H}$)	
		8	1.25 (t, ${}^3J_{C,H}$)	
		9	2.70 (s, ${}^3J_{C,H}$)	
3	149.4	9	2.70 (s, ${}^4J_{C,H}$)	
5	146.8	10	2.64 (s, ${}^4J_{C,H}$)	
		6	8.65 (s, ${}^4J_{C,H}$)	
6	141.2	10	2.64 (s, ${}^3J_{C,H}$)	
7	25.9	8	1.25 (t, ${}^2J_{C,H}$)	
8	10.9	7	2.97 (q, ${}^2J_{C,H}$)	
9	17.6	--	--	
10	17.1	6	8.65 (s, ${}^3J_{C,H}$)	

^aHMBC correlations between carbon (●) and hydrogen (shown explicitly as **bold** and underlined) are shown in the structures.

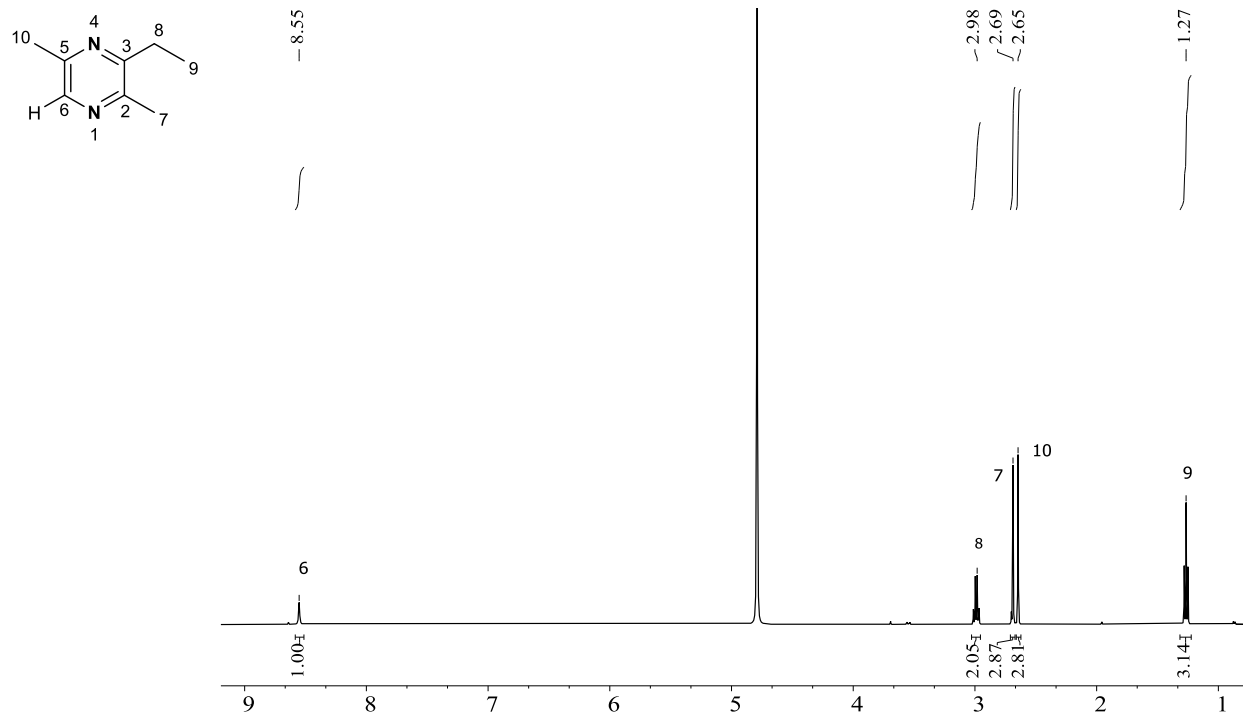


Figure S54. ^1H NMR (500 MHz, D_2O) of 325-EDMP.

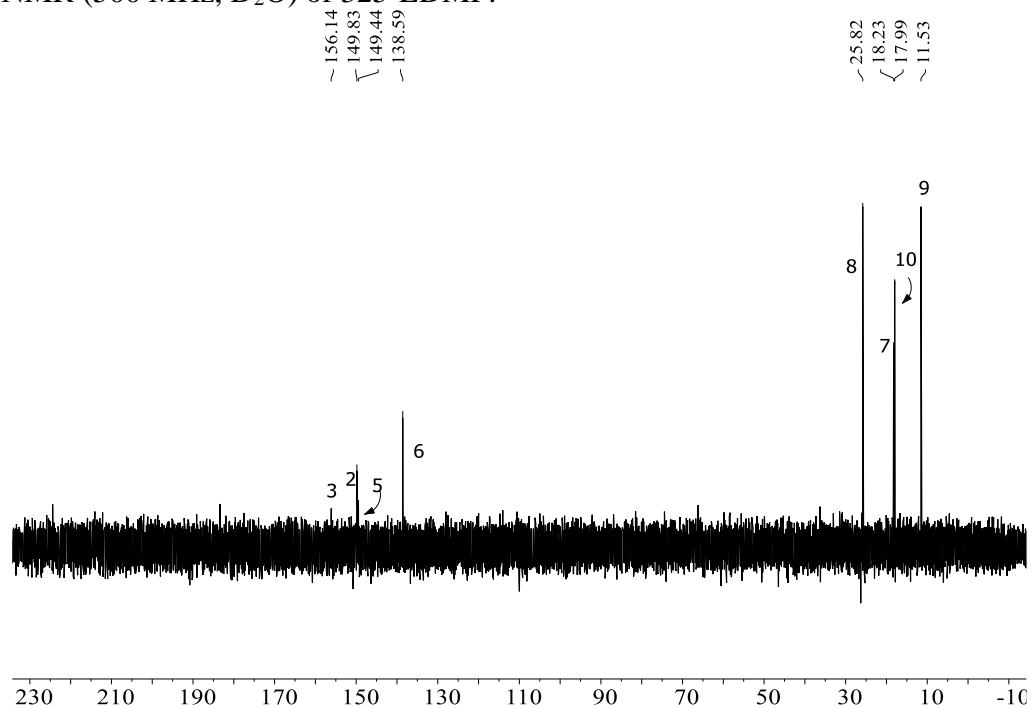


Figure S55. ^{13}C NMR (126 MHz, D_2O) of 325-EDMP

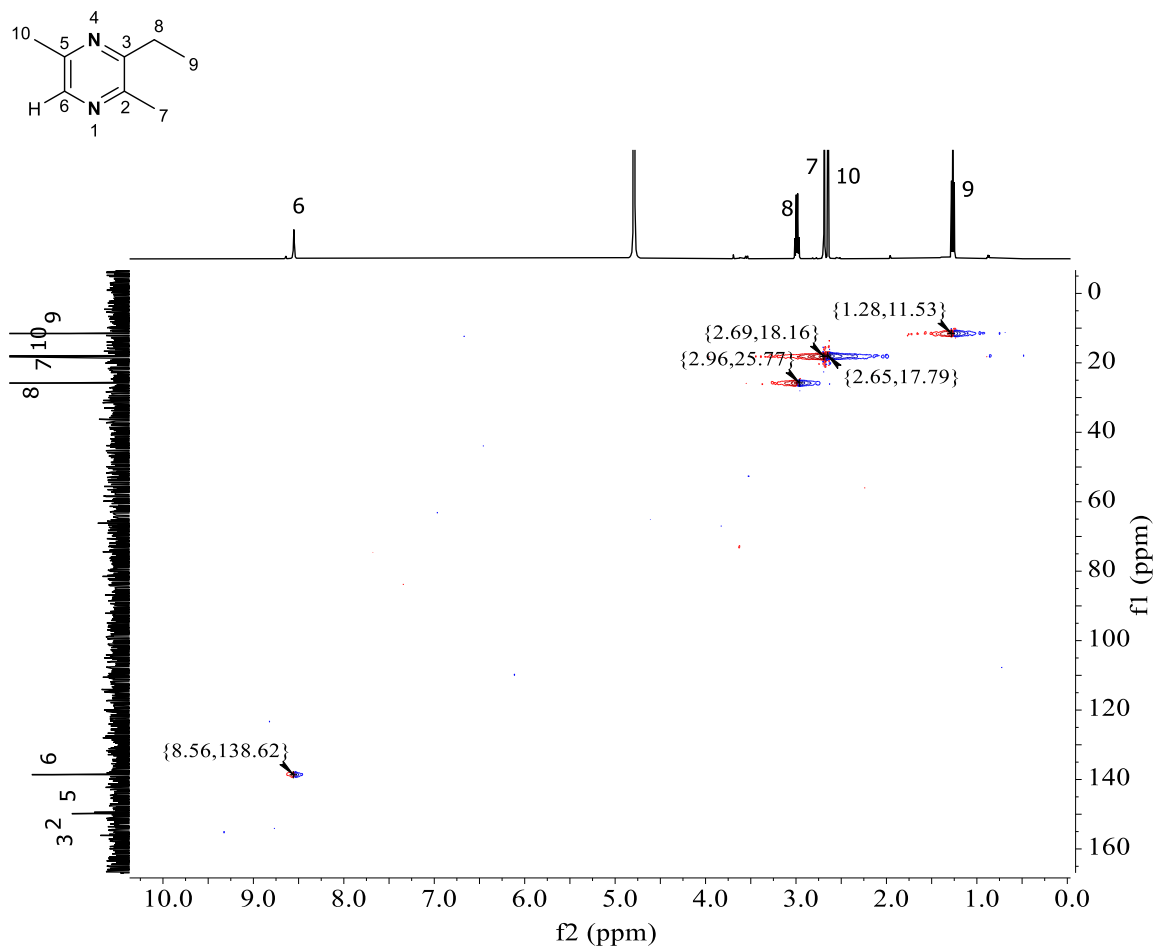


Figure S56. $^1J_{\text{C,H}}$ (^{13}C - ^1H HSQC, D_2O) correlation spectrum of 325-EDMP. Correlation data are summarized in Table S9.

Table S9. $^1J_{\text{C,H}}$ (^{13}C - ^1H HSQC) correlations in HSQC of 325-EDMP

C	DEPT	δ_{C}	H	δ_{H} (multiplicity)
6	CH	138.6	6	8.56 (<i>s</i>)
7	CH ₃	11.5	8	1.28 (<i>t</i>)
8	CH ₃	18.1	9	2.69 (<i>s</i>)
9	CH ₂	25.7	7	2.96 (<i>q</i>)
10	CH ₃	17.7	10	2.65 (<i>s</i>)

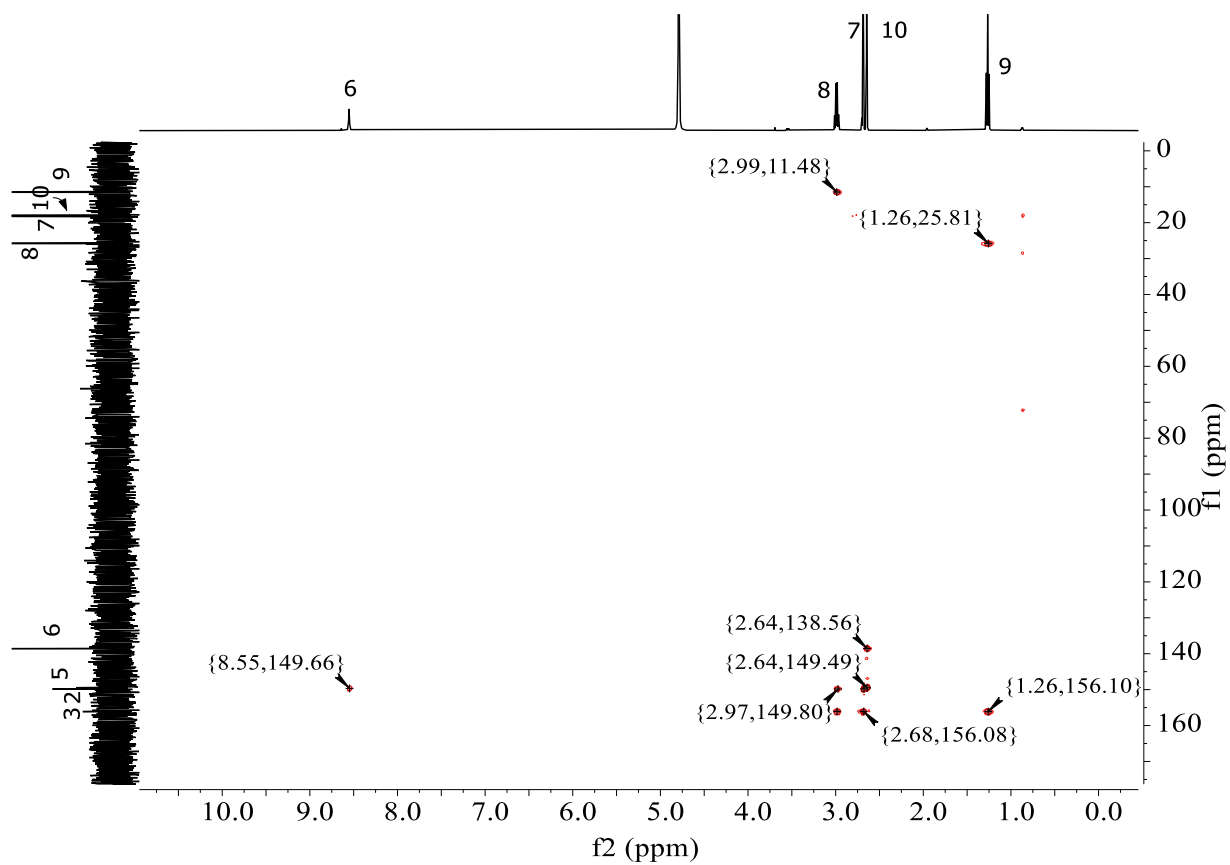
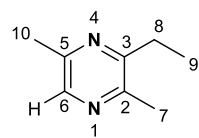
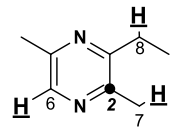
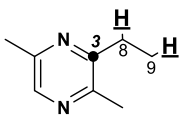
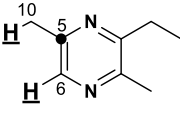
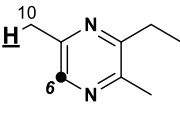
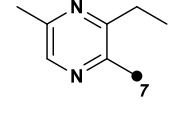
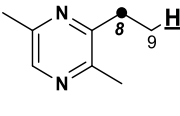
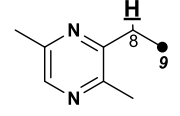
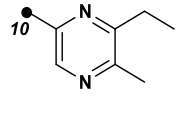


Figure S57. $^2J_{C,H}$, $^3J_{C,H}$ (^{13}C - 1H HMBC) correlation spectrum of 325-EDMP. Correlation data are summarized in Table S10.

Table S10. ${}^2J_{C,H}$, ${}^3J_{C,H}$ (${}^{13}C$ - 1H HMBC) Coupling Data for 325-EDMP

C	δ_C	H	δ_H (multiplicity)	HMBC (${}^nJ_{C,H}$ correlations) ^a
2	149.8	6	8.56 (s, ${}^3J_{C,H}$)	
		7	2.69 (s, ${}^2J_{C,H}$)	
		8	2.97 (s, ${}^3J_{C,H}$)	
3	156.1	8	2.97 (q, ${}^3J_{C,H}$)	
		9	1.26 (t, ${}^3J_{C,H}$)	
5	149.4	6	8.56 (s, ${}^2J_{C,H}$)	
		10	2.64 (s, ${}^2J_{C,H}$)	
6	138.6	10	2.64 (s, ${}^3J_{C,H}$)	
7	18.1	--	--	
8	25.7	9	1.26 (t, ${}^2J_{C,H}$)	
9	11.5	8	2.97 (q, ${}^2J_{C,H}$)	
10	17.7	--	--	

^aHMBC correlations between carbon (●) and hydrogen (shown explicitly as **bold** and underlined) are shown in the structures.

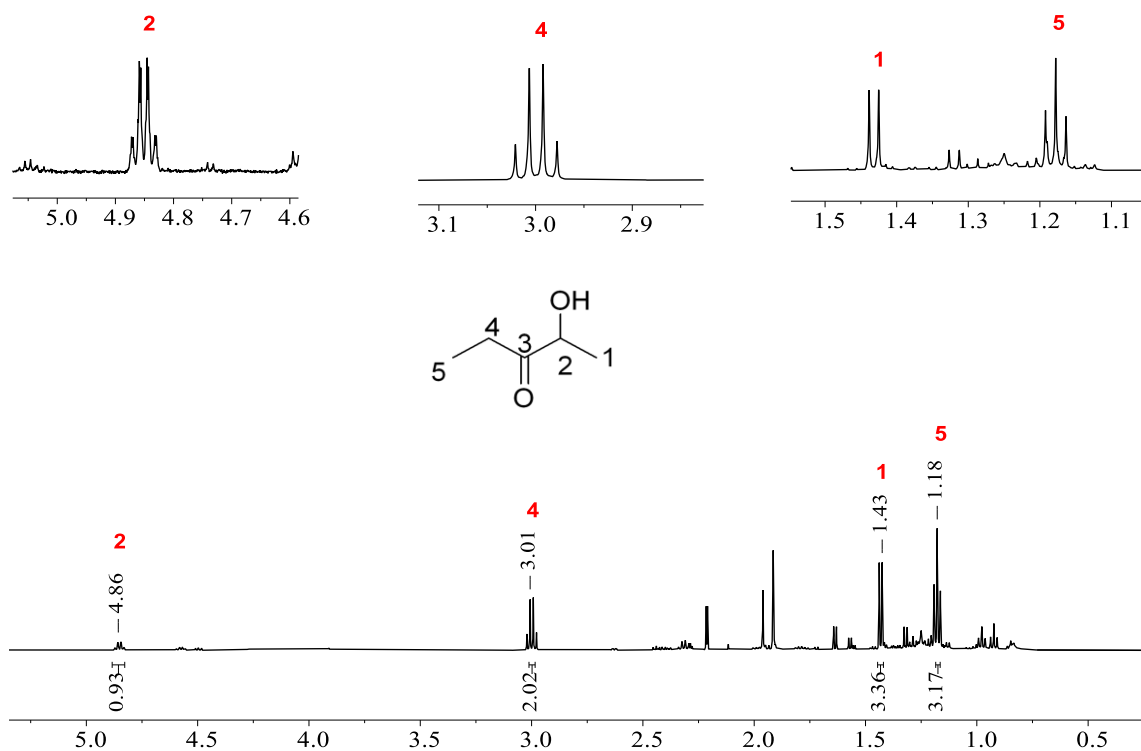


Figure S58. ^1H NMR analysis (^1H NMR, 500 MHz, CDCl_3) of 2-hydroxy-3-pentanone in a crude sample extracted (Et_2O) from a reaction mixture incubated with PDC, acetaldehyde, and 2-oxobutanoate sodium salt for 48 h. δ : 4.86 (1H, quartet, $J = 6.9$ Hz), 3.01 (2H, quartet, $J = 7.1$ Hz), 1.43 (3H, doublet, $J = 7.0$ Hz), 1.18 (3H, triplet, $J = 6.5$ Hz).

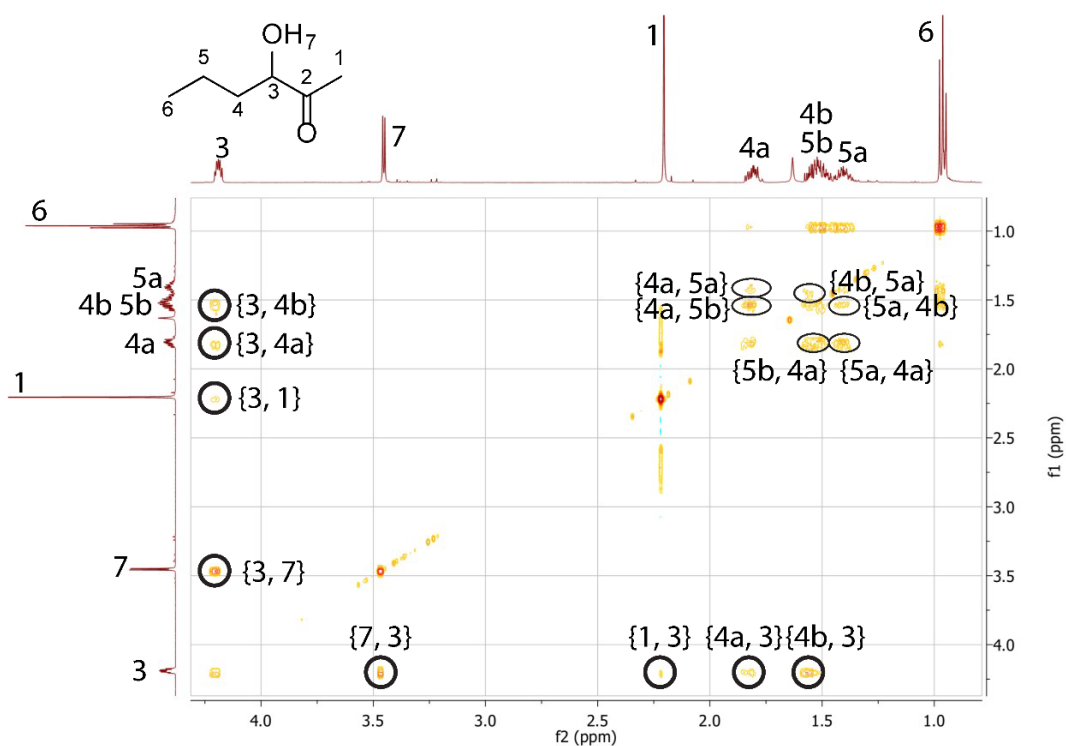


Figure S59. Reference homonuclear⁴⁶ ^1H - ^1H COSY data for 3-hydroxy-2-hexanone 1 used to predict the chemical shift correlations of 3-hydroxy-2-pentanone made via a carboligation reaction catalyzed by a pyruvate decarboxylase in the current study. Homonuclear correlations between H3 and H1, H4, H5, and H7 (bold circles) and annotated highlighted because these were the most diagnostic for identifying ^1H - ^1H correlations in 3-hydroxy-2-pentanone (Figure S60). Other correlations are circled and annotated.

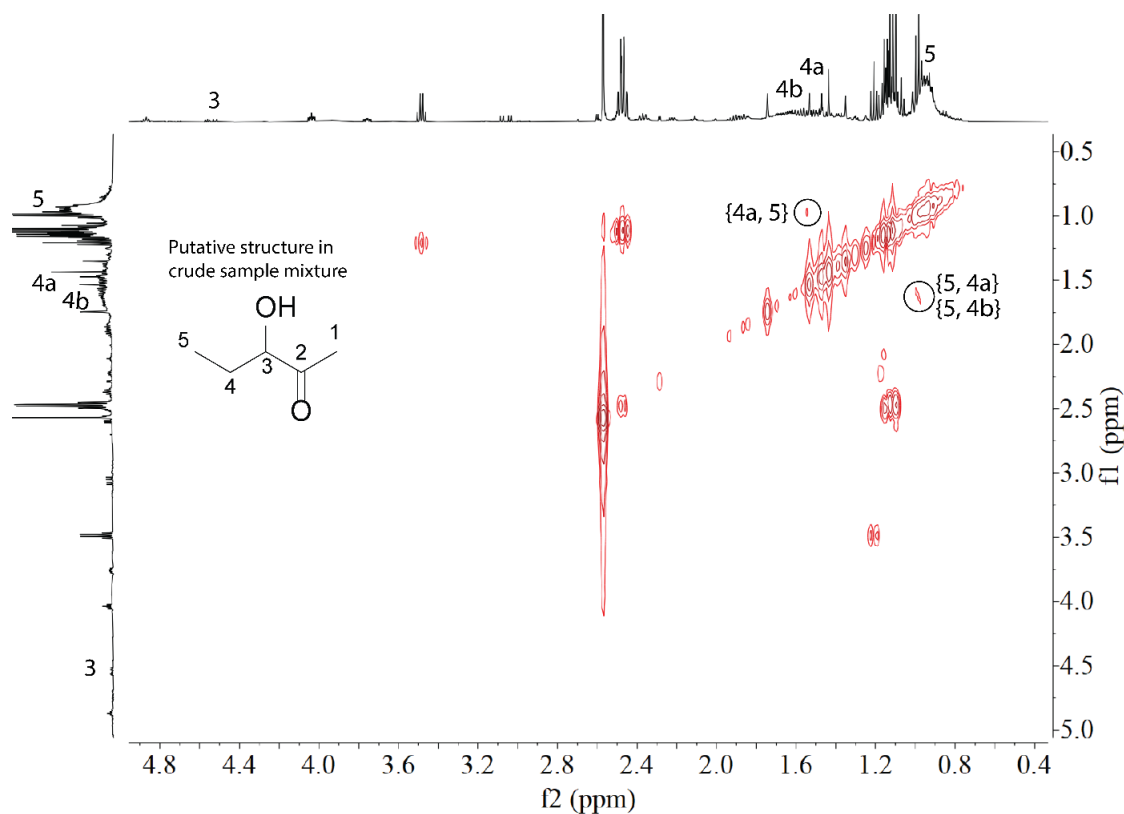


Figure S60. ^1H - ^1H COSY analysis (500 MHz, CDCl_3) of the putative biocatalyzed 3-hydroxy-2-pentanone in a crude sample extracted (Et_2O) from a reaction mixture in which PDC, propanal, and 2-oxopropanoate sodium salt were incubated for 48 h. Putative correlations between H5 and H4 are circled and annotated off-diagonal.

We referenced the COSY spectrum⁴⁶ for 3-hydroxy-2-hexanone (Figure S59) to help predict the chemical shifts for the biocatalyzed 3-hydroxy-2-pentanone (**18**) (Figure S60). H5 (CH_3) of **18** was expected to resonate at ~ 0.9 ppm, similar to H6 (CH_3) of the hexanone homolog. H5 and H4 of to evaluate the potential correlations between H5 and H4 of. Putative correlation between H5 and H4 of **18** was provisionally assigned as a terminal ethyl group; the same correlation between H5 and H4 was also observed in the COSY spectrum for 3-hydroxy-2-hexanone (Figure S60). However, the H3 correlations in the COSY spectrum for the homolog of **18** were seen between all other protons in the molecule (Figure S60). There were no correlations between the

putatively assigned H3 and other protons in the COSY spectrum for **18**, suggesting an apparent structural disconnect and that **18** was likely below the limits of detection.

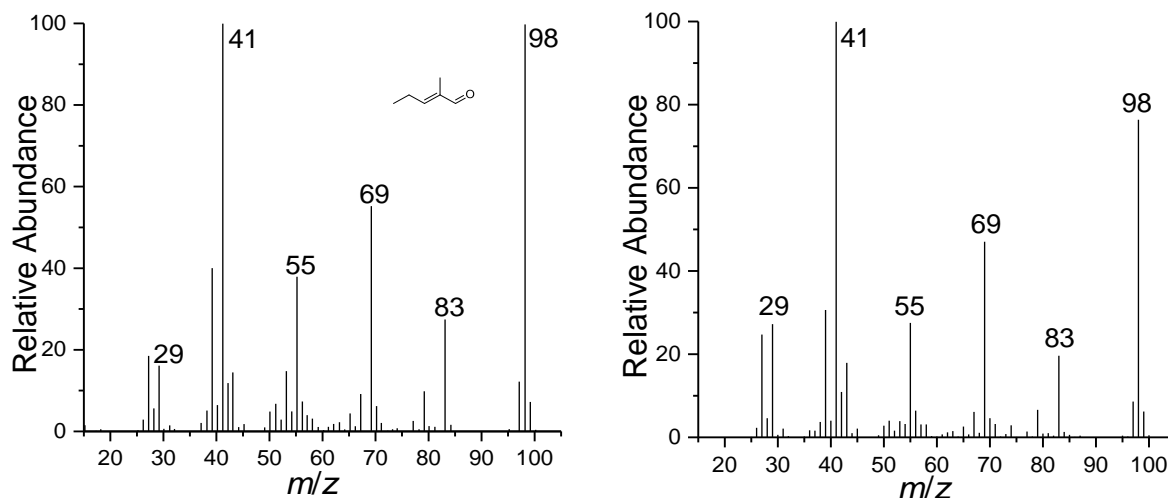


Figure S61. *Left panel:* GC/EI MS of the compound eluting at 5.74 min in the TIC of the crude 3-hydroxy-2-pentanone sample (Figure 4.5 of the main text) whose fragment ions correspond approximately with those for *Right panel:* 2-methyl-2-pentenal in the mass spectral database.⁴⁸

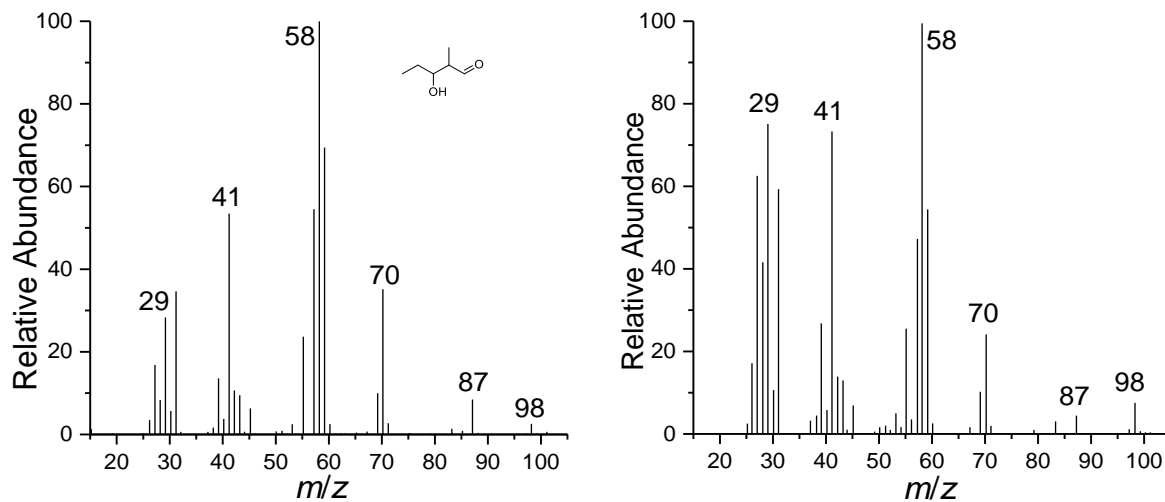


Figure S62. *Left panel:* GC/EI MS of the compound eluting at 7.93 min in the TIC of the crude 3-hydroxy-2-pentanone sample (Figure 4.5 of the main text) whose fragment ions correspond approximately with those for *Right panel:* 3-hydroxy-2-methylpentanal in the mass spectral database.⁴⁸

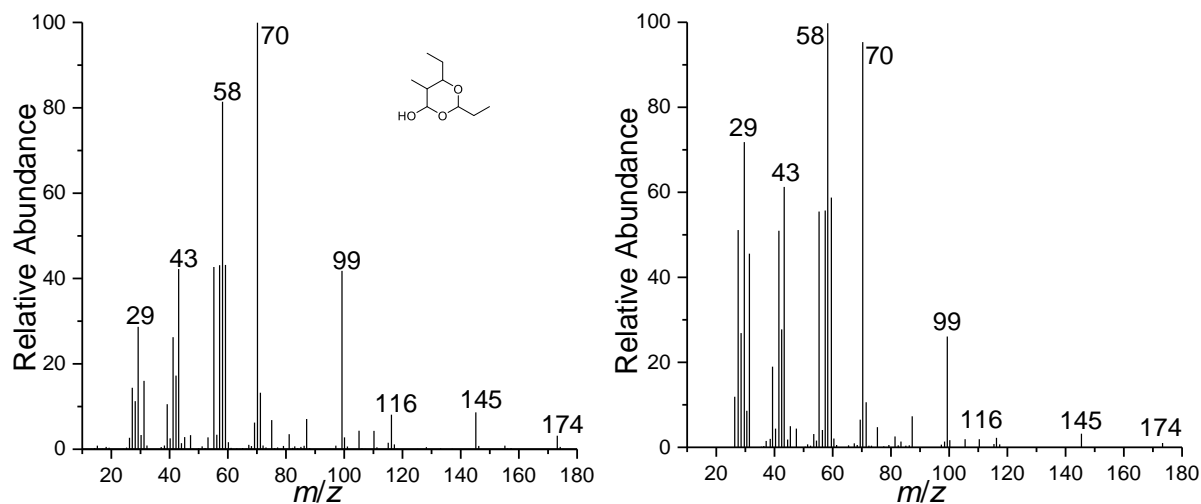


Figure S63. *Left panel:* GC/EI MS of the compound eluting at 12.15 min in the TIC of the crude 3-hydroxy-2-pentanone sample (Figure 4.5 of the main text) whose fragment ions correspond approximately with those for *Right panel:* 2,6-diethyl-5-methyl-1,3-dioxane in the mass spectral database.⁴⁹

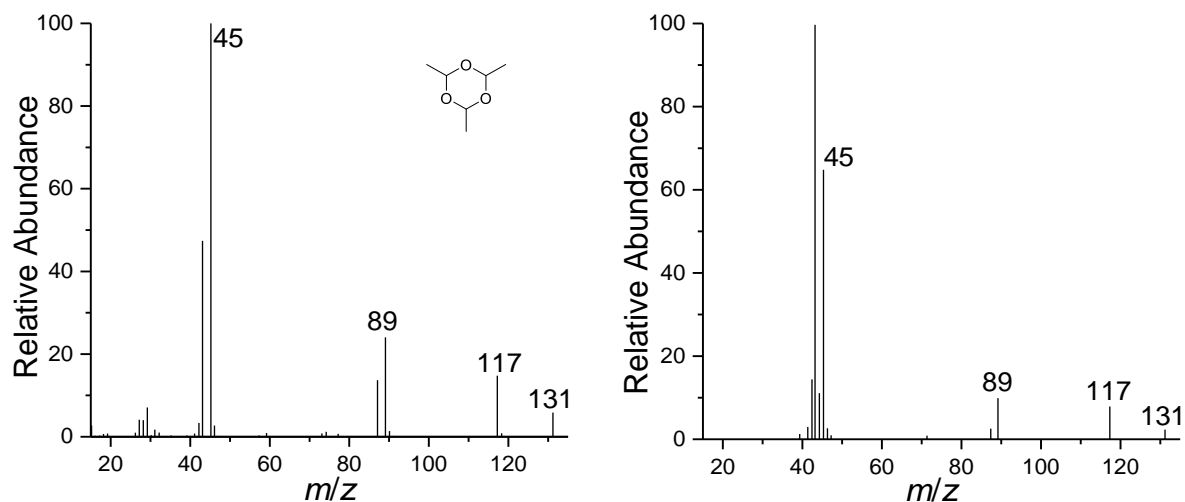


Figure S64. *Left panel:* GC/EI MS of the compound eluting at 4.85 min in the TIC of the 2-hydroxy-3-pentanone sample (Figure 4.6 of the main text) whose fragment ions correspond approximately with those for *Right panel:* paraldehyde in the mass spectral database.⁵⁰

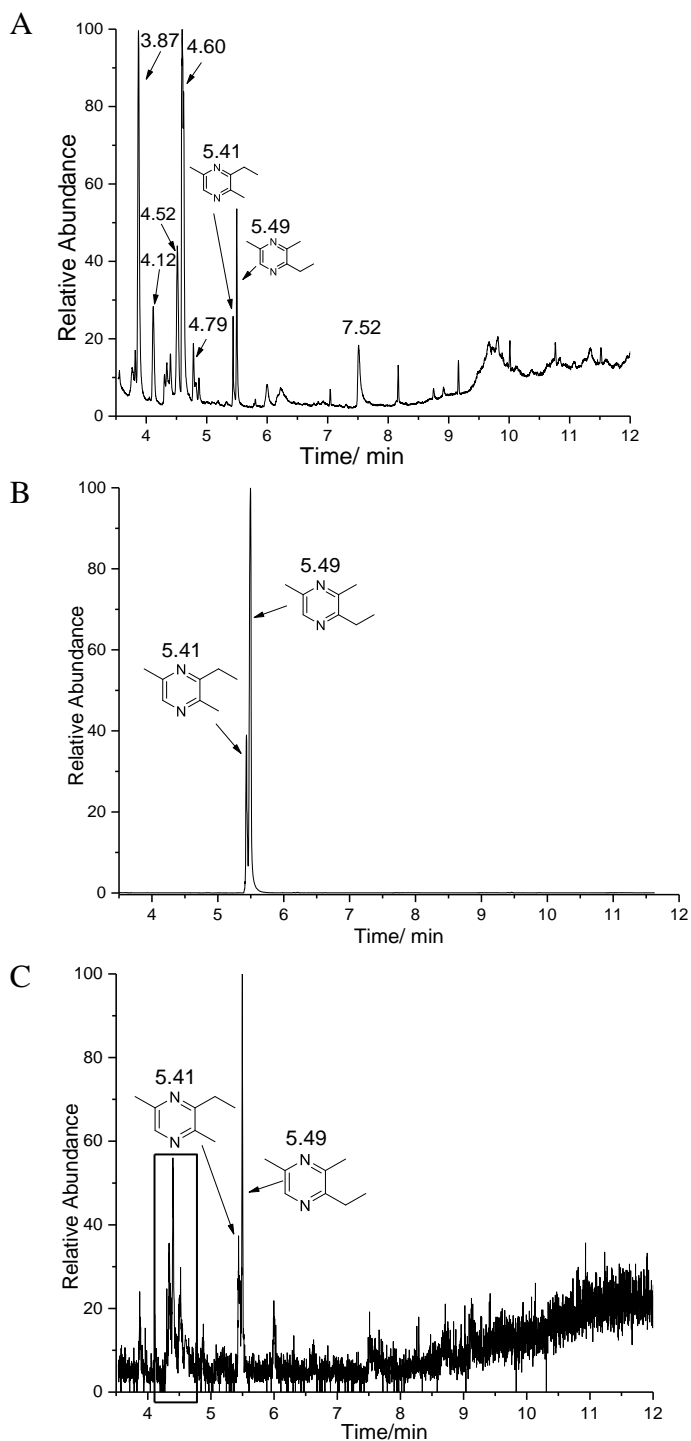


Figure S65. GC/EI-MS analysis in A) total-ion count (TIC) mode, B) selected-ion monitoring (SIM) mode for the EDMPs (m/z 136), and C) SIM mode (m/z 80) for the pyrazine core minus the alkyl substituents of the product mixture after incubating 1,2-diaminopropane and 2-hydroxy-3-pentanone. The products (boxed) are characterized in **Figure 4.8** of the main text.

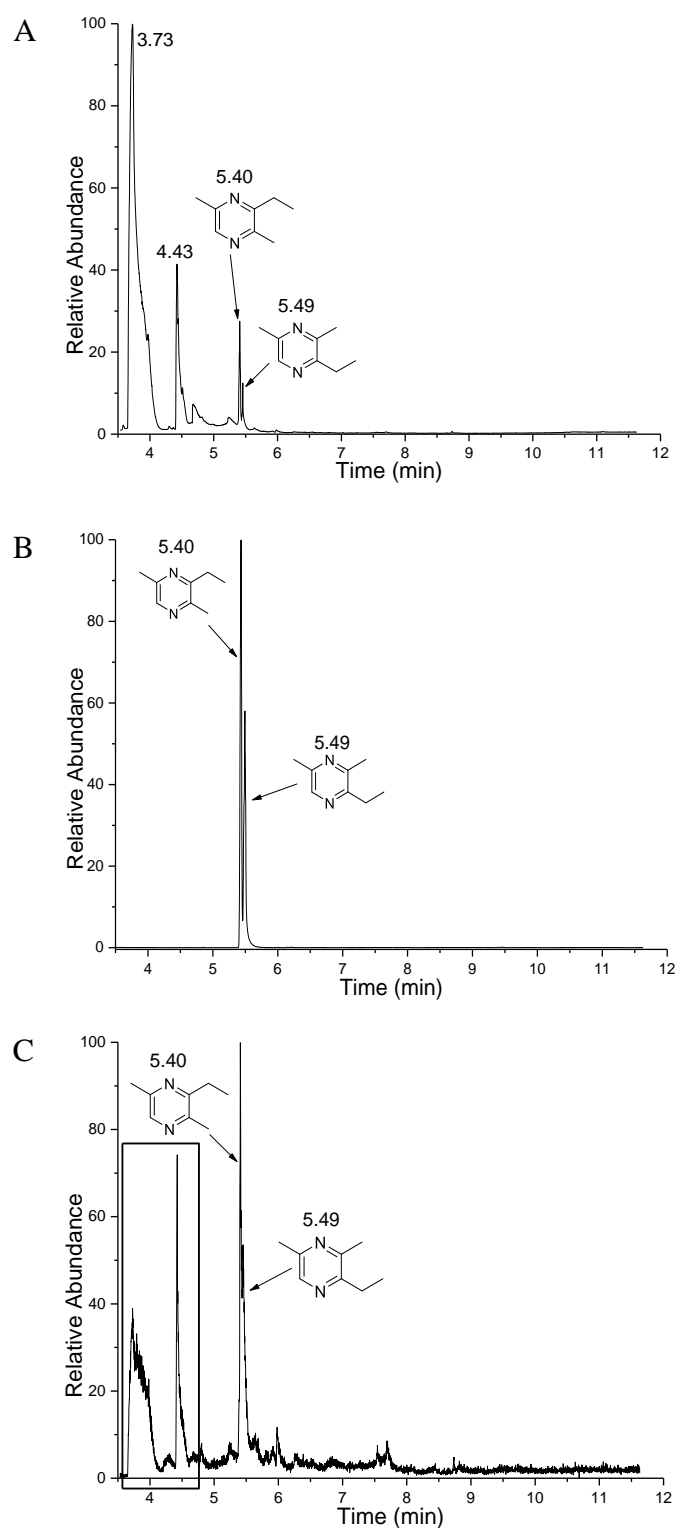


Figure S66. GC/EI-MS analysis in A) TIC mode, (B) SIM mode for the EDMs (m/z 136), and (C) SIM mode (m/z 80) for the pyrazine core minus the alkyl substituents of the product mixture after incubating 1,2-diaminopropane and 3-hydroxy-2-pentanone. The products (boxed) are characterized in Figure 4.8 of the main text.

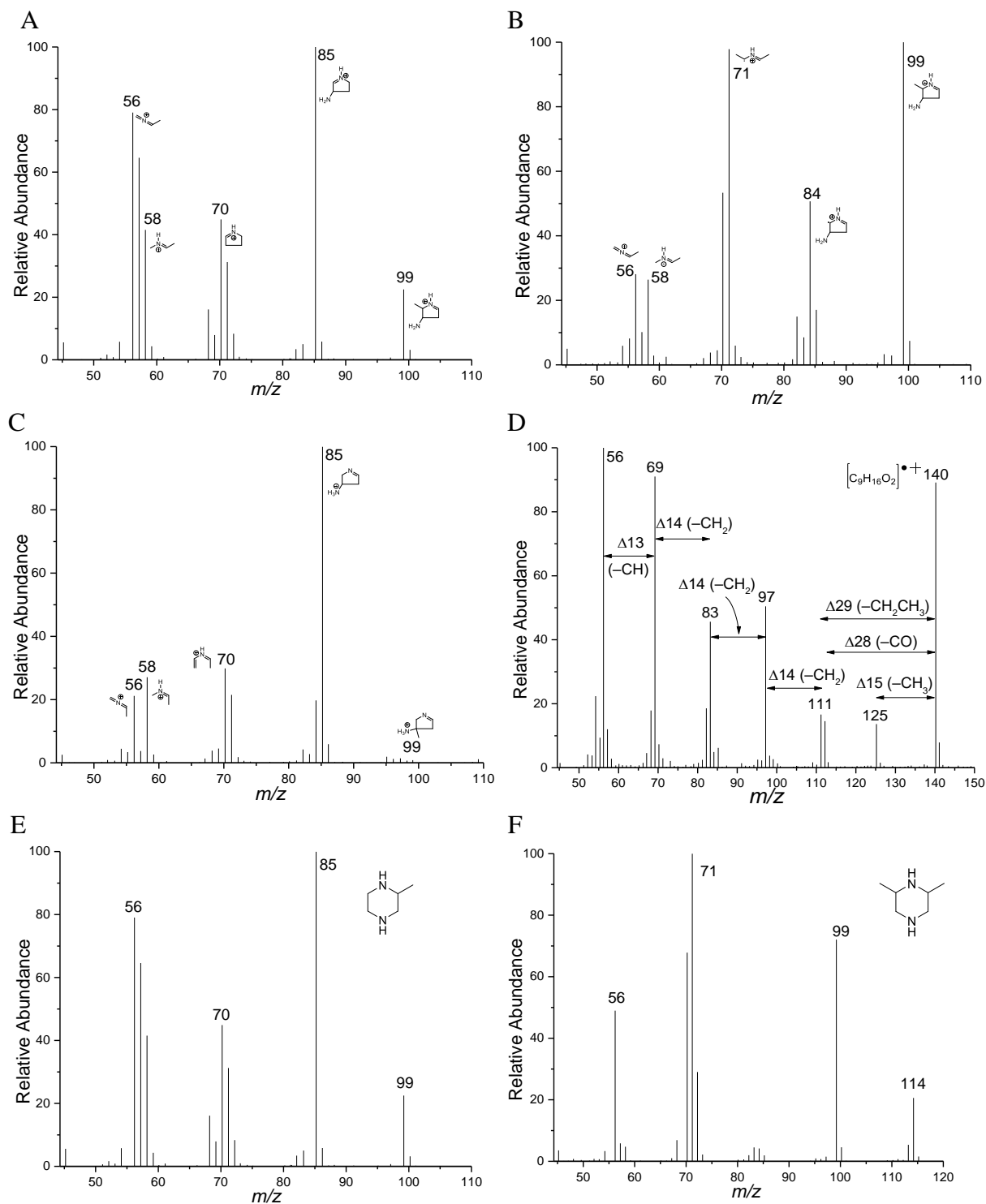


Figure S67. EI-MS fragmentation profile of peaks eluting from the GC (TIC profile in Figure 4.8A of the main text) at A) 3.87 min, B) 4.12 min, C) 4.52 min, deduced from related azo-compounds,⁵² and D) 7.52 min, which corresponded to a putative alkyl ester with a molecular formula of C₉H₁₆O₂. EI-MS fragmentation profile of peaks eluting from the GC (TIC profile in Figure 4.8B of the main text) at E) 3.73 min and F) 4.43 min. The fragment ions in Panels A – C, E, F are inferred from those in Figure 4.8 of the main text and a previous document.⁵²

REFERENCES

REFERENCES

1. Wagner, R., Czerny, M., Bielohradsky, J., and Grosch, W. (1999) Structure-Odour-Activity Relationships of Alkylpyrazines, *Zeitschrift für Lebensmittel-Untersuchung und -Forschung A* 208, 308-316.
2. Silva, M., Metidji, M. O., Stray, H., and Bjørnstad, T. (2019) Alkylpyrazines-from the “Dinner Table” to the Oilfield: A New Class of Partitioning Tracers, In *IOR 2019–20th European Symposium on Improved Oil Recovery*, pp 1-12, European Association of Geoscientists & Engineers.
3. Maga, J. A., and Katz, I. (1982) Pyrazines in Foods: An Update, *Crit. Rev. Food Sci. Nutr.* 16, 1-48.
4. Zhao, C., Cao, H., and Xiao, J. (2020) Pyrazines in Food In *Handbook of Dietary Phytochemicals* (Xiao, J., Sarker, S. D., and Asakawa, Y., Eds.), pp 1-25, Springer Singapore, Singapore.
5. Maga, J. A. (1992) Pyrazine Update, *Food Rev. Int.* 8, 479-558.
6. Brophy, J., Cavill, G., and Plant, W. (1981) Volatile Constituents of an Australian Ponerine Ant *Rhytidoponera metallica*, *Insect Biochem.* 11, 307-310.
7. Moore, B. P., Brown, W. V., and Rothschild, M. (1990) Methylalkylpyrazines in Aposematic Insects, Their Hostplants and Mimics, *Chemoecology* 1, 43-51.
8. Kosuge, T., Zenda, H., Tsuji, K., Yamamoto, T., and Narita, H. (1971) Studies on Flavor Components of Foodstuffs: Part I, Distribution of Tetramethylpyrazine in Fermented Foodstuffs, *Agric. Biol. Chem.* 35, 693-696.
9. Koehler, P., Mason, M., and Odell, G. (1971) Odor Threshold Levels of Pyrazine Compounds and Assessment of Their Role in The Flavor of Roasted Foods, *J. Food Sci.* 36, 816-818.
10. Rapp, A., and Mandery, H. (1986) Wine aroma, *Experientia* 42, 873-884.
11. Zhao, X., Ju, Y., Wei, X., Dong, S., Sun, X., and Fang, Y. (2019) Significance and Transformation of 3-Alkyl-2-Methoxypyrazines Through Grapes to Wine: Olfactory Properties, Metabolism, Biochemical Regulation, and the HP–MP Cycle, *Molecules* 24, 4598.

12. Lund, S. T., and Bohlmann, J. (2006) The Molecular Basis for Wine Grape Quality-a Volatile Subject, *Science* 311, 804-805.
13. Synos, K., Reynolds, A., and Bowen, A. (2015) Effect of Yeast Strain on Aroma Compounds in Cabernet Franc Icewines, *LWT-Food Science and Technology* 64, 227-235.
14. Zviely, M., Shqara, E. A., and Hodrien-Frutarom, D. (2003) Chocarom Pyrazine, *Perfum. Flavor.* 28, 30-38.
15. Rizzi, G. P. (1988) The Biogenesis of Food-Related Pyrazines, *Food Rev. Int.* 4, 375-400.
16. Izzo, H. V., and Ho, C. T. (1992) Ammonia Affects Maillard Chemistry of an Extruded Autolyzed Yeast Extract: Pyrazine Aroma Generation and Brown Color Formation, *J. Food Sci.* 57, 657-659.
17. Amrani-Hemaimi, M., Cerny, C., and Fay, L. B. (1995) Mechanisms of Formation of Alkylpyrazines in the Maillard Reaction, *J. Agric. Food. Chem.* 43, 2818-2822.
18. Maga, J. A., and Sizer, C. E. (1973) Pyrazines in Foods, *CRC Critical Reviews in Food Technology* 4, 39-115.
19. Snape, H. L., and Brooke, A. (1897) LII.—Laurent's amarone, *Journal of the Chemical Society, Transactions* 71.
20. Eicher, T., Hauptmann, S., and Speicher, A. (2013) *The Chemistry of Heterocycles: Structure, Reactions, Syntheses, and Applications*, 3rd ed., Wiley-Interscience.
21. Latha, B. M., Sadasivam, V., and Sivasankar, B. (2007) A Highly Selective Synthesis of Pyrazine From Ethylenediamine on Copper Oxide/Copper Chromite Catalysts, *Catal. Commun.* 8, 1070-1073.
22. Cherng, Y.-J. (2002) Efficient Nucleophilic Substitution Reactions of Pyrimidyl and Pyrazyl Halides With Nucleophiles Under Focused Microwave Irradiation, *Tetrahedron* 58, 887-890.
23. Rizzi, G. P. (1968) Reactions of Methylpyrazines with Organolithium Reagents, *J. Org. Chem.* 33, 1333-1337.
24. Büchi, G., and Galindo, J. (1991) Regioselective Synthesis of Alkylpyrazines, *J. Org. Chem.* 56, 2605-2606.
25. Ong, K. T., Liu, Z.-Q., and Tay, M. G. (2017) Review on the Synthesis of Pyrazine and Its Derivatives, *Borneo J. Resour. Sci. Technol.* 7, 60-75.

26. Gilchrist, T. L. (1997) *Heterocyclic Chemistry*, 3rd ed., Pearson.
27. Mortzfeld, F. B., Hashem, C., Vrankova, K., Winkler, M., and Rudroff, F. (2020) Pyrazines: Synthesis and Industrial Application of these Valuable Flavor and Fragrance Compounds, *Biotechnol. J.*
28. Schwab, W., Davidovich-Rikanati, R., and Lewinsohn, E. (2008) Biosynthesis of plant-derived flavor compounds, *Plant J.* 54, 712-732.
29. Zviely, M. (2010) Pyrazines for Fragrances, *Perfum. Flavor.* 35, 32-34.
30. Rychen, G., Aquilina, G., Azimonti, G., Bampidis, V., de Lourdes Bastos, M., Bories, G., Cocconcelli, P. S., Flachowsky, G., Gropp, J., Kolar, B., Kouba, M., López Puente, S., López-Alonso, M., Mantovani, A., Mayo, B., Ramos, F., Saarela, M., Villa, R. E., Wallace, R. J., Wester, P., Brantom, P., Dusemund, B., Hogstrand, C., Van Beelen, P., Westendorf, J., Gregoret, L., Manini, P., and Chesson, A. (2017) Safety and Efficacy of Pyrazine Derivatives Including Saturated Ones Belonging to Chemical Group 24 When Used as Flavourings for All Animal Species, *EFSA Journal* 15, e04671.
31. Mizukami, Y., Sawai, Y., and Yamaguchi, Y. (2008) Changes in the Concentrations of Acrylamide, Selected Odorants, and Catechins Caused by Roasting of Green Tea, *J. Agric. Food. Chem.* 56, 2154-2159.
32. Silva-Junior, E. A., Ruzzini, A. C., Paludo, C. R., Nascimento, F. S., Currie, C. R., Clardy, J., and Pupo, M. T. (2018) Pyrazines from Bacteria and Ants: Convergent Chemistry within an Ecological Niche, *Sci. Rep.* 8, 1-7.
33. Maga, J. A., and Sizer, C. E. (1973) Pyrazines in Foods. Review, *J. Agric. Food. Chem.* 21, 22-30.
34. Alpert, H. R., Agaku, I. T., and Connolly, G. N. (2016) A study of pyrazines in cigarettes and how additives might be used to enhance tobacco addiction, *Tob. Control* 25, 444-450.
35. El-Hage, R., El-Hellani, A., Salman, R., Talih, S., Shihadeh, A., and Saliba, N. A. (2018) Fate of pyrazines in the flavored liquids of e-cigarettes, *Aerosol science and technology : the journal of the American Association for Aerosol Research* 52, 377-384.
36. Ganji, P., and van Leeuwen, P. W. (2017) Phosphine Supported Ruthenium-Nanoparticle Catalyzed-Synthesis of Substituted Pyrazines and Imidazoles From α -Diketones, *J. Org. Chem.* 82, 1768-1774.

37. Ashraf-Khorassani, M., Coleman III, W., Dube, M., and Taylor, L. (2019) Isolation and Purification of Pyrazines Produced by Reaction of Cellulosic-Derived Sugars With NH₄OH and Selected Amino Acids, *J. Chromatogr. Sci.* 57, 784-789.
38. Guan, D., Lu, Y.-Y., Liao, X.-L., Wang, L., and Chen, L. (2014) Electroantennogram and Behavioral Responses of the Imported Fire Ant, *Solenopsis invicta* Buren, to an Alarm Pheromone Component and Its Analogues, *J. Agric. Food. Chem.* 62, 11924-11932.
39. Kurniadi, T., Rhlid, R. B., Fay, L.-B., Juillerat, M.-A., and Berger, R. G. (2003) Chemoenzymatic Synthesis of Aroma Active 5,6-Dihydro- and Tetrahydropyrazines from Aliphatic Acylolins Produced by Baker's Yeast, *J. Agric. Food. Chem.* 51, 3103-3107.
40. Lou, Z., Er, C., Li, J., Wang, H., Zhu, S., and Sun, J. (2012) Removal of Caffeine From Green Tea by Microwave-Enhanced Vacuum Ice Water Extraction, *Anal. Chim. Acta* 716, 49-53.
41. Li, Y.-Y., Lu, Y.-Y., Lu, M., Wei, H.-Y., and Chen, L. (2018) HPLC Separation of 2-Ethyl-5(6)-Methylpyrazine and Its Electroantennogram and Alarm Activities on Fire Ants (*Solenopsis invicta* Buren), *Molecules* 23, 1661.
42. Donato, P., Cacciola, F., Beccaria, M., Dugo, P., and Mondello, L. (2015) Chapter 8 - Lipidomics In *Comprehensive Analytical Chemistry* (Picó, Y., Ed.), Vol. 68, pp 395-439, Elsevier.
43. Kim, S., Thiessen, P., Cheng, T., Yu, B., and Bolton, E. National Center for Biotechnology Information. PubChem Compound Summary for CID 25916, 3-Ethyl-2,5-dimethylpyrazine., January 21, 2021, https://pubchem.ncbi.nlm.nih.gov/compound/3-Ethyl-2_5-dimethylpyrazine
44. Daw, P., Kumar, A., Espinosa-Jalapa, N. A., Diskin-Posner, Y., Ben-David, Y., and Milstein, D. (2018) Synthesis of Pyrazines and Quinoxalines via Acceptorless Dehydrogenative Coupling Routes Catalyzed by Manganese Pincer Complexes, *ACS Catal.* 8, 7734-7741.
45. Dalby, P. A., Ward, J. M., and Hailes, H. C. (2012) 7.17 C–X Bond Formation: C–C Bond Formation using TDP-Dependent Enzymes In *Comprehensive Chirality* (Carreira, E. M., and Yamamoto, H., Eds.), pp 372-389, Elsevier, Amsterdam.
46. Heguaburu, V., do Carmo, H., Parpal, F., Amorós, M. E., and González, A. (2017) Synthesis of aggregation pheromone components of cerambycid species through α -hydroxylation of alkylketones, *Tetrahedron Lett.* 58, 1738-1741.

47. Wallace, W. E. (2021) Mass Spectra In *NIST Chemistry WebBook, NIST Standard Reference Database Number 69* (Linstrom, P. J., and Mallard, W. G., Eds.), National Institute of Standards and Technology, Gaithersburg MD, 20899, <https://doi.org/10.18434/T4D303> (retrieved March 11, 2021).
48. John Wiley & Sons, Inc. SpectraBase; SpectraBase Compound ID=AkNQmSJ3wEu SpectraBase Spectrum ID=5b9DuGfqB3v, <https://spectrabase.com/spectrum/5b9DuGfqB3v> (accessed 3/11/2021).
49. John Wiley & Sons, Inc. SpectraBase; SpectraBase Compound ID=AkNQmSJ3wEu SpectraBase Spectrum ID=14POgL5j8h3, <https://spectrabase.com/spectrum/14POgL5j8h3> (accessed 3/11/2021).
50. John Wiley & Sons, Inc. SpectraBase; SpectraBase Compound ID=6paA77v1rxm SpectraBase Spectrum ID=K477tNjqhcc, <https://spectrabase.com/spectrum/K477tNjqhcc> (accessed 3/11/2021).
51. Quilliam, M. A., Ogilvie, K. K., and Westmore, J. B. (1975) Injector port reactions in gas chromatography: Sources of error in the quantitative analysis of alkylsilyl derivatives of nucleosides, *J. Chromatogr. A* 105, 297-307.
52. Jackson, P., and Attalla, M. I. (2010) N-Nitrosopiperazines form at high pH in post-combustion capture solutions containing piperazine: a low-energy collisional behaviour study, *Rapid Commun. Mass Spectrom.* 24, 3567-3577.
53. John Wiley & Sons, Inc. SpectraBase; SpectraBase Compound ID=454Byit8l3m SpectraBase Spectrum ID=FImLiYpqWqO <https://spectrabase.com/spectrum/FImLiYpqWqO> (accessed 3/25/2021).
54. John Wiley & Sons, Inc. SpectraBase; SpectraBase Compound ID=GWXdgANhpaz <https://spectrabase.com/compound/GWXdgANhpaz#IhNKI04UWEC> (accessed 3/23/2021).
55. Wishart, D. S., Feunang, Y. D., Guo, A. C., Lo, E. J., Marcu, A., Grant, J. R., Sajed, T., Johnson, D., Li, C., Sayeeda, Z., Assempour, N., Iynkkaran, I., Liu, Y., Maciejewski, A., Gale, N., Wilson, A., Chin, L., Cummings, R., Le, D., Pon, A., Knox, C., and Wilson, M. (2018) DrugBank 5.0: a major update to the DrugBank database for 2018, *Nucleic Acids Res.* 46, D1074-d1082.
56. Taber, D. F., DeMatteo, P. W., and Taluskie, K. V. (2007) Synthesis of symmetrical and unsymmetrical pyrazines, *J. Org. Chem.* 72, 1492-1494.